DISSERTATIONS IN
FORESTRY AND
NATURAL SCIENCES

Anni Lehmuskero

Metallic thin film structures and polarization shaping gratings

Publications of the University of Eastern Finland
Dissertations in Forestry and Natural Sciences

UNIVERSITY OF
EASTERN FINLAND

ANNI LEHMUSKERO

Metallic thin film structures and polarization shaping gratings

Publications of the University of Eastern Finland
Dissertations in Forestry and Natural Sciences
No 25

Academic Dissertation
To be presented by permission of the Faculty of Science and Forestry for public examination in the Auditorium M102 in Metria Building at the University of Eastern Finland, Joensuu, on December, 17, 2010,
at 12 o'clock noon.

Department of Physics and Mathematics

Kopijyvä Oy
Joensuu, 2010
Editors: Prof. Pertti Pasanen,
Ph.D. Sinikka Parkkinen, Prof. Kai-Erik Peiponen

Distribution:
University of Eastern Finland Library / Sales of publications
P.O. Box 107, FI-80101 Joensuu, Finland
tel. +358-50-3058396
http://www.uef.fi/kirjasto

ISBN: 978-952-61-0285-6 (printed)
ISSNL: 1798-5668
ISSN: 1798-5668
ISBN: 978-952-61-0286-3 (pdf)
ISSNL: 1798-5668
ISSN: 1798-5676

Author's address:
University of Eastern Finland
Department of Physics and Mathematics
P.O. Box 111
80101 JOENSUU
FINLAND
email: anni.lehmuskero@uef.fi

Supervisors:
Professor Markku Kuittinen, Ph.D.
University of Eastern Finland
Department of Physics and Mathematics
P.O. Box 111
80101 JOENSUU
FINLAND
email: markku.kuittinen@uef.fi

Professor Pasi Vahimaa, Ph.D.
University of Eastern Finland
Department of Physics and Mathematics
P.O. Box 111
80101 JOENSUU
FINLAND
email: pasi.vahimaa@uef.fi

Reviewers:
Professor Stefan Maier, Ph.D.
Imperial College London
Department of Physics
South Kensington Campus
LONDON SW7 2AZ
UNITED KINGDOM
email: s.maier@imperial.ac.uk

Professor Martti Kauranen, Ph.D.
Tampere University of Technology
Department of Physics
P.O. Box 692
33101 TAMPERE
FINLAND
email: martti.kauranen@tut.fi

Opponent:
Professor Joachim Krenn, Ph.D.
Karl Franzens University Graz
Institute of Physics
Nano-Optics Department
Universitätsplatz 5
A-8010 GRAZ
AUSTRIA
email: joachim.krenn@uni-graz.at

ABSTRACT

In this thesis the optical properties of thin metallic films and laser-colored stainless steel surfaces were studied. Highly absorbing polarizing filters and a beamsplitter were also designed and their properties analyzed. Furthermore, a giant optical rotation together with enhanced transmittance for a chiral metallic grating was optimized and the optical phenomena were analyzed.

The research contained experimental and theoretical work. Most of the theoretical calculations were conducted with the Fourier modal method. Most of the optical characterizations were made with an ellipsometer. All the fabricated gratings were produced by electron-beam lithography. Thin films were deposited using evaporation or atomic-layer deposition.

It was determined that the refractive index of metallic thin films changes between different deposition methods and different film thicknesses. The main factors affecting the change were grain size, oxidation, and surface deformations. The colors on the laser-marked surface were caused by thin film interference in different thicknesses of chromium oxide films. It was observed that the oxide thickness increased along with laser energy density if the energy density was below the ablation threshold.

Furthermore, it was suggested that the main reasons for the high absorbance in the filters and in the beamsplitter was light coupling into localized surface plasmons and guided-mode resonance. Weaker absorbance in a wire grid polarizer occurred at the bulk plasma resonance wavelength. Finally, it was revealed that in chiral gratings the main optical effects contributing to enhanced transmittance together with the giant optical rotation were surface plasmon polaritons, the Rayleigh anomaly, and localized surface plasmons.

Universal Decimal Classification: 535.4, 535.5, 681.7.063, 681.7.064
PACS Classification: 73.20.Mf, 78.20.-e, 78.66.Bz, 42.79.Dj, 42.79.Ci
INSPEC Thesaurus: optics; micro-optics; optical properties; refractive index; ellipsometry; modal analysis; optical fabrication; microfabrication;

nanofabrication; electron beam lithography; evaporation; atomic layer deposition; thin films; diffraction gratings; optical filters; optical polarisers; polarisation; optical beam splitters; metals; stainless steel; grain size; oxidation; deformation; surface plasmons; plasmonics; polaritons
Yleinen suomalainen asiasanasto: optiikka; optiset laitteet; metallit; ruostumaton ters; valmistustekniikka; mikrotekniikka; nanotekniikka

Preface

This thesis sums up the work I did during the years as a researcher in the optics group in Joensuu. Most of the research was done in front of the computer by reading e-books and articles and executing numerical simulations. There were also several times when I just stared at the empty wall thinking about physical issues. All this work was done in parallel with the music studies in another school. Therefore, the past few years have been very busy, and although the research and writing process have been rewarding, I am somewhat relieved that this book is finally complete.

My scientific journey includes several people that I would like to acknowledge. Firstly, I would like to express my gratitude to Prof. Timo Jääskelinen for providing me the opportunity to work at the Department of Physics and Mathematics. Prof. Markku Kuittinen and Prof. Pasi Vahimaa have given me interesting scientific subjects to study, which I wish to thank them for. The discussions with them, Prof. Jari Turunen, and Docent Jani Tervo have helped me on my way to become an independent scientist, which I also appreciate. I also would like to acknowledge all the co-authors and the reviewers, Prof. Martti Kauranen and Prof. Stefan Maier for their contribution to this thesis. Furthermore, I am grateful to Emil Aaltonen foundation for the financial support.

The days at the office would have been much more boring without the people of the optics group. Therefore, I would like to acknowledge all the former and present personnel of the Department of Physics and Mathematics. Especially, I will be thinking back to Toni, Minna, Noora, Hanna, Ben, Ville K., Kalle, Kimmo S., and Heikki with warmth. Toni also deserves my special thanks. He has helped me in several ways, emotionally and technically, and the discussions on difficult physical topics have been important also for this thesis. Finally, I would like to express my endless gratitude for my mom and dad for all the love and support. I am glad that

you allowed me to climb onto the slippery roof as a child. The star gazing on those cold winter nights brought up several questions about science and life, which finally also resulted in this book.

”And the sky’s the limit”

Joensuu November 27, 2010

Anni Lehmuskero

LIST OF PUBLICATIONS

This thesis consists of the present review of the author's work in the field of metallic thin film structures and polarization shaping gratings and the following selection of the author's publications:

I A. Lehmuskero, M. Kuittinen, and P. Vahimaa, "Refractive index and extinction coefficient dependence of thin Al and Ir films on deposition technique and thickness," *Opt. Express* **15,** 10744–10752 (2007).

II A. Lehmuskero, V. Kontturi, J. Hiltunen, and M. Kuittinen, "Modeling of laser colored stainless steel surfaces by color pixels," *Appl. Phys. B* **98,** 497–500 (2009).

III A. Lehmuskero, B. Bai, P. Vahimaa, and M. Kuittinen, "Wire-grid polarizers in the volume plasmon region," *Opt. Express* **17,** 5481–5489 (2009).

IV A. Lehmuskero, I. Vartiainen, T. Saastamoinen, T. Alasaarela, and M. Kuittinen, "Absorbing polarization selective resonant gratings," *Opt. Express* (accepted) (2010).

V B. Bai, J. Laukkanen, A. Lehmuskero, and J. Turunen, "Simultaneously enhanced transmission and artificial optical activity in gold film perforated with chiral hole array," *Phys. Rev. B*, **81,** 115424 (2010).

Throughout the overview, these papers will be referred to by Roman numeral.

AUTHOR'S CONTRIBUTION

The author conducted the measurements, writing, and analysis in **Paper I**. The idea for **Paper II** arose in discussions with the co-authors. Most of the optical characterizations and analysis were made by the author. The theoretical modeling and writing of the paper was done by the author. In **Paper III** the calculations and writing, and most of the analysis were performed by the author. The idea of **Paper IV** was suggested by the author. In that paper, the author made most of the theoretical calculations, most of the analysis, and all the ellipsometric measurements. In **Paper V** the author performed the ellipsometric measurements, some of the ellipsometric data analysis and contributed to the writing process.

Contents

1 INTRODUCTION **1**

2 ELECTRON THEORY OF METALS **5**
2.1 Origin of optical properties 5
2.2 Electronic resonances 10
2.2.1 Bulk plasmons 11
2.2.2 Surface plasmons 12
2.2.3 Localized surface plasmons 15
2.3 Oxidation 18
2.4 Summary 18

3 ELECTROMAGNETIC THEORY OF LIGHT **19**
3.1 Light in homogenous medium 19
3.1.1 Maxwell's equations 20
3.1.2 Poynting vector 20
3.1.3 Polarization 21
3.1.4 Constitutive relations 21
3.1.5 Boundary conditions 22
3.1.6 Electromagnetic field at interface 23
3.1.7 Angular spectrum representation 24
3.2 Light in periodic structure 25
3.2.1 Diffraction gratings 25
3.2.2 Fourier modal method 28
3.2.3 Grating anomalies 29
3.2.4 Effective medium theory 30
3.3 Summary 31

4 FABRICATION AND CHARACTERIZATION OF METALLIC NANOSTRUCTURES **33**
4.1 Thin film deposition 33
4.1.1 Atomic layer deposition 33

4.1.2 Thermal evaporation 34
4.2 Electron-beam lithography 35
4.3 Laser marking 36
4.4 Ellipsometry 37
4.5 Summary 39

5 THIN METAL AND METAL OXIDE FILMS 41
5.1 Changes in refractive index in metal films 41
5.2 Colors on laser-marked stainless steel 45
5.3 Summary 50

6 POLARIZATION SHAPING METALLIC GRATINGS 51
6.1 Extraordinary wire grid polarizers 51
6.1.1 Inverse polarizer 52
6.1.2 Highly absorbing polarizer 54
6.2 Highly absorbing beamsplitter 57
6.3 Chiral polarization rotator 59
6.4 Summary 63

7 CONCLUSIONS 65

REFERENCES 68

1 Introduction

Thoughts about the nature of light have changed in the course of history. In 1704 Isaac Newton presented the corpuscular theory of light in his book *Opticks* [1]. He stated that light consisted of small particles that propagated along straight lines. The corpuscular theory, however, could not explain all the properties of light. It became clear through experiments, such as the famous double-slit experiment of Thomas Young [2], that light also had a wave manifestation. In addition, in 1845 Michael Faraday presented the first evidence that light was related to electromagnetism. Nowadays, it is obvious that light is both particle and wave in nature and that the waves are electromagnetic. In 1905 Albert Einstein expressed the relationship between the wave and the photon, as Einstein named the light particle, as $E = \hbar f$, where f is the frequency of the electromagnetic wave, E the energy of the associated light particle, and $\hbar$ Planck's constant.

Due to its electromagnetic nature, as light propagates in a medium it interacts with the electrically charged particles in the atoms and molecules. The magnitude of the material responding to the external electromagnetic field is described by optical constants, such as refractive index, permittivity, and permeability. Despite their name, optical *constants* are not constants but are dependent on the frequency of light. This phenomenon is called dispersion and may be modeled by corpuscular [3] and wave [4] theory that successfully lead to similar mathematical representations for the frequency dependent optical constants.

While the influence of homogenous material on the electromagnetic field is governed by the optical constants, the influence of structures and discontinuities must be calculated using a rather complicated set of electromagnetic equations. This is the case with diffraction. Light diffraction is the disturbance of a light wave leading to a departure from rectilinear propagation. The disturbance

occurs in the material interfaces of a structure and is most distinctive when the feature size of the structure is comparable to the wavelength of light. One of the most important modern examples of diffractive devices are diffraction gratings consisting of periodic nano- or micrometer-sized features. They belong to a larger family of nano- and micro-optical devices that enables the harvesting of light into applications such as waveguides, high resolution microscopy, CD-players, holograms, diffractive lenses, and optical sensors. The list of applications is endless and their technological value is unquestionable.

Recently, especially metallic nano- and microstructures have attracted substantial attention from the researchers due to their unique properties. Metals have, however, been studied for more than a hundred years ago but the development of numerical methods, electromagnetic simulation codes, and computers have speeded up research into metallic micro- and nanostructures. Furthermore, the development of nanofabrication techniques have progressed hand in hand with computational techniques, providing the tools for designing, fabricating and analyzing the optical properties of metallic structures.

One of the fascinating fields of optics is plasmonics. It studies the interaction of the conduction electrons and electromagnetic field at metallic interfaces or in small metallic nanostructures. It relies on the free essence of the conduction electrons that may be induced to oscillate collectively and longitudinally. Plasmonics has led to a wide range of applications such as biosensors [5,6], nanoscale light guiding [7,8], and labeling of molecular objects [9–11]. The list will undoubtedly continue to expand as plasmonics is integrated into new areas.

This thesis focuses on metallic nano- and microstructured gratings and thin films. We study the optical properties of metallic and metal oxide thin films and the polarization shaping gratings employing plasmonic effects. Chapters 2 and 3 provide the theoretical background for the studies in the thesis. Chapter 2 includes a more detailed discussion of the basic fundamental optical and chemical

properties of metals that are quite extensively characterized by electrons that respond to an electromagnetic field or react with a chemical substance. In addition, we further explain the properties of plasmonic resonances and present the dispersion relation and resonance conditions for surface and particle plasma resonances. In Chapter 3 we consider light as an electromagnetic wave, introduce some basic concepts of electromagnetic field, and present the analysis tools for light in a homogenous material and a periodic medium. Chapter 4 describes nano- and microstructure fabrication and characterization techniques most relevant to our studies.

Chapters 5 and 6 contain the main results of the thesis. In Chapter 5 we show how the optical properties of metallic thin films change depending on the fabrication method and thickness. Furthermore, we briefly examine the industrial world by revealing the optical effects behind laser-colored stainless steel. In Chapter 6 we introduce polarization shaping devices with untraditional optical properties relying on plasmonic and grating resonances. In addition, we make a thorough investigation of the phenomena behind giant optical activity and enhanced transmission in chiral metallic gratings.

2 Electron theory of metals

The response of matter to an electromagnetic field is characterized by the behavior of electrons in the applied field. In the case of metals, the electrons are essentially free, which gives rise to unique metallic features, both from the chemical and optical point of view. The behavior of electrons may be approached using classical or quantum–mechanical models, but in general the combination of the two provides the deepest understanding of the optical properties, as will be shown in this chapter.

2.1 ORIGIN OF OPTICAL PROPERTIES

Let us consider a molecule that is illuminated by an electromagnetic wave. The electric charges in the molecule are set into oscillatory motion by the electric field of the incident wave. Accelerated electric charges radiate electromagnetic energy. In the case of a system of molecules, each molecule is affected not only by the incident field but also by the resultant of the secondary fields of all the other molecules. Therefore, inside a medium the secondary waves superpose on each other and on the incident wave. [12, 13] This process is the origin of the optical properties of the medium.

The interaction of the field with electric charges leads a to reduction in the propagation speed of the field because the response to the external field is not immediate. In addition, for an oblique incident angle the propagation direction changes. These properties are observed at a macroscopic level and are described by the real part of the refractive index, n, which is defined by the relationship between the speed of light in a vacuum, c_0, and the speed of light in the medium, c

$$n = c_0/c. \tag{2.1}$$

The wavelength of the electromagnetic field in the medium also experiences a change to $\lambda = \lambda_0/n$, where λ_0 is the wavelength of

the incident field in the vacuum.

In addition to reradiating electromagnetic energy, the excited elementary charges may transform part of the incident electromagnetic energy into other forms, thermal energy, for example. This process is called absorbtion. The amplitude of the electromagnetic field decreases as it propagates through an absorbing medium. The imaginary part, k, of the complex refractive index [12],

$$\hat{n}(\omega) = n(\omega) + \mathrm{i}k(\omega), \tag{2.2}$$

determines the rate at which the wave is attenuated. In Eq. (2.2) i represents the imaginary unit, ω is the angular frequency of the incident field, and n is defined by Eq. (2.1). It is evident from Eq. (2.2) that the refractive index, and therefore the motion of the electrons, is dependent on the frequency of the electromagnetic wave.

An external electric field polarizes material so that the positive atom nucleus and negative electrons move in opposite directions. Susceptibility, χ, is a measure of how easily the material is polarized. Susceptibility is actually part of another optical constant, electric permittivity, defined as

$$\hat{\epsilon}(\omega) = \epsilon_0[1 + \chi(\omega)] + \mathrm{i}\frac{\sigma(\omega)}{\omega}\ , \tag{2.3}$$

where ϵ_0 is the permittivity in a vacuum and σ the electric conductivity of the material. The conductivity is non-zero only for materials with electrons that are not bound to the atom nucleus, so-called free electrons. The magnitude of the oscillatory motion of free electrons in the external field is proportional to the electric conductivity. The imaginary part of the permittivity,

$$\Im\{\hat{\epsilon}(\omega)\} = \Im\{\chi(\omega)\} + \Re\{\sigma(\omega)\} \tag{2.4}$$

represents the absorption of the field in the medium. $\Im\{\cdot\}$ denotes the imaginary part and $\Re\{\cdot\}$ the real part. The imaginary part of the susceptibility is associated with the absorption of electrons that are bound to the nucleus and the real part of the conductivity is associated with absorption by the free electrons.

The relative permittivity is related to the refractive index for a non-magnetic medium by

$$\hat{\epsilon}_{\mathrm{r}}(\omega) = \frac{\hat{\epsilon}(\omega)}{\epsilon_0} = \epsilon'(\omega) + \mathrm{i}\epsilon''(\omega) = \hat{n}^2(\omega) \ , \tag{2.5}$$

where ϵ_0 is the permittivity in the vacuum and $\epsilon'(\omega)$ and $\epsilon''(\omega)$ are both real. The relative permittivity is also called dielectric function.

The real and imaginary parts of the complex optical constants, such as refractive index, susceptibility, and permittivity, are connected by integral relations. For relative permittivity the relations may be written as [14–16]

$$\epsilon'(\omega') \ - 1 = \frac{2}{\pi} P \int_0^\infty \frac{\omega \epsilon''(\omega)}{\omega^2 - \omega'^2} \mathrm{d}\omega \ , \tag{2.6}$$

$$\epsilon''(\omega') = -\frac{2\omega'}{\pi} P \int_0^\infty \frac{[\epsilon'(\omega) - 1]}{\omega^2 - \omega'^2} \mathrm{d}\omega + \frac{\sigma_0}{\epsilon_0 \omega'} \ , \tag{2.7}$$

where P denotes the Cauchy principal value of the integral, σ_0 the dc conductivity, and ω' is an artificial pole on the real axis of a complex angular frequency. The equations (2.6) and (2.7) are called Kramers–Kronig relations. They are a direct consequence of the causality principle and they relate the change in phase of an electromagnetic wave to an absorption process [17].

The quantum–mechanical approach to optical properties is based on discretesizing energy into packets called quanta. The energy level diagram of isolated atoms, illustrated in Fig. 2.1, consists of a series of states with discrete energies. A result of the periodicity of the crystal lattice of a medium is that the energy levels are grouped into bands. Optical transitions between these levels lead to absorption and emission of electromagnetic radiation. For example, the absorption of a photon leads to the transition of an electron from a low energy level to the one above it.

Energy bands are divided into three groups. The band representing the core electrons, the valence band and the conduction band. For insulators and semiconductors the conduction band is empty; for conductors it is partly filled. The size of the gap between the valence and conduction band determines whether the material

is an insulator or a semiconductor. For semiconductors the band gap is less than 3 eV. For conductors the two bands overlap.

In metals the electrons in the conduction band can be excited into adjacent unoccupied states by applying an electric field, which results in an electric current. This availability of vacant electron states in the same energy band provides a mechanism, intraband absorption, for absorption of low-energy photons. Absorption in nonconductors, interband absorption, is only likely for photon energies greater than the band gap. [18]

The classical model treats electrons as if they were attached to the nucleus by a spring, as shown in Fig. 2.2. From the equation of motion for a small mass attached to a large mass by a spring we obtain the dipole moment and, consequently, an expression for the relative permittivity,

$$\hat{\epsilon}_{\mathrm{r}}(\omega) = 1 + \frac{N\mathrm{e}^2}{m\epsilon_0} \frac{1}{\omega_0^2 - \omega - i\gamma\omega} , \tag{2.8}$$

where e is the magnitude of the electric charge, ω_0 the resonance frequency of the spring, N the number of oscillators per unit volume, and γ the damping factor of the springs. Eq. (2.8) is called the Lorentz harmonic oscillator model. The quantum–mechanical analog for the resonance frequency ω_0 is the transition frequency of an electron between two energy levels. The damping factor relates

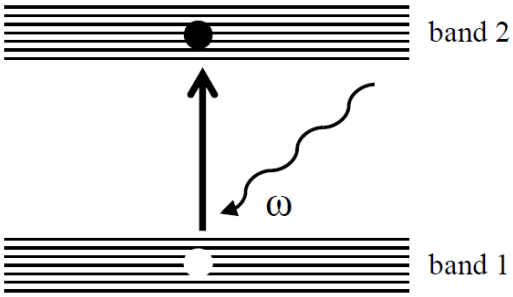

Figure 2.1: Interband absorption of light with angular frequency ω in the energy level diagram. Bands 1 and 2 consist of several energy levels.

in the quantum–mechanical analog to the probability of absorption processes such as transitions to all other atomic states. [19] In general, an optical medium will have many characteristic resonance frequencies. The permittivity may then be described by taking the sum of the Lorentz oscillators with different natural resonance frequencies. [18]

The optical response for free electrons can be obtained from the Lorentz harmonic oscillator model demonstrated in Fig. 2.2 by ignoring the springs, that is, by setting the spring constant in Eq. (2.8) to zero. Then, we obtain the expression for the relative permittivity [20],

$$\hat{\epsilon}_{\mathrm{r}}(\omega) = 1 - \frac{\omega_{\mathrm{p}}^2}{\omega^2 + \mathrm{i}\gamma\omega} \,, \tag{2.9}$$

where

$$\omega_{\mathrm{p}} = \sqrt{\frac{N\mathrm{e}^2}{\epsilon_0 m_0}} \tag{2.10}$$

is the plasma frequency. Now, the constant γ in Eq. (2.9) represents the damping due to the scattering of electrons associated with electrical resistivity [19]. It may be written $\gamma = 1/\tau$, where τ is the mean free time between collisions. The distance between the collisions is called the mean free path. If we ignore the damping, that is

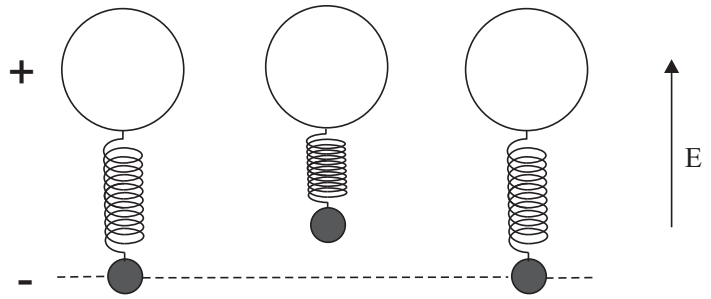

Figure 2.2: Lorentz harmonic oscillator consisting of a heavy positive charge and a light negative mass. Electric field $\mathbf{E}$ *causes displacement from the equilibrium position.*

$\gamma = 0$, the relative permittivity becomes real and may be written

$$\epsilon_{\mathrm{r}}(\omega) = 1 - \frac{\omega_{\mathrm{p}}^2}{\omega^2} \,. \tag{2.11}$$

By substituting Eq. (2.11) into Eq. (2.5) we notice that the refractive index is purely imaginary when $\omega < \omega_{\mathrm{p}}$, real when $\omega > \omega_{\mathrm{p}}$, and zero when $\omega = \omega_{\mathrm{p}}$.

Drude theory alone does not accurately describe the optical characteristics of many metals. Metals usually exhibit some free-electron type of behavior, which can be treated with the Drude theory, but they also have a substantial bound-electron component, due to interband transitions. For example, the colors of gold and copper are a result of interband transitions at the visible spectral range. [12] A more accurate way to describe the permittivity of metals is to combine multiple Lorentz oscillators with the Drude model.

The relative permittivity of aluminum has been calculated with Drude model and the combined Lorentz and Drude model in Fig. 2.3. The calculated values are compared to measured values taken from [21]. At wavelengths below the plasma wavelength, 82 nm, the low-damping approximation given in Eq. (2.11) is valid and the permittivity is real. The real part approaches unity as the wavelength decreases because the electrons are no longer capable of responding to the driving field. As the wavelength increases, the intraband transitions take place, metal becomes conductive, and the imaginary part grows along with the real part according to the Kramers–Kronig relations. However, there is a disturbance in the smoothly behaving permittivity around 800 nm, which is due to interband transitions. This is the reason the Drude model fails in this region.

2.2 ELECTRONIC RESONANCES

One property of metals that arises from the free electrons is that light may excite electronic resonances in them. A common feature

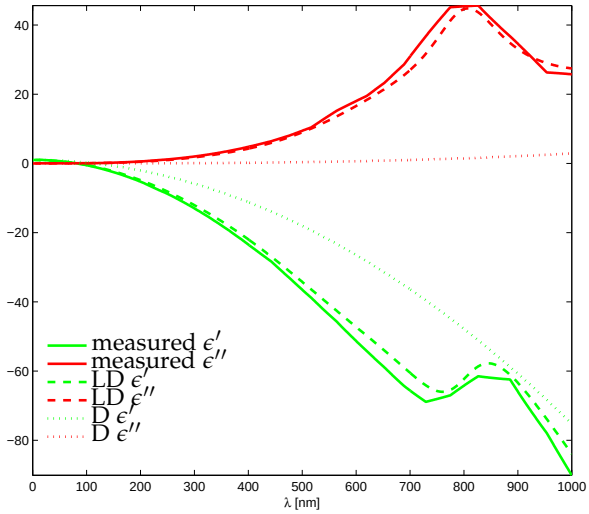

Figure 2.3: Real part ϵ' and imaginary part ϵ'' of relative permittivity for aluminum. LD represents the combined Lorentz–Drude model, D the Drude model. The measured values have been taken from [21].

of electronic resonance is that the oscillation amplitude of the local electric field overcomes the excitation amplitude by orders of magnitude [22]. The resonant oscillation also results in charge density oscillations that are either collective or longitudinal or both, so that the charge density has an oscillatory time dependence $\exp(-i\omega t)$, where t is the time. The charge density oscillation is also referred to as plasma oscillation and its quantum is plasmon [23]. Plasmons may be divided into three groups, which are described in the following sections.

2.2.1 Bulk plasmons

If the damping in Drude's model Eq. (2.9) is assumed to be zero, the relative permittivity vanishes at the plasma frequency. This creates longitudinal electron oscillations called bulk plasma or volume plasma oscillation. Since the relative permittivity is zero, so is re-

fractive index according to Eq. (2.5). The wavelength of the electromagnetic field then approaches infinity inside the medium and the electrons start to move collectively in a phase. This produces a displacement of the whole free electron gas. The fixed ion lattice will exert a restorative force to counteract this displacement of electrons, which causes the electrons to move back to the original direction and consequently again form a restorative force in the opposite direction and so on. The result is that the whole electron gas oscillates at the plasma frequency backwards and forwards with respect to the fixed ions. [18, 19]

True plasma oscillation persists after the external field is removed and can be excited only by a beam of charged particles, such as electrons. [19] Therefore, in optical studies the bulk plasma oscillation refers to the forced oscillations generated by light. There exist some studies where the bulk plasma oscillations have been excited by illuminating a metallic surface at an oblique angle of incidence by light having an electric field component normal to the surface [24].

2.2.2 Surface plasmons

Surface plasmon resonance is a charge density oscillation existing at the interface of the dielectric and metal. The oscillation carries energy along the surface while the field in a direction normal to the surface is evanescent, as illustrated in Fig. 2.4. Because these oscillations may be excited by light, their quantum is called surface plasmon polaritons or surface plasmons.

Let us define the wave number as $k = 2\pi/\lambda$. The wave number is the length of the wave vector which points in the propagating direction of the wave. The propagation constant, that is the wave vector component parallel to the interface, for a surface plasmon polariton is given by [25]

$$k_{\mathrm{SP}}^{\parallel} = k_0 \sqrt{\frac{\hat{\epsilon}_2 \epsilon_1}{\hat{\epsilon}_2 + \epsilon_1}}\,, \tag{2.12}$$

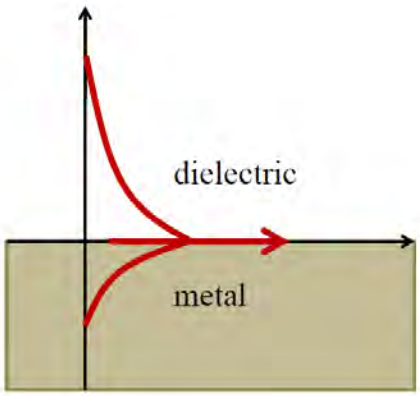

Figure 2.4: Propagation direction of the surface plasmon polariton is indicated by the red arrow. The field in the direction normal to the surface is evanescent in the dielectric and metal, which is indicated by the red lines.

and the component normal to the surface [26]

$$k_{\mathrm{SP}}^{\perp} = k_0 \sqrt{\frac{\epsilon_{\mathrm{q}}^2}{\hat{\epsilon}_2 + \epsilon_1}}\,, \tag{2.13}$$

where ϵ_1 and $\hat{\epsilon}_2 = \epsilon_2' + \mathrm{i}\epsilon_2''$ are the permittivities of the dielectric and metal, respectively, $k_0 = 2\pi/\lambda_0$ is the wave number in a vacuum, and ϵ_{q} with $q = 1, 2$ refer to either of the materials. Confinement to the surface demands that the field in the direction normal to the surface is evanescent. This is possible when the incident light has an electric field component normal to the interface and $\epsilon_2' < 0$ if $\epsilon_1 > 0$. At optical wavelengths, this condition is fulfilled by several metals, gold and silver being the most commonly used [5].

If we approximate the permittivity with Eq. (2.11) and if $\epsilon_2' < -\epsilon_1$, the wave vector component $k_{\mathrm{SP}}^{\parallel}$ becomes real and the surface plasmon propagates without attenuation. This is, however, approximately true for only some metals and only in the ultraviolet frequency range and frequencies below it. In general, the propagation constant is complex and the field in the propagation direction is attenuated. The real part of the propagation constant determines the

surface plasmon wavelength

$$\lambda_{SP} = \frac{2\pi}{\Re\{k_{SP}^{\parallel}\}} , \tag{2.14}$$

and the imaginary part determines the propagation 1/e decay length

$$l_{SP} = \frac{1}{2\Im\{k_{SP}^{\parallel}\}} . \tag{2.15}$$

The wave vector component parallel to the surface for light incident from the dielectric material is

$$k^{\parallel} = \sqrt{\epsilon_1} \sin\theta_1 \frac{2\pi}{\lambda_0} , \tag{2.16}$$

where θ_1 is the angle if incidence. In order to excite surface plasmons, the real parts of the propagation constant components given by Eq. (2.12) and (2.16) should be equal. Since $\epsilon_2' < 0$ and $\epsilon_1 > 0$, the real part of the propagation constant of the surface plasmon $k_{SP}^{\parallel}$ is greater than that of the field in the dielectric medium $k^{\parallel}$. This problem can be overcome, for example, using the famous Kretschmann configuration [27], which includes a prism placed on the metal surface. The light incident from the dielectric side to the prism experiences total internal reflection from the prism-metal interface and the generated evanescent wave couples with the surface plasmon mode.

If the surface is corrugated with a period d, the wave vector component parallel to the surface is [26]

$$k_c^{\parallel} = k^{\parallel} + m\frac{2\pi}{d} , \tag{2.17}$$

where $k^{\parallel}$ is defined by Eq. (2.16) and m is the diffraction order; its meaning is explained in the next chapter. The $k_c^{\parallel}$ may be tuned to match the wave vector given by Eq. (2.12). It should be noted that the dispersion relation in Eq. (2.12) hardly changes if the metal surface has a shallow corrugation.

If we assume that the corrugated surface lies on the xy-plane, the wave vector for a two-dimensional corrugated surface is

$$\boldsymbol{k}_{\mathrm{c}}^{\parallel} = \boldsymbol{k}^{\parallel} + m\frac{2\pi}{d_x}\hat{\boldsymbol{x}} + n\frac{2\pi}{d_y}\hat{\boldsymbol{y}} \,, \tag{2.18}$$

where d_x and d_y are the grating periods in the x- and y-directions, respectively, $\boldsymbol{k}^{\parallel}$ the parallel wave vector of the incident light, and m and n the diffraction orders. It follows from the generation of diffraction orders that surface plasmons may be excited with normally incident light in contrast to a non-corrugated surface. The same applies also in the case of one-dimensional corrugated surfaces.

2.2.3 Localized surface plasmons

For a small particle, with a size in the range of the penetration depth of the electromagnetic field into the metal, the clear distinction between surface and bulk plasmons vanishes. Let us consider a spherical metal particle with a diameter much smaller than the wavelength of light embedded in the dielectric material. From the Mie theory [28], by taking a first-order approximation we find the polarizability, a measure for how easily individual particle is polarized, inside the particle is

$$\alpha = 4\pi a^3 \frac{\hat{\epsilon}_2 - \epsilon_1}{\hat{\epsilon}_2 + 2\epsilon_1} \,, \tag{2.19}$$

where a is the radius of the particle, ϵ_1 the permittivity of the surrounding material and $\hat{\epsilon}_2$ the permittivity of the metal. If we assume that ϵ_2'' varies slowly along the frequency, the polarizability reaches its maximum when [25]

$$\epsilon_2' = -2\epsilon_1 \,. \tag{2.20}$$

The oscillation mode associated with this condition, which is in fact the lowest-order surface mode, has become known as the Fröhlich mode [12], which is illustrated in Fig. 2.5. If $\gamma \ll \omega_{\mathrm{p}}^2$, which is

usually true for most metals at room temperature, it follows from Eq. (2.9) that the frequency that satisfies Eq. (2.20) is

$$\omega_{\mathrm{F}} = \frac{\omega_{\mathrm{p}}}{\sqrt{1+2\epsilon_1}} , \tag{2.21}$$

which in air $\epsilon_1 = 1$ reduces to

$$\omega_{\mathrm{F}} = \frac{\omega_{\mathrm{p}}}{\sqrt{3}} . \tag{2.22}$$

The frequency ω_{F} is called the Fröhlich frequency.

The field inside the metal particle for which $a \ll \lambda$ is homogenous and therefore drives the electrons in a collective oscillative motion. When Eq. (2.20) is satisfied, the electric field is highly localized in the metallic particle. The quantum of the electron oscillation in the case of a highly localized electric field is called the localized surface plasmon or particle plasmon.

We may estimate the effect of the particle size by taking second-order approximation from Mie's theory. The resonance condition for the Fröhlich mode is then [12]

$$\epsilon_2' = -(2 + \frac{12}{5}x^2)\epsilon_1 , \tag{2.23}$$

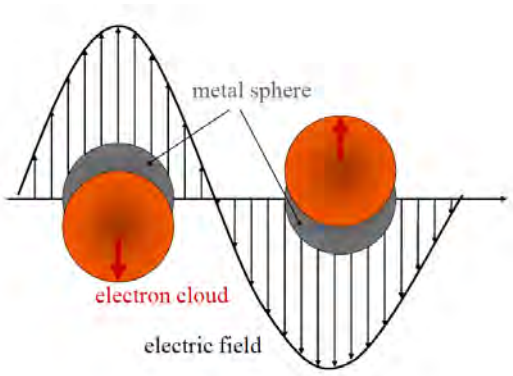

Figure 2.5: Electron oscillations in the Fröhlich mode corresponding to the dipole particle plasmon resonance.

where x is the so-called size parameter defined by

$$x = \frac{2\pi\sqrt{\epsilon_1}a}{\lambda} \, . \tag{2.24}$$

It may be concluded from Eq. (2.23) that the resonance frequency shifts to lower frequencies when the size of the sphere increases.

The Fröhlich mode is also known as the dipole mode. For larger particles higher-order modes also appear at different frequencies. The second lowest mode is the quadrupole mode, in which half of the electron cloud inside the metal moves parallel to the applied field and half moves antiparallel [29].

For a sphere, which is a symmetrical particle, the localized plasmons may be excited independently on the polarization of the applied field. However, in the case of an infinitely long cylinder, only a field with a component normal to the surface is capable of exciting plasmons. The resonance condition corresponding to Eq. (2.20) in an infinitely long cylinder illuminated by light polarized perpendicular to the cylinder axis is given by [30]

$$\frac{\epsilon_2'}{\epsilon_1} = -1 \, . \tag{2.25}$$

It is evident by comparing the resonance condition given by Eq. (2.20) and Eq. (2.25) that the shape of the particle has a significant influence on the resonance.

Let us consider a spherical dielectric inclusion in a metallic body. This is opposite to the problem that was solved by Eq. (2.20) and we may consider it simply by switching the permittivities, $\epsilon_2' \rightarrow \epsilon_1$ and $\epsilon_1 \rightarrow \epsilon_2'$. Then we obtain the resonance condition for a spherical void, or cavity, from [25]

$$\epsilon_2' = -\frac{1}{2}\epsilon_1 \, . \tag{2.26}$$

The resonance associated with Eq. (2.26) is called cavity plasmon resonance. The resonance condition for other shapes of cavities is obtained with a similar switch of permittivities.

2.3 OXIDATION

Valence electrons are responsible for chemical reactions such as oxidation. The natural tendency of two elements in the oxidation process is to obtain an octet, a state where the bonding has a total of eight valence electrons and does not undergo any further chemical reactions. Since metals have only 1–3 valence electrons, they react easily with oxygen, except this is not the case for the most noble metals.

The bonding between oxygen and the metal is defined by the electronegativity difference of the elements. Usually the resulting bonding is mostly ionic in nature, which means that the oxygen receives electrons from the metal and it is held together by electrostatic forces. Some of the most common metal oxides are titanium oxide TiO_2, aluminum oxide Al_2O_3, chromium oxide Cr_2O_3, which is formed, for example, on stainless steel, and iron oxide Fe_2O_3, also known as rust.

2.4 SUMMARY

In this chapter we discussed the optical and chemical properties of metals originating from the electronic structure characteristic to different elements. The optical properties, fundamentally microscopic by nature, are presented in the next chapter in their effectively macroscopic forms — the refractive index and permittivity.

3 Electromagnetic theory of light

Electromagnetic theory expresses light as vectorial electromagnetic waves. The theory ignores the essence of light as particles, therefore excluding atomic-level processes, but describes the behavior of light accurately in other cases. A set of equations combined from the theories of electricity and magnetism by James Clerk Maxwell form the basis for the electromagnetic theory of light. Maxwell's equations together with constitutive relations, which describe the behavior of substances under the influence of light, can be exploited to derive analytic tools for light propagation in a homogeneous medium and a periodic structure.

3.1 LIGHT IN HOMOGENOUS MEDIUM

Optical properties are independent of their position in a homogeneous medium. Let us consider a stationary and time-harmonic field. An electric field vector may be represented as the sum of monochromatic fields

$$\boldsymbol{E}(\boldsymbol{r},t) = \Re\left\{\int_{-\infty}^{\infty} \boldsymbol{E}(\boldsymbol{r},\omega)\exp(-\mathrm{i}\omega t)\mathrm{d}\omega\right\}, \tag{3.1}$$

where $\Re$ is the real part, $\boldsymbol{r}$ the position, i imaginary unit, ω the angular frequency and each component of the complex amplitude vector, $\boldsymbol{E}(\boldsymbol{r},\omega)$, may be written in the form

$$E_j(\boldsymbol{r},\omega) = |E_j(\boldsymbol{r},\omega)|\exp\{\mathrm{i}\arg[E_j(\boldsymbol{r},\omega)]\}, \tag{3.2}$$

where $j = \{x,y,z\}$, $|E_j(\boldsymbol{r},\omega)|$ is the modulus of the complex amplitude vector, and $\arg[E_j(\boldsymbol{r},\omega)]$ the phase of the complex amplitude component. An analogous expression may be written for magnetic field $\boldsymbol{H}(\boldsymbol{r},t)$, electric displacement $\boldsymbol{D}(\boldsymbol{r},t)$, magnetic induction $\boldsymbol{B}(\boldsymbol{r},t)$, and current density $\boldsymbol{J}(\boldsymbol{r},t)$. [31]

3.1.1 Maxwell's equations

The time-harmonic field in a homogeneous material satisfies Maxwell's equations. The time-independent form of the equations are [32–34]

$$\nabla \times \boldsymbol{E}(\boldsymbol{r},\omega) = \mathrm{i}\omega \boldsymbol{B}(\boldsymbol{r},\omega)\ , \tag{3.3}$$

$$\nabla \times \boldsymbol{H}(\boldsymbol{r},\omega) = \boldsymbol{J}(\boldsymbol{r},\omega) - \mathrm{i}\omega \boldsymbol{D}(\boldsymbol{r},\omega)\ , \tag{3.4}$$

$$\nabla \cdot \boldsymbol{D}(\boldsymbol{r},\boldsymbol{\omega}) = \rho(\boldsymbol{r},\omega)\ , \tag{3.5}$$

$$\nabla \cdot \boldsymbol{B}(\boldsymbol{r},\omega) = 0\ , \tag{3.6}$$

where $\rho(\boldsymbol{r},\omega)$ is the electric charge density. The simplest solution to Maxwell's equations is a plane wave. If a monochromatic plane wave propagates along the z-axis, the expression for the electric field is

$$\boldsymbol{E}(\boldsymbol{r},t) = \boldsymbol{E}(z,t) = \Re\{(E_x\hat{\boldsymbol{x}} + E_y\hat{\boldsymbol{y}})\exp(\mathrm{i}kz)\exp(-\mathrm{i}\omega t)\}\ , \tag{3.7}$$

where E_x and E_y are the complex amplitude components of the electric field and $\hat{\boldsymbol{x}}$ and $\hat{\boldsymbol{y}}$ the unit vectors in x- and y-direction, respectively. Wavenumber, k, is defined by $k = 2\pi/\lambda$, where λ is the wavelength of light. In dealing with linear mathematical operations, such as addition, differentiation, and integration, usually the complex representation of the field instead of the real representation is considered which facilitates the mathematical treatment.

3.1.2 Poynting vector

The energy flow of the electromagnetic field is described by the Poynting vector

$$\boldsymbol{S}(\boldsymbol{r},t) = \boldsymbol{E}(\boldsymbol{r},t) \times \boldsymbol{H}(\boldsymbol{r},t). \tag{3.8}$$

The magnitude of a time-averaged Poynting vector at certain point $\boldsymbol{r}$

$$\langle \boldsymbol{S}(\boldsymbol{r},t)\rangle = \frac{1}{2}\Re\{\boldsymbol{E}(\boldsymbol{r}) \times \boldsymbol{H}^*(\boldsymbol{r})\} \tag{3.9}$$

if often considered as representing the intensity of the electromagnetic field, and its direction is taken to define the direction of the energy flow. Such a pointwise interpretation is, however, completely

unambiguous only in case of a single plane wave. Whenever interference is involved, the physical interpretation is less straightforward and particular caution should be exercised in cases where the electromagnetic field changes rapidly in scales of the order of the optical wavelength.

3.1.3 Polarization

The electric field of a plane wave can always be represented using two orthogonal components. The state of polarization describes the relationship between the amplitudes and phase differences of these two components. If a plane wave is incident on a surface, the component that is perpendicular to the plane of incidence, which is spanned by the wave vector and the normal of the surface, is called the TE (transverse electric) component. The component parallel to the plane of incidence is called the TM (transverse magnetic) component. The geometry is illustrated in Fig. 3.1.

If the phase difference, δ, between the components is a multiple of π, $\delta = \arg E_y - \arg E_x = m\pi$, the field is said to be linearly polarized. When the amplitudes are equal $|E_x| = |E_y|$ and the phase difference is $\delta = \pi/2 \pm 2m\pi$, the field is left-handed circularly polarized; it is right-handed circularly polarized when the phase difference $\delta = -\pi/2 \pm 2m\pi$. In other cases, the field is elliptically polarized.

3.1.4 Constitutive relations

If we assume that the medium is linear and isotropic, the constitutive relations that connect the complex amplitudes of the magnetic field, the electric field, electric displacement, magnetic induction, and the current density can be represented as

$$\boldsymbol{D}(\boldsymbol{r},\omega) = \epsilon(\boldsymbol{r},\omega)\boldsymbol{E}(\boldsymbol{r},\omega)\ , \tag{3.10}$$

$$\boldsymbol{B}(\boldsymbol{r},\omega) = \mu(\boldsymbol{r},\omega)\boldsymbol{H}(\boldsymbol{r},\omega)\ , \tag{3.11}$$

$$\boldsymbol{J}(\boldsymbol{r},\omega) = \sigma(\boldsymbol{r},\omega)\boldsymbol{E}(\boldsymbol{r},\omega)\ , \tag{3.12}$$

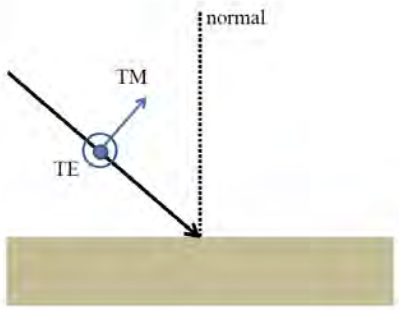

Figure 3.1: Electric field of a plane wave can always be divided into TE and TM components. The former is perpendicular to the plane of incidence and the latter is parallel. The black arrow represents the propagation direction of the field.

where $\epsilon(\boldsymbol{r},\omega)$ is the electric permittivity, $\mu(\boldsymbol{r},\omega)$ magnetic permeability, and $\sigma(\boldsymbol{r},\omega)$ electric conductivity [31]. The permittivity and permeability can be written as $\epsilon(\boldsymbol{r},\omega) = \epsilon_r(\boldsymbol{r},\omega)\epsilon_0$ and $\mu(\boldsymbol{r},\omega) = \mu_r(\boldsymbol{r},\omega)\mu_0$, respectively, where ϵ_r is the relative permittivity, ϵ_0 the permittivity of the vacuum, μ_r the relative permeability, and μ_0 the permeability of the vacuum. In this thesis only non-magnetic media are considered, for which $\mu_r = 1$. Maxwell's equations together with the constitutive relations imply that we need to solve only two of the vectorial electric or magnetic field components to obtain the remaining four.

3.1.5 Boundary conditions

Maxwell's equations are valid only in a continuous medium. The field across an interface between two media must follow the boundary conditions that can be deduced from Maxwell's equations using the Gauss and Stokes theorems [31].

Let us denote the field approaching a certain point from different sides of the boundary with the subscripts 1 and 2 and the normal unit vector at the boundary with $\hat{\boldsymbol{n}}_{12}$, which points from

medium 1 to medium 2. It follows from the boundary conditions

$$\hat{\boldsymbol{n}}_{12} \cdot [\boldsymbol{B}_1(\omega) - \boldsymbol{B}_2(\omega)] = 0 \,, \tag{3.13}$$

$$\hat{\boldsymbol{n}}_{12} \cdot [\boldsymbol{D}_1(\omega) - \boldsymbol{D}_2(\omega)] = \rho_s(\omega) \,, \tag{3.14}$$

$$\hat{\boldsymbol{n}}_{12} \times [\boldsymbol{E}_1(\omega) - \boldsymbol{E}_2(\omega)] = \boldsymbol{0} \,, \tag{3.15}$$

$$\hat{\boldsymbol{n}}_{12} \times [\boldsymbol{H}_1(\omega) - \boldsymbol{H}_2(\omega)] = \boldsymbol{J}_s(\omega) \,, \tag{3.16}$$

where $\rho_s(\omega)$ is the electric charge density on the surface and $\boldsymbol{J}_s(\omega)$ the current density on the surface, that the tangential components of the electric and magnetic field and the normal components of electric displacement and magnetic induction are continuous across the boundary. If 2 is perfectly conducting, in another words $\sigma \to \infty$, the fields are zero inside the medium, $\boldsymbol{B}_2(\boldsymbol{r}, \omega) = \boldsymbol{D}_2(\boldsymbol{r}, \omega) = \boldsymbol{E}_2(\boldsymbol{r}, \omega) = \boldsymbol{H}_2(\boldsymbol{r}, \omega) = 0$.

3.1.6 Electromagnetic field at interface

The TE and TM components are reflected and transmitted with different efficiencies when light is incident at an oblique angle to an interface. The reflectance and transmittance of light from a interface may be calculated with Fresnel's coefficients, which are derived from the boundary conditions Eqs. (3.13)–(3.16). The relationship between the incident and reflected electric field complex amplitudes is given by

$$r_{\mathrm{TE}} = \frac{n_{\mathrm{i}} \cos\theta_{\mathrm{i}} - n_{\mathrm{t}} \cos\theta_{\mathrm{t}}}{n_{\mathrm{i}} \cos\theta_{\mathrm{i}} + n_{\mathrm{t}} \cos\theta_{\mathrm{t}}} \,, \tag{3.17}$$

for TE-polarized light, where n_{i} is the refractive index at the input side, n_{t} the refraction index in the transmission side, θ_{i} the incidence angle, and θ_{t} the refraction angle.

The relationship between the transmitted and incident complex amplitudes for TE-polarized light is

$$t_{\mathrm{TE}} = \frac{2 n_{\mathrm{i}} \cos\theta_{\mathrm{i}}}{n_{\mathrm{i}} \cos\theta_{\mathrm{i}} + n_{\mathrm{t}} \cos\theta_{\mathrm{t}}} \,. \tag{3.18}$$

The corresponding coefficients for the TM component are

$$r_{\mathrm{TM}} = \frac{n_{\mathrm{t}} \cos\theta_{\mathrm{i}} - n_{\mathrm{i}} \cos\theta_{\mathrm{t}}}{n_{\mathrm{t}} \cos\theta_{\mathrm{i}} + n_{\mathrm{i}} \cos\theta_{\mathrm{t}}} \,, \tag{3.19}$$

and

$$t_{\mathrm{TM}} = \frac{2n_{\mathrm{i}} \cos\theta_{\mathrm{i}}}{n_{\mathrm{i}} \cos\theta_{\mathrm{t}} + n_{\mathrm{t}} \cos\theta_{\mathrm{i}}} \,. \tag{3.20}$$

The expressions for reflected and transmitted irradiance are

$$R_{\mathrm{TE}} = |r_{\mathrm{TE}}|^2 \,, \tag{3.21}$$

$$T_{\mathrm{TE}} = \frac{n_{\mathrm{t}} \cos\theta_{\mathrm{t}}}{n_{\mathrm{i}} \cos\theta_{\mathrm{i}}} |t_{\mathrm{TE}}|^2 \,, \tag{3.22}$$

$$R_{\mathrm{TM}} = |r_{\mathrm{TM}}|^2 \,, \tag{3.23}$$

$$T_{\mathrm{TM}} = \frac{n_{\mathrm{t}} \cos\theta_{\mathrm{t}}}{n_{\mathrm{i}} \cos\theta_{\mathrm{i}}} |t_{\mathrm{TM}}|^2 \,, \tag{3.24}$$

where r_{TE}, r_{TM}, t_{TE} and t_{TM} may be either complex or real.

3.1.7 Angular spectrum representation

Since a plane wave satisfies the Maxwell's equations, so does superposition of plane waves [35, 36]. Using this knowledge in Fourier analysis, we obtain a description for the propagation of an arbitrary electromagnetic field in a homogeneous medium.

Let us consider an electromagnetic field propagating from plane $z = z_0$ into a parallel plane $z > z_0$. Assuming that no sources in the half space $z_0 > 0$ exist, we obtain an expression for any scalar component $U_{\mathrm{s}}(x, y, z; \omega)$ of the field at plane z, so that $z > z_0$ [35]

$$U_{\mathrm{s}}(x, y, z; \omega) = \iint_{-\infty}^{\infty} A_{\mathrm{s}}(k_x, k_y; \omega) \exp[\mathrm{i}(k_x x + k_y y + k_z \Delta z)] \mathrm{d}k_x \mathrm{d}k_y \tag{3.25}$$

where $\Delta z = z - z_0$ and

$$A_{\mathrm{s}}(k_x, k_y; \omega) = \frac{1}{(2\pi)^2} \iint_{-\infty}^{\infty} U_{\mathrm{s}}(x, y, z_0; \omega) \exp[-\mathrm{i}(k_x x + k_y y)] \, \mathrm{d}x \mathrm{d}y \tag{3.26}$$

is the angular spectrum of the field at $z = z_0$. According to the angular spectrum representation, the field may be expressed as a superposition of plane waves propagating in directions determined

by the components (k_x, k_y, k_x) of wave vector $\boldsymbol{k}$ and the complex amplitudes of the plane waves are given in Eq. (3.26). The z-component of the wave vector can be written

$$k_z = \begin{cases} [k^2 - (k_x^2 + k_y^2)]^{1/2} , & \text{when } k_x^2 + k_y^2 \leq k^2 , \\ \mathrm{i}[(k_x^2 + k_y^2) - k^2]^{1/2}, & \text{when } k_x^2 + k_y^2 > k^2 . \end{cases} \tag{3.27}$$

The solution of Eq. (3.25) contains two types of waves. The real root in Eq. (3.27) represents plane waves that propagate in the direction given by the wave vector $\boldsymbol{k}$ whereas the imaginary root represents exponentially decaying fields, known as evanescent waves.

3.2 LIGHT IN PERIODIC STRUCTURE

In periodic structure both the field and permittivity may be expanded into a Fourier series. With this as the starting point when solving Maxwell's equations and the boundary conditions, an exact representation of the field in the periodic region is obtained. In this section we consider the behavior of the electromagnetic field in diffraction gratings, which are the most fundamental periodic elements in wave optical engineering.

3.2.1 Diffraction gratings

The characteristic property of diffraction gratings is that when illuminated by a plane wave, the field is reflected and transmitted in discrete directions, referred to as diffraction orders.

Let us consider the grating geometry represented in Fig. 3.2. Region I, where $z < 0$, and region III, where $z > h$, are homogeneous and the relative permittivities are $\epsilon_{\mathrm{I}} = n_{\mathrm{I}}^2$ and $\epsilon_{\mathrm{III}} = n_{\mathrm{III}}^2$, respectively. The grating lies in the modulated region $0 < z < h$ with two permittivities, ϵ_1 and ϵ_2. The permittivities ϵ_{III}, ϵ_1, and ϵ_2 may be either real or complex. The relative permittivity of the modulated region may be written

$$\epsilon_r(x, y, z; \omega) = \epsilon_r(x + d_x, y + d_y, z; \omega) , \tag{3.28}$$

when d_x and d_y are the grating periods in the x- and y-directions, respectively.

The field in regions I and III is pseudo-periodic and satisfies the Floquet–Bloch condition for each scalar component [23, 37]

$$U_{\mathrm{s}}(x+d_x, y+d_y, z;\omega) = U_{\mathrm{s}}(x,y,z;\omega)\exp[\mathrm{i}(k_{x0}d_x + k_{y0}d_y)]\ , \quad (3.29)$$

according to which the field is periodic with a period $d_x \times d_y$ apart from the phase factor $\exp[\mathrm{i}(k_{x0}d_x + k_{y0}d_y)]$. In Eq. (3.29) k_{x0} and k_{y0} are the x- and y-components of the wave vector of the incident light.

It follows from the Floquet–Bloch condition that the wave vector components for a reflected and transmitted field can only have the discrete values

$$k_{xm} = k_{x0} + 2\pi m/d_x\ , \quad (3.30)$$

$$k_{yn} = k_{y0} + 2\pi n/d_y\ , \quad (3.31)$$

where m and n are integers corresponding to the m^{th} and n^{th} diffraction orders. Furthermore, the angular spectrum is also discrete and may be expressed as the discrete sum of the plane waves instead of the integral.

Let us assume that a unit-amplitude plane wave light source with the vacuum wavelength λ_0 exists in the half space $z < 0$. The

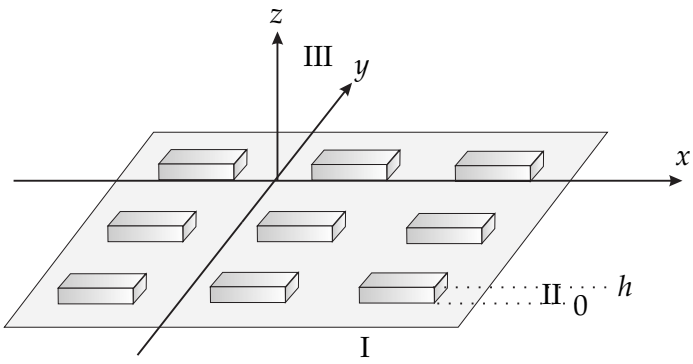

Figure 3.2: The grating geometry.

electric fields in regions I and III may then be expressed as a superposition of plane waves corresponding to different diffraction orders [38]

$$\begin{aligned} \boldsymbol{E}_{\mathrm{I}}(x,y,z;\omega) = \hat{\boldsymbol{u}}_0 \exp[\mathrm{i}(k_{x0}x + k_{y0}y + k_{z00}z)] \\ + \sum_{mn} \boldsymbol{r}_{mn} \exp[\mathrm{i}(k_{xm}x + k_{yn}y - k^{-}_{zmn}z)] \end{aligned} \tag{3.32}$$

in region I and

$$\boldsymbol{E}_{\mathrm{III}}(x,y,z;\omega) = \sum_{mn} \boldsymbol{t}_{mn} \exp \mathrm{i}[k_{xm}x + k_{yn}y + k^{+}_{zmn}(z-h)] \tag{3.33}$$

in region III, where $\boldsymbol{r}_{mn}$ and $\boldsymbol{t}_{mn}$ are the complex amplitudes of the diffracted field and $\hat{\boldsymbol{u}}_0$ is the unity complex amplitude vector. The wave vector components in Eq. (3.32) are defined by $k_{x0} = n_{\mathrm{I}} k_0 \sin\theta\cos\phi$, $k_{y0} = n_{\mathrm{I}} k_0 \sin\theta\sin\phi$, and $k_{z00} = n_{\mathrm{I}} k_0 \cos\theta$, when $k_0 = 2\pi/\lambda_0$ is the wave number of the incident light. The z-components k^{-}_{zmn} and k^{+}_{zmn} are defined by

$$k^{-}_{zmn} = [(k_0 n_{\mathrm{I}})^2 - k^2_{xm} - k^2_{yn}]^{1/2} , \tag{3.34}$$

$$k^{+}_{zmn} = [(k_0 n_{\mathrm{III}})^2 - k^2_{xm} - k^2_{yn}]^{1/2} . \tag{3.35}$$

The incident angle θ between the wave vector $\boldsymbol{k}_0$ and the z-axis, the conical angle ϕ, polarization angle ψ, and the polarization vector $\hat{\boldsymbol{u}}$

$$\begin{aligned} \hat{\boldsymbol{u}} = (\cos\psi\cos\theta\cos\phi - \sin\psi\sin\phi)\hat{\boldsymbol{x}} \\ + (\cos\psi\cos\theta\sin\phi + \sin\psi\cos\phi)\hat{\boldsymbol{y}} \\ - \cos\psi\sin\theta\hat{\boldsymbol{z}} \end{aligned} \tag{3.36}$$

are represented in Fig. 3.3. The corresponding expressions for the magnetic field are given by Eqs. (3.3), (3.4), and (3.11).

The propagation directions for the transmitted plane waves can be deduced from the condition

$$k_0 n_{\mathrm{III}} \cos\theta_{mn} = k^{+}_{zmn}, \tag{3.37}$$

when the grating equation for transmitted diffraction orders is

$$\begin{aligned} k_0^2 n_{\mathrm{III}}^2 \sin^2\theta_{mn} = (k_0 n_{\mathrm{I}} \sin\theta\cos\phi + 2\pi m/d_x)^2 \\ + (k_0 n_{\mathrm{I}} \sin\theta\sin\phi + 2\pi n/d_y)^2 . \end{aligned} \tag{3.38}$$

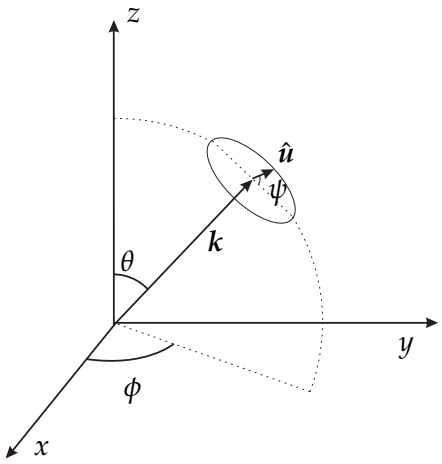

Figure 3.3: The incidence angle θ, conical angle ϕ, wave vector $\mathbf{k}$, polarization angle ψ, and polarization vector $\hat{\mathbf{u}}$.

Correspondingly, for the reflected diffraction orders it holds that

$$k_0^2 n_\mathrm{I}^2 \sin^2\theta_{mn} = (k_0 n_\mathrm{I} \sin\theta\cos\phi + 2\pi m/d_x)^2 + (k_0 n_\mathrm{I} \sin\theta \sin\phi + 2\pi n/d_y)^2 \,. \tag{3.39}$$

The one-dimensional grating equations are obtained when d_x or d_y approaches infinity and angle $\phi = 0$.

The diffraction efficiencies for reflected and transmitted diffraction orders are obtained from

$$\eta_{rmn} = \Re\{k_{zmn}^-/k_{z00}^-\}|\boldsymbol{r}_{mn}|^2 \,, \tag{3.40}$$

$$\eta_{tmn} = \Re\{k_{zmn}^+/k_{z00}^+\}|\boldsymbol{t}_{mn}|^2 \,, \tag{3.41}$$

where $\Re\{k_{zmn}^-/k_{z00}^-\}$ and $\Re\{k_{zmn}^+/k_{z00}^+\}$ are scaling factors that arise from the energy conservation as the cross-section projections of the incident and diffracted beams change when the propagation angles of the beams change.

3.2.2 Fourier modal method

We are usually interested in solving the complex amplitudes of the transmitted and reflected diffraction orders in Eqs. (3.32) and (3.33)

and the field distribution in the three regions. However, in most cases no analytical solution can be found and many numerical rigorous methods, such as the Rayleigh [38], Integral [39], FDTD [40], and Coordinate transform method [41] have been presented to solve the problem.

In this thesis we use the Fourier modal method (FMM) [42–45], which, according to its name, expands the periodic electric permittivity and field in the modulated grating area as a Fourier series. The field inside the modulated grating area is expressed as the superposition of waveguide modes and is of pseudoperiodic form. The Fourier coefficients as well as the wave vector z-components of the modes are solved numerically from an eigenvalue equation. The complex amplitudes of the reflected and transmitted field are obtained matching the field inside and outside the grating region by means of the boundary conditions and using S-matrix algorithm [46, 47]. In the Fourier expansions the infinite number of summations must be truncated into a finite number, which determines the accuracy of the solution. For a converged result, all the propagating modes and a sufficient number of evanescent modes must be included in the calculation.

The Fourier modal method is suitable for binary gratings and can also be applied to non-binary structures by dividing the grating profile into binary slabs. Both one- and two-dimensional gratings and both metallic and dielectric grating materials can be dealt with the method. However, the implementation of FMM between dielectric and metallic gratings is somewhat different. Due to the larger contribution of evanescent fields, the number of modes taken into account in the calculations is higher for metals, especially in the case of surface plasmons, for which the field is evanescent at both sides of the interface.

3.2.3 Grating anomalies

Sudden changes in the electromagnetic fields with respect to physical parameters such as the wavelength of the incident field or the

angle of incidence associated with diffraction gratings are called Wood's anomalies. There are two principal types of anomalous effects; the Rayleigh type and the resonance type. The Rayleigh type occurs when one of the diffraction orders propagates parallel to the surface. This corresponds to the situation $\theta_{mn} = 90$ in Eq. (3.38). The Rayleigh anomaly condition for the appearance/disappearence of the $(m,n)^{\text{th}}$ diffracted order for light incident in the zy-plane is obtained from Eq. (3.38) by setting $\theta_{mn} = 90$ and $\phi = 0$

$$\frac{n_{\text{III}}^2}{\lambda_0^2} = \left(\frac{m}{d_x}\right)^2 + \left(\frac{n_{\text{I}} \sin\theta}{\lambda_0} + \frac{n}{d_y}\right)^2. \tag{3.42}$$

The second anomaly is called guided-mode resonance and is due to the coupling of the diffracted fields to the modes propagating in the modulated grating region that acts as a waveguide. [48]

3.2.4 Effective medium theory

When the feature size of a grating is substantially smaller than the wavelength of the incident light, the grating may be treated as a homogeneous thin film with an effective refractive index defined by the grating structure. Then, only the zeroth reflected and transmitted diffraction orders propagate. If the permittivity distribution of the grating is not symmetric, the effective refractive index is dependent on the direction and the grating may be approximated as an effectively anisotropic thin film. Treating the grating as an effective medium makes the solution of the grating problem much faster since the reflected and transmitted energy may be evaluated from the Fresnel's coefficients [31]. Effective medium description also provides physical insight into the behavior of light in subwavelength gratings.

Let us consider a one-dimensional y-invariant linear grating profile, illustrated in Fig. 3.4, where the refractive index profile is defined by

$$n(x) = \begin{cases} n_1, & \text{when } 0 < x < g \\ n_2, & \text{when } g < x < d. \end{cases} \tag{3.43}$$

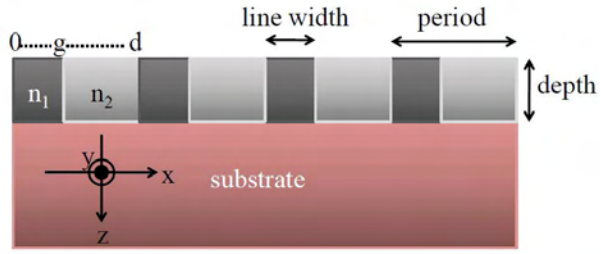

Figure 3.4: One dimensional y-invariant linear grating. n_1 and n_2 denote the refraction indexes of the modulated grating region.

From the theory of periodic waveguides [45] we know that the effective refractive index is defined by the z-component of the wave vector, it is the propagation constant, γ, divided by the wave number

$$\hat{n}_{\text{eff}} = \gamma / k. \tag{3.44}$$

Bearing this in mind and considering only the zeroth order modes in the eigenvalue equation mentioned in the previous section, we obtain the approximation for the effective refractive index [49]

$$\hat{n}_{\perp}^{\text{eff}} = [f n_1^{-2} + (1-f) n_2^{-2}]^{-1/2}\,, \tag{3.45}$$

for a field polarized perpendicularly to the grating lines, where the fill factor $f = g/d$. For a field polarized parallel to the grating lines we obtain

$$\hat{n}_{\parallel}^{\text{eff}} = [f n_1^2 + (1-f) n_2^2]^{1/2}\,. \tag{3.46}$$

Expressions for the effective refractive index also exist for two-dimensional structures [50, 51], but the approximations are not as accurate as in the one-dimensional case.

3.3 SUMMARY

In this chapter we represented the theoretical tools for analysing light propagation in homogenous and nano- and microstructured elements. In the next chapter we shall consider the fabrication and characterization techniques for these structures.

4 Fabrication and characterization of metallic nanostructures

Fabrication techniques for nano- and micro-optical devices have improved significantly since 1876, when David Rittenhouse made the first grating by wrapping fine wire between a pair of 0.25 mm pitch screws [52]. The feature size has decreased down to ten nanometers using electron beam lithography [53, 54] and techniques such as DNA self-assembling [55] seem to reduce it even further. In this thesis we have used two very different fabrication techniques: the electron beam lithography and laser-marking. In addition, thin film deposition and a versatile optical characterization technique, ellipsometry, are described.

4.1 THIN FILM DEPOSITION

Thin film deposition is an important step in nano- and microstructure fabrication. Two widely used thin film deposition techniques are atomic layer deposition [56] and thermal evaporation [57, 58]. Due to their different physical mechanisms to grow the film, they result in different physical structures. The physical structure of the film is of great importance since it affects the optical properties and further processability of the film (see **Paper I**), [59].

4.1.1 Atomic layer deposition

Atomic layer deposition (ALD) may be employed to grow oxide, nitride, and metal films [60]. In the process two or more precursors react chemically with each other and form one monolayer of the desired material. The precursors are led into a vacuum chamber

in turns and after each precursor pulse the chamber is purged by an inert gas. These steps are repeated until the desired thickness is achieved.

The temperature, pressure of the chamber, and other process parameters are adjusted according to the process chemistry and targeted film properties. For example, with increasing temperature the reactions become more complete and the impurity content decreases, which leads to higher refractive indexes. [56, 61, 62]

ALD is a very precise method for growing thin films because it allows us to adjust the film thickness by one atomic layer at a time. Depending on the process, one cycle produces a 0.1–3 Å film thickness [62]. Due to this atomic scale precise control, the microstructure of the deposited film is dense and conformal.

4.1.2 Thermal evaporation

The objective of evaporation is to transfer atoms from a heated target to a substrate. The target material is heated to the evaporation point and the thermal energy is transferred to the kinetic energy of the evaporated atoms that impinge on the substrate. [63] The target may be heated by an electron beam or resistively in a boat by passing an electric current through it.

One significant difference between ALD and thermal evaporation is that the microstructure of evaporated film changes significantly along the film thickness. The structural evolution for evaporated films starts with the adsorption of atoms on the surface and is followed by the condensation of the adsorbed atoms, adatoms. The condensation of the adatoms is also referred to as nucleation. The nuclei grow into islands until they coalesce into each other and form a continuous network of grains. [64, 65]

The development of the grain structure is determined mainly by the surface mobility of the adatoms relative to the deposition rate and the substrate temperature relative to the melting temperature of the film material. As a rule, higher substrate temperatures and lower deposition rates lead to larger grain size [66]. In face-

centered-cubic metals such as aluminum, silver, gold, copper and iridium, the surface mobility of the adatoms is high and the structure continues to evolve during the thickening of the film. The final grain size is typically on the order of the film thickness. Another type of material includes refractory metals and elements with a diamond-cubic crystal structure such as silicon, chromium and iron. They have a lower surface mobility and the resulting microstructure consists of vertically long pillars. [67]

The resulting thin film for both material types consists of grains which are separated by grain boundaries. The space between the grain boundaries is filled with impurities such as nitrogen and oxygen that originate from the vacuum chamber. Therefore, the amount of space between the grain boundaries and the quality of the vacuum impact on the optical properties of the evaporated thin film.

4.2 ELECTRON-BEAM LITHOGRAPHY

Electron-beam lithography is a process with several steps. First, a resist is exposed to an electron beam. In the case of a positive polymer resist, electrons break chemical bondings so that long polymer chains are fragmented into monomers; in the case of a negative monomer resist the electrons polymerize the resist [68]. The exposure is followed by a development of the resist by immersing the sample in solvent or spraying or puddling it. The development liquid dissolves the monomer regions so that the negative or the positive of the exposed pattern is left. The remaining resist residues are removed with oxygen plasma in a reactive ion etcher chamber. The pattern from the empty openings in the resist is etched into a layer underneath the resist by dry or wet etching. In case of dry etching the material is removed by bombarding it with plasma whereas in the case of wet etching the material is etched with a liquid chemical. After the etching process the residues of the resist that worked as a mask are removed, for example, with oxygen plasma etching and in the simplest case the sample is complete.

Metallic gratings may be fabricated by performing the steps described above. However, it is important to note that the quality of the metal film plays a crucial role in the etching step. The metal film may be porous if it is deposited by thermal evaporation. In the case of aluminum, the porous film structure contains a high amount of aluminum oxide, which is one of the hardest materials on earth, and may result in incomplete etching [69].

Metallic gratings may also be fabricated by coating the patterned resist and the openings with a metal layer. The resist and the metal layer on top of it are then removed by immersing the sample in solvent while the metal layer in the openings remains on the substrate. These two steps together are called the lift-off method; it is also suitable for obtaining a mask for deep structures [70]. For the fabrication of gold gratings lift-off is the only feasible method [69].

4.3 LASER MARKING

Fabrication of microstructured elements with the laser-marking technique is very straightforward compared to electron-beam lithography. The structure is achieved by heating the surface with a laser so that the surface material is evaporated or sublimated. This process is also referred to as ablation. The heating of the surface may also trigger a chemical reaction with the oxygen in the air and result in the formation of a thin oxide layer. The occurrence of these two phenomena depends on the energy absorbed by the surface. Higher energies lead to ablation. Below the ablation threshold, the thickness of the native oxide layer on the metal increases along with the energy density.

The initial oxide layer is developed through adsorption and chemisorption of oxygen on the metal surface. Further oxide growth can proceed via electron and ion diffusion through the oxide layer. [71] Because of the diffusion mechanism, the layer growth is self-limiting and saturates at a certain thickness. However, if the surface is heated, as in the case of laser-marking, the diffusion is enhanced and the layer continues to grow.

The energy and therefore the heat on the surface may be conveniently adjusted by a pulsed laser. The energy is dependent on the laser power, pulse length, pulse repetition frequency, diameter of the beam, laser scanning velocity, and the line spacing between adjacent scans. Usually the beam intensity distribution is gaussian or semi-gaussian but in order to obtain an oxide layer of uniform thickness, the beam intensity profile should have the shape of a flat-top. In case of the flat-top profile, the energy, E, accumulating in area, A, may be calculated from

$$E = IAt \,, \tag{4.1}$$

where I is the intensity of the beam and t the time the surface is heated. The average power of the pulse is defined by the relationship of the laser power, P_l, and the repetition frequency of the pulses, f,

$$P_\mathrm{p} = \frac{P_\mathrm{l}}{f} \tag{4.2}$$

and the pulse interval is

$$t_\mathrm{p} = \frac{1}{f} \,. \tag{4.3}$$

4.4 ELLIPSOMETRY

An ellipsometer, according to its name, measures the ellipticity of the polarization state of light reflected from a measured surface. More accurately, the measured values ψ and δ are defined by

$$\tan\psi e^{\mathrm{i}\delta} = \frac{\hat{r}_\mathrm{TM}}{\hat{r}_\mathrm{TE}} \,, \tag{4.4}$$

where $\hat{r}_\mathrm{TM}$ and $\hat{r}_\mathrm{TE}$ are the Fresnel reflection coefficients for the sample. If the measured sample is thin film, the Fresnel coefficients are calculated by summing the coefficients in Eqs. (3.17) and (3.19) coherently for beams that reflect a number of times from the back and top surface of the film. In the case of bulk material only one

reflection needs to be considered. [72] An ellipsometer may be employed to determine the refractive index, thickness and reflectance and transmittance of the sample.

The evaluated refractive indexes must satisfy the ellipsometric equation Eq. (4.4). When dielectric material is measured over a certain wavelength range, we are usually interested in finding refractive indexes with dispersion described by the Cauchy's relation

$$n(\lambda) = A + \frac{B}{\lambda^2} + \frac{C}{\lambda^4} , \tag{4.5}$$

where A, B, and C are the adjusted parameters. The parametric model for metals consists of the sum of the Drude and Lorentz oscillators defined by Eqs. (2.8) and (2.9). In addition, the Kramers-Kronig relation between the imaginary and real part of the refractive index may be applied to determine the solution.

If no parametric model is used, the refractive indexes are evaluated by using an initial estimate from the refraction indexes of an already known material. Then, the solution is given by the refraction indexes that are closest to the initial estimate and satisfy the ellipsometric equation Eq. (4.4).

The correspondence of ψ and δ generated by the calculated refractive indexes between the measured ψ and δ is evaluated by the root mean square error (RMSE). Refraction indexes resulting in the smallest error are the solution for Eq. (4.4). The RMSE is calculated with numerical iterative Levenberg–Marquardt algorithm [73].

The ellipsometer may also be used to measure change in the polarization state for transmitted light. If the light incident on the sample is linearly polarized, the ellipticity, χ, and polarization rotation angle, θ, for transmitted light, defined in Fig. 4.1, can be obtained from simple equations [74]

$$\tan[2(45^\circ - \theta)] = \tan 2\psi \cos\delta \tag{4.6}$$

and

$$\sin 2\chi = \sin 2\psi \sin\delta , \tag{4.7}$$

where ψ and δ are defined as in Eq. (4.4) except that the Fresnel reflection coefficients are replaced by transmission coefficients.

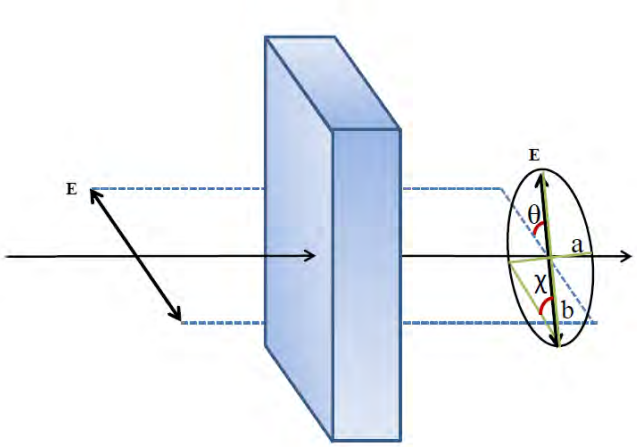

Figure 4.1: Ellipticity, χ, defined by $\arctan \chi = a/b$*, where a and b are the minor and major axes of the ellipse, and polarization rotation, θ, of the transmitted light.* ***E*** *is the electric field vector.*

4.5 SUMMARY

This chapter introduced some modern fabrication and characterization techniques of optical components. In the next two chapters, presenting the main results of this thesis, these techniques are utilized.

5 Thin metal and metal oxide films

It was revealed in the previous chapter that the microstructure of thin films is affected by the deposition method and the process parameters. In this chapter we review how these factors contribute to the macroscopic optical properties. More precisely, we examine how the complex refractive index of a thin film is dependent on thickness and the deposition technique.

Furthermore, we examine more closely colorful stainless steel surfaces that the laser-marking technique creates below the ablation threshold. We show that the colors are produced by thin film interference in chromium oxide films growing on the surface during the marking.

5.1 CHANGES IN REFRACTIVE INDEX IN METAL FILMS

Retrieving refractive indexes from the optical constants database, such as those represented by the references [21, 75], is not a task without concern. The refractive indexes tabulated in these databases are measured for several differently fabricated and processed materials. The materials may have been fabricated by evaporation, sputtering or arc-zone melting, and some of them are bulk. The process parameters, such as temperature and pressure for evaporated or sputtered samples, are certainly not equal. Furthermore, post-processing of the samples may or may not include, for example, polishing, annealing, and rinsing. [76–82]

In order to design optical devices, the refractive index used for the theoretical calculations should be known as precisely as possible. Especially the optical response of resonant elements, such as waveguide resonators and plasmon resonators, is very sensitive to

changes in the refractive index. Even modification in the second decimal can shift the resonance peak out of the operational range and alter the spectral intensity.

In case of thin films, in addition to the fabrication technique and process parameters, the thickness of the film also affects the refractive index in many different ways. We have demonstrated in **Paper I** how the complex refraction index changes between films of different thickness and different deposition techniques. The techniques that were used for the deposition of the films included atomic-layer deposition (ALD) and electron-beam gun evaporation. The deposited materials were aluminum and iridium. Iridium was deposited by both methods but aluminum was deposited only by evaporation since the ALD of aluminum is extremely challenging. The thickness of aluminum films ranged between 37–290 nm; for iridium it was between 30–144 nm.

The samples were cleaned as described in **Paper I** to remove contaminants that could affect the nucleation and further film growth. The process parameters, including evaporation rate, vacuum chamber pressure, and temperature, were kept constant for each material. The refractive indexes were determined by a variable angle spectroscopic ellipsometer, VASE, provided by J. A. Woollam Co. Refractive indexes were calculated using the initial estimate approach, described in section 4.4, and the combined Lorentz–Drude model given by Eq. (2.8) and Eq. (2.9). In the case of aluminum, we also added a 3-nm-thick oxide layer on top of the metal layer.

The aluminum oxide thickness used in the modeling has a significant impact on the refractive indexes we obtain for the aluminum film in the modeling. The 3 nm thickness is not necessarily the accurate value for the oxide layer. However, since the process parameters in evaporation were chosen to be such that they would minimize the surface roughness and the samples were measured at the same age, within one day, we could assume that the thickness of the oxide film was the same for all aluminum samples. As a result, the refractive indexes represented in Fig. 5.1 (a) and (b) might scale up or down but in similar manner for all samples, permitting the

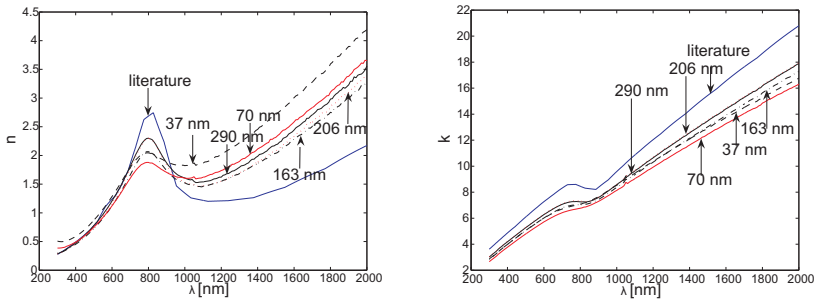

(a) (b)

Figure 5.1: Real part (a) and imaginary part (b) of the refractive index for 37 nm, 70 nm, 163 nm, 206 nm, and 290 nm thick electron-beam-gun-evaporated aluminum films. The literature values are for ultra-high-vacuum-evaporated film [21, 82].

thickness dependence to remain.

For iridium the analysis of thickness dependence is more straightforward since no native oxide layer is formed on it at room temperature. Figure 5.2 indicates that the real part of the refractive index approaches the literature values, taken for a crystal rod of iridium, when the thickness of the film increases. For ALD iridium the change is not as significant as for the evaporated films. This is not surprising if we consider the well-controlled microstructure that ALD produces. The same applies to the imaginary part of the refractive index, except for the fact that the imaginary part of evaporated films is closer to the literature values for thinner films, but not the thicker.

Figure 5.2 shows that the imaginary and real part of the ALD refractive index drops when the thickness increases. We have proposed in **Paper I** that this could be due to an increase in the amount of impurities and defects occurring in the ALD process when more monolayers are deposited. It is a well-known fact that these kind of defects make the refractive index more effective-like [84–86]. Moreover, when the impurities consist of air, both the real and imaginary part of the effective refractive index decreases compared to the value of the pure metal. For evaporated iridium the thickness

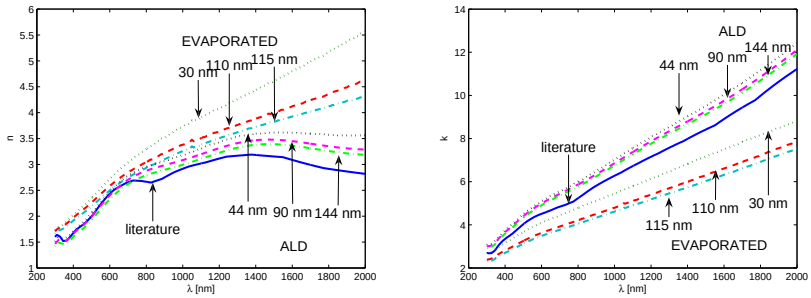

(a) (b)

Figure 5.2: Real part (a) and imaginary part (b) of the refractive index for 44 nm, 90 nm, and 144 nm thick atomic-layer deposited iridium compared to 30 nm, 110 nm, and 115 nm thick evaporated iridium. The literature values are for a polycrystalline iridium rod [21, 83].

effect is mostly dominated by cracks on the surface that increase in size for thicker films. The cracks were caused by the different thermal expansion coefficients of iridium and silicon dioxide, which was used as a substrate.

For evaporated aluminum the behavior of the imaginary part of the refractive index is opposite to that of ALD films. The imaginary part decreases for thinner films. Since the surface of the aluminum samples were smooth and homogenous, the cracks were not an issue. Instead, the decrease could be explained by grain structure evolution. As stated in Chapter 4, the size of the evaporated grain for aluminum tends to be the same as the thickness of the film. Consequently, for the thinnest aluminum layers the grain size could have a limiting effect on the electron mean free path, which is about 15 nm at room temperature [23, 87]. If the mean free path is reduced, the conductivity drops and, as does the imaginary part of the refractive index. In addition, the proportion of impurities, such as oxygen, might be smaller for thicker films. The oxygen content in the vacuum chamber is consumed by the oxidation of aluminum. Therefore, as the film gets thicker, the oxygen content gets smaller and smaller. The increased proportion of air and other impurities for thinner films would be consistent with the fact that

the interband transitions of aluminum at 800 nm are not as strong for thin films as they are for thicker ones. This is shown in Fig. 5.1 (b), where the curve is smoother at the interband transition region for the thinner films.

Some inconsistencies between the behavior of the complex refractive indexes also exist. For example, why does the film with a thickness of 70 nm have a smaller extinction coefficient than the 37 nm thick film? A factor that might contribute to this is the fluctuating evaporation rate that ranged between 1.8–2.2 Å/s for aluminum. The evaporation rate affects grain growth and therefore the optical properties as well. Another unexplained feature is the high real refractive index of evaporated iridium films. We might also assume that the real part would be smaller than that of the ALD film due to the more effective-like optical properties, but obviously this is not the case.

5.2 COLORS ON LASER-MARKED STAINLESS STEEL

Laser-marking is a relatively fast and cheap technique when a metallic surface needs to have legible and durable colored markings. The technique has been used industrially and to some extent in companies for marking and decorative purposes. We know that the physical origins of the color are in thin film interference and diffraction. Thin film interference is caused by the oxide layer growning on the metal surface during the laser marking and diffraction [88] may originate from the periodic structures that were created by scanning the surface line by line with the laser. The physical mechanism of the oxidation has been studied quite extensively [89–94], but the modeling of the optical effect has received only limited attention and only one profound study, made by Zheng *et al*. [95], may be found on the subject.

We have demonstrated in **Paper II** that colors seen by the naked eye are effective in the sense that the reflected intensity spectrum is a superposition of reflectances of chromium oxide films with several thicknesses. This differs from the model suggested by Zheng

et al., which states that the color is formed in horizontally homogenous thin film with a uniform thickness and the refractive index changing gradiently normal to the surface. We have chosen stainless steel grade AISI 304L as the metal due to its several commercial applications.

The samples that were studied are shown in Fig. 5.3 (a) and are indicated by the letters A, B, and C, representing blue, silver green and purple colored samples, respectively. We used a pulsed YLP-series ytterbium fiber laser with an average power of 18 W and a wavelength of 1064 nm. Different colors were obtained by changing the laser-marking parameters; this is more accurately described in **Paper II**.

A microscopic image of the purple sample is represented in Fig. 5.3 (b). It is evident that the surface actually consists of several different colors. It has been reported that different oxides occur at different temperatures [96]. In order to determine the thickness and the materials that produced the colors in the microscopic image the surface was imaged through a microscope with a spectral camera allowing a reflectance measurement for 500×500 nm^2 sized surface areas.

Stainless steel AISI 304L consists mainly of iron. In addition,

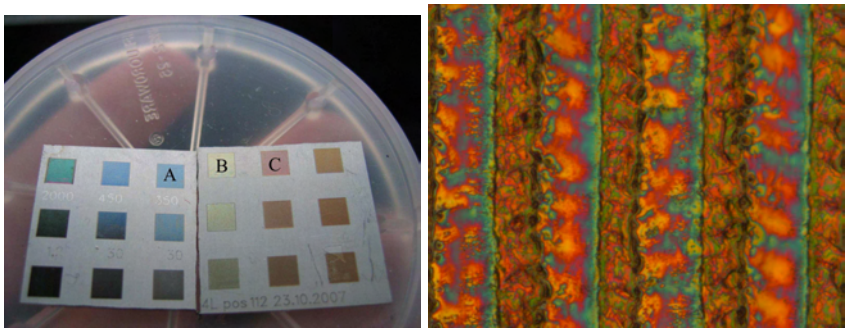

(a) (b)

Figure 5.3: Laser-marked stainless steel (a). The colors that were modeled are indicated by the letters A, B, and C corresponding to blue, silver green and purple, respectively. (b) represents the microscopic image of the purple sample.

it contains 20 % chromium, 9 % nickel and less than 2 % carbon, magnanese, silicon, phosphorous, sulphur, and molybdenum. Therefore each of the microscopic spectra, imaged with the spectral camera, was modeled as a thin layer of chromium, iron, or nickel oxide. We also tried to model the surface as a multilayered structure with several different oxides one on top of the other. However, we concluded that all the colors were produced by a single layer of chromium oxide with varying thicknesses. The overall effective spectrum was calculated by summing all the microscopic spectra. This sum spectrum was consistent with the experimental effective spectrum measured with the ellipsometer.

The calculated thickness of chromium oxide ranged between 0–500 nm. This result was supported by elementary analysis and scanning electron microscope (SEM) cross-section images, as presented in Fig. 5.4, where the SEM image of the 466.7 nm thick chromium oxide layer is shown. According to the elementary analysis, the amount of oxygen and chromium was lowest at that part of the surface where the modeling resulted in a thin oxide layer and vice versa. This is shown in Fig. 5.5 (a) and (b).

Using a similar modeling procedure, we obtained a quantitative

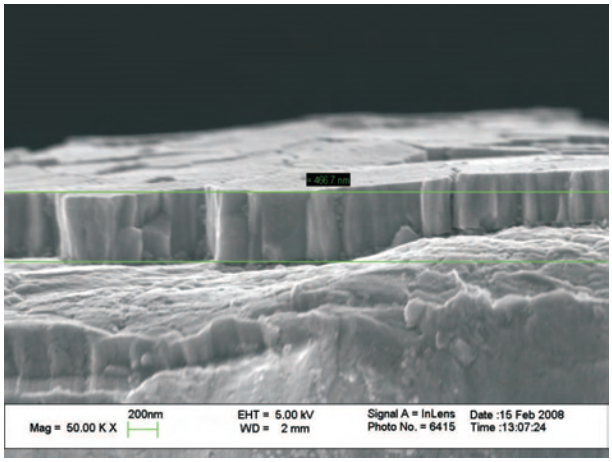

Figure 5.4: Cross-section image of laser-marked stainless steel. Chromium oxide layer is between the green lines.

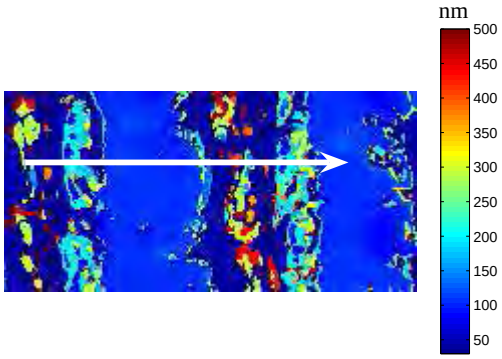

(a)

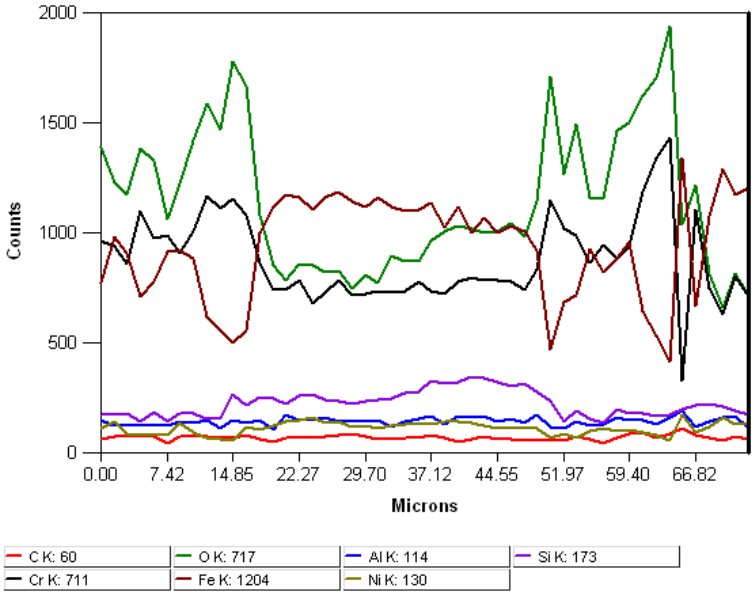

(b)

Figure 5.5: Chromium oxide thickness map (a) and elementary analysis result (b) measured along the arrow in (a). The green line represents oxygen counts, the red line iron, and the black line chromium.

connection between the laser beam energy on the surface, color, and oxide thickness, as represented in Fig. 5.6 (a)–(c). The energy values are calculated for 8 μm^2 sized areas where the surface was heated stationarily for 350 μs. The results show that colors are produced with energy values of 0.5–13 μJ. However, the thickest oxide layers do not correspond to the highest energy values. In fact, in the region of highest energy the oxide layer thickness is close to zero. We therefore conclude that in this region the ablation threshold has been exceeded, and stainless steel is more evaporated than oxidized.

In conclusion, we have suggested a model describing colors on a laser-marked stainless steel surface. This has provided a physi-

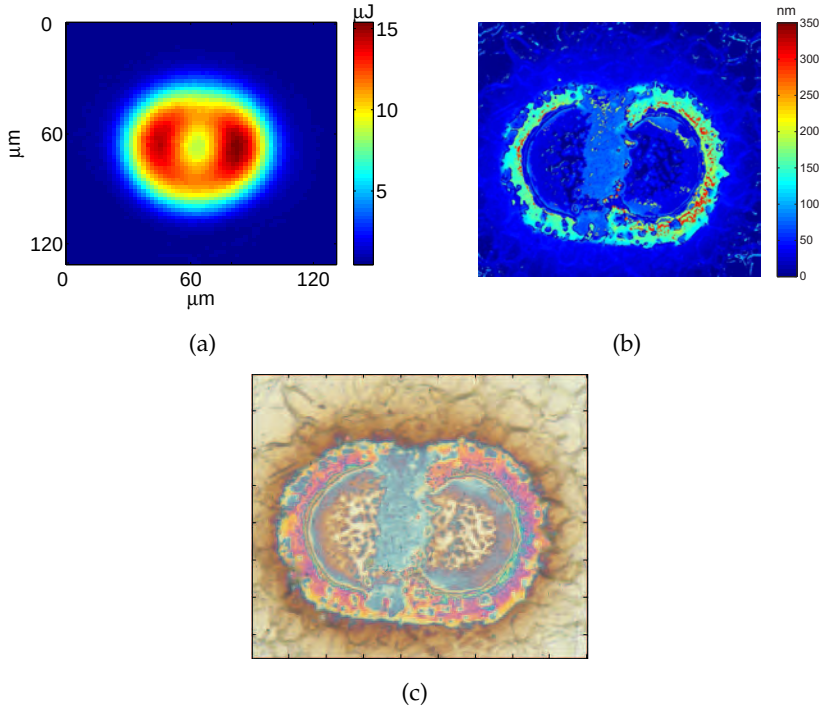

Figure 5.6: Laser beam energy distribution on the surface (a), chromium oxide thickness map (b), and microscopic image (c) of stainless steel surface that was heated with a pulsed ytterbium fiber laser without scanning.

cal understanding of the laser-marking technique, which hopefully will lead to better control of the colors that are formed during the marking. Thus far, the colors have been produced by random experimentation on adjusting the laser parameters. In the future, it would be appealing to be able to predict the correct process parameters for each color. This could be done most easily using a laser beam with a flat-top intensity profile. In this case, the energy on the surface would be equal across the beam and the cumulative heat effects would be easier to consider in the calculations. The flat-top profile would also provide a basis for applying the laser-marking technique to RGB color pixeling, idea of which is to produce the desired colors effectively as the sum of red, green, and blue spots.

5.3 SUMMARY

In this chapter we discussed the microscopic properties of metallic thin films. We showed how different fabrication methods and process parameters result in different microscopic structures that also change with thickness. The resulting differences in refractive index were consistent for some samples but for others the behavior of the refractive index could not be explained. Nevertheless, it became very clear that the refractive indexes of thin metallic films in general differ from the literature values and we recommend that they be measured each time the thickness or process is changed, to guarantee successful optical design.

Thin oxide films on laser-marked stainless steel were considered from the macroscopic perspective by examining the optical effects found on the colored surface. We demonstrated that the colors were formed in chromium oxide films by thin film interference and showed how the energy density, color, and oxide thickness were connected to each other. Knowledge of the relationship of energy and color will hopefully increase control over the laser-marking process and its possible application to RGB color pixeling.

6 Polarization shaping metallic gratings

Since the introduction of the term plasmon in 1956 [97] surface plasmon optics has undergone a gradual transition from fundamental studies to more application-emphasized research. In this chapter we show some ways that plasmonics together with guided-mode resonance may be utilized in designing polarization shaping devices. We introduce wire grid polarizers and a beamsplitter that differ from conventional designs by absorbing either a parallel or perpendicular field component. Furthermore, we thoroughly analyze polarization rotation in a chiral grating exhibiting giant optical activity simultaneously with enhanced transmission.

In the following results the incident electromagnetic field in the calculations is assumed to be a stationary plane wave. All the calculations have been made with the Fourier modal method.

6.1 EXTRAORDINARY WIRE GRID POLARIZERS

Wire grid polarizers are linear metallic gratings with a grating period much smaller than the wavelength of light [98–100]. A schematic of a linear polarizer was presented in Chapter 3 in Fig. 3.4 where n_1 and n_2 denote now the refractive indexes of metal and dielectric, respectively. In this thesis the dielectric is air and the substrate is fused silica, SiO_2.

Wire grid polarizers can be analyzed using the effective medium theory described in Chapter 3. Since the effective refractive index given by Eq. (3.45) is almost real when n_2 is real and the fill factor is less than 0.5, the polarizer exhibits properties similar to thin dielectric film, and the light polarized perpendicularly to the metallic grating lines is transmitted. For the parallel field, when n_2 is metal,

the imaginary part of the effective refractive index in Eq. (3.46) is more significant. Therefore, for perpendicular polarization the structure may be considered as a metallic thin film and the light is reflected above the plasma wavelength. The same conclusion is obtained by considering the structure from the electrons' point of view. Electrons are able to move as they would in a thin metal film only along the wire, and this movement is induced only by parallel polarization.

In the vicinity of the plasma and wave guide resonances the division into metallic and dielectric behavior changes. Suddenly, the field is transmitted or absorbed and is no longer reflected. We have called these polarizers extraordinary due to their optical properties, which differ from conventional wire grid polarizers.

6.1.1 Inverse polarizer

At the plasma frequency the effective refractive indexes in Eq. (3.45) and Eq. (3.46) may be approximated by expanding them into a Taylor series and taking the first-order term. The refractive index is then

$$n_{\parallel}^{\text{eff}} \approx \sqrt{1-f} \tag{6.1}$$

for the parallel component and

$$n_{\perp}^{\text{eff}} \approx \frac{\hat{n}_1}{\sqrt{f}} \tag{6.2}$$

for the perpendicular component. However, for real metals the damping term γ in Eq. (2.9) is never zero. Therefore, the bulk plasma resonance condition $\hat{\epsilon}_{\text{r}} = 0$, corresponding to Eq. (2.11), becomes $\epsilon' = 0$ and $\epsilon'' \ll 1$.

In **Paper III** we analyzed the optical properties of a silver wire grid grating in the vicinity of the bulk plasmon wavelength, which is 328 nm for silver. We showed that according to Eq. (6.1) the polarizer may be considered as a dielectric thin film for the parallel field. As a result, the parallel field is mostly transmitted. For perpendicular polarization, according to Eq. (6.2), the behavior is dictated by

the complex refractive index of silver and the field is mostly absorbed. The transmittance and absorbance for the perpendicular and parallel field are shown in Fig. 6.1.

We also explained the behavior from non-effective point of view. According to the constitutive relation Eq. (3.10), the field inside the metal is much stronger than the field in the air when $|\epsilon_{\mathrm{Ag}}| \ll |\epsilon_{\mathrm{air}}|$. Therefore, the field is localized into the metal and absorbed. According to the boundary condition given by Eq. (3.15) and due to the subwavelength structure, the parallel field must be continuous and nearly homogenous in the grating. Since the modulus of the complex refractive index of metal is small at the plasma wavelength, the transmission is solely defined by the proportion of air in the modulated area of the grating. Because the proportion of air is high, the parallel field is mostly transmitted.

There have been studies on the excitation of bulk plasmons and the abnormal absorption related to it [24, 101–103]. The excitation of bulk plasmons requires that the electric field has a component normal to the surface. The normal component can also be generated in gratings in normal incidence but in subwavelength gratings the magnitude of the component is negligible. Therefore, although the

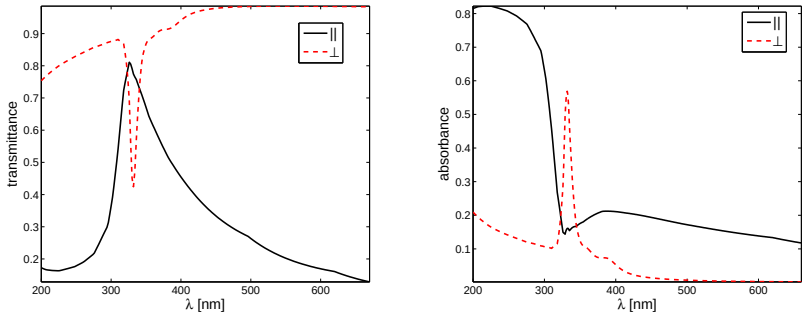

(a) (b)

Figure 6.1: Transmittance (a) and absorbance (b) of parallel (∥) and perpendicular (⊥) polarizations when the incidence angle is normal to the grating. The grating period is 30 nm, the depth is 100 nm, and the width of the metal stripe is 5 nm. The substrate is fused silica, SiO_2.

absorption in our case situates at bulk plasmon wavelength, it is unlikely that bulk plasmons are excited.

Absorbing polarizers could be used as polarizing filters. However, the spectral position of a bulk plasmon wavelength is a consequence of the material property and cannot be tailored by structure optimization. This may of course be seen as beneficial since the performance of the grating is not so sensitive to manufacturing defects. Nevertheless, for an application such as the polarizing filter, the absorption and contrast between the transmitted components, which was only 1.9106, must be higher. In order to obtain better performance the polarizer design must be based on another physical effects.

6.1.2 Highly absorbing polarizer

In **Paper IV** we designed and fabricated polarizing filters that reach an absorption of nearly 100 % together with a contrast of 6600. Two designs were made: design A absorbed the perpendicular polarization and transmitted the parallel. Design B absorbed the parallel polarization and transmitted the perpendicular. The grating structures representing both designs is shown in Fig. 6.2. The structures were optimized for 532 nm, which is the wavelength of the diode-pumped solid state (DPSS) laser and the frequency-doubled Nd:YAG laser. A 15 nm-thick aluminum oxide layer on the side walls and the top of the aluminum wires was taken into account in the optimization. Transmittance, reflectance and absorbance for the gratings are shown in Fig. 6.3 (a) and (b).

Bulk aluminum has an absorption of 8 % at the visible spectral range. We concluded by analyzing the field intensity and energy flow distributions given in Figs. 6.4 and 6.5 that the high absorption originates from the guided-mode resonance. When light is coupled to the wave guide mode, the interaction between the light and metal increases, which enhances the natural absorbance of aluminum. The arrows in Figs. 6.4 and 6.5 indicate the Poynting vectors calculated with Eq. (3.9).

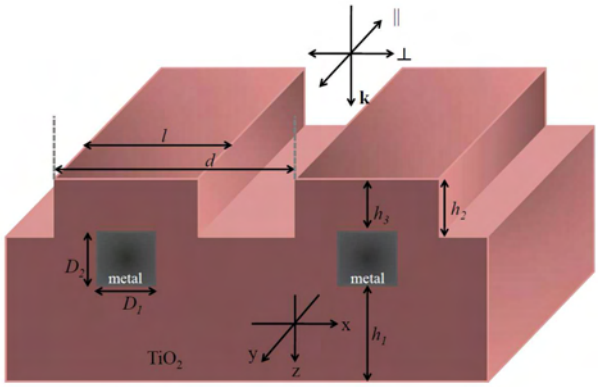

Figure 6.2: Grating geometry. The optimized parameters for design A are $d = 244$ *nm,* $D_1 = 125$ *nm,* $D_2 = 86$ *nm,* $h_1 = 84$ *nm,* $h_2 = D_2 = 86$ *nm,* $h_3 = 49$ *nm, and* $l = 223$ *nm. The parameters for design B are* $d = 312$ *nm,* $D_1 = 40$ *nm,* $D_2 = 140$ *nm,* $h_1 = 34$ *nm,* $h_2 = 64$ *nm,* $h_3 = 36$ *nm, and* $l = 102$ *nm. The metal is aluminum.*

Waveguide modes propagate along the x-axis. When they interfere with each other, a periodic pattern of high intensity regions, so-called hot spots, is expected to occur in the x-direction. The hot spots are indeed present in the titanium oxide layer between the

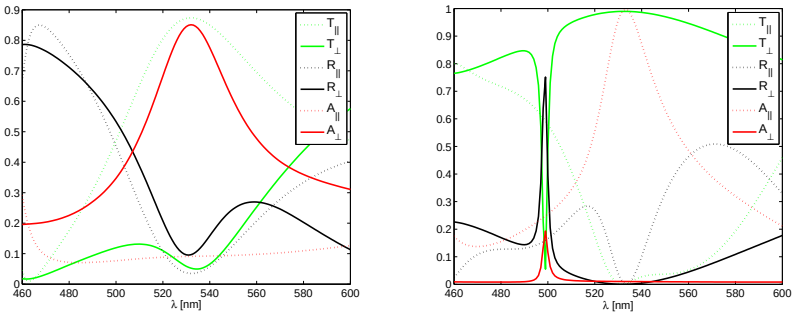

(a) (b)

Figure 6.3: Reflectance (black), transmittance (green), and absorbance (red) for the perpendicular (solid line) and parallel components (dashed line). Light is incident at the normal angle. (a) represents design A and (b) design B. For design B the contrast $T_\perp / T_\parallel = 6600$ *and the absorbance is 0.9967 % at 532 nm.*

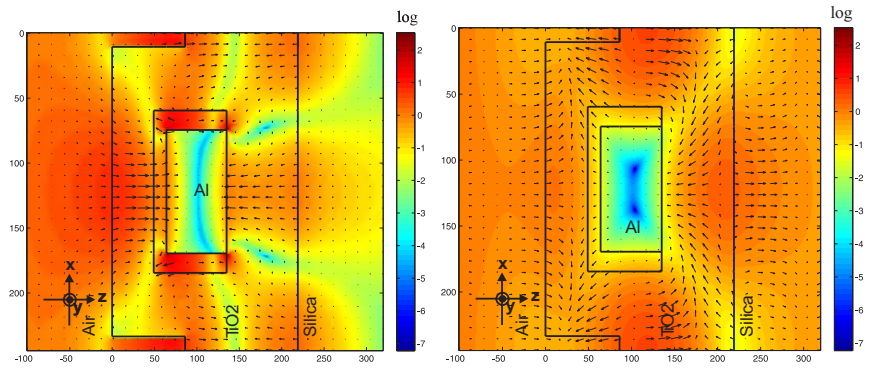

(a) (b)

Figure 6.4: Electric field intensity and Poynting vector distribution inside one grating period for design A. (a) and (b) represent the x (absorbed) and y (transmitted) components, respectively. Light is incident along the z-axis. In (a) the incident light is polarized perpendicular to the grating lines. In (b) the incident field is polarized parallel to the grating lines. The material on top of and on the sidewalls of aluminum is aluminum dioxide. The scale is logarithmic.

aluminum wires and the silicon dioxide substrate as can be seen in Fig. 6.4 (a) and Fig. 6.5 (b). In addition, if the grating parameters are optimized for an oblique angle of incidence, the Poynting vector arrows in Fig. 6.6 (a) show that the energy flows clearly along the waveguide between the aluminum and titanium dioxide, which is clear evidence of guided-mode resonance. This is not seen in the normal angle of incidence because the energy flows in both directions along x-axis due to the symmetry of the structure.

We fabricated the structure corresponding to design A to demonstrate the effect experimentally. Design A was chosen because it is easier to fabricate since it has a much more reasonable aspect ratio. The sample was fabricated by electron beam lithography and the titanium oxide layer was grown by atomic layer deposition. Figure 6.6 (b) indicates that the theoretical calculations match the experimental transmittance measured with an ellipsometer. The small differences are caused by the oxidation of aluminum and manufacturing defects such as rounding of the rectangular corners.

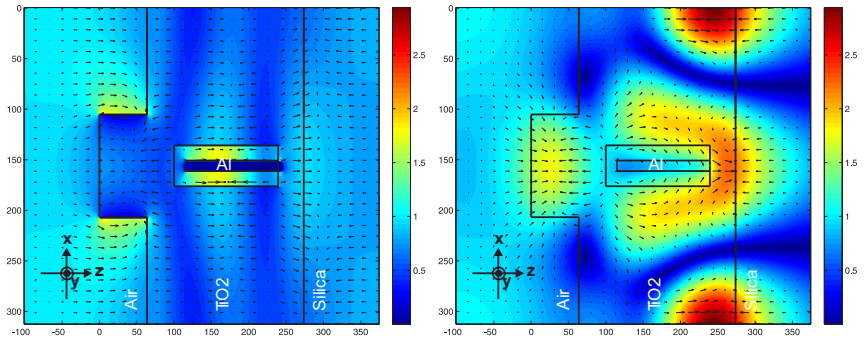

(a) (b)

Figure 6.5: Intensity and Poynting vector distribution of the electric field in the aluminum grating for design B. (a) and (b) represent the x (transmitted) and y (absorbed) components, respectively. In (a) the incident light is polarized perpendicular to the grating lines. In (b) the incident field is parallel to the grating lines.

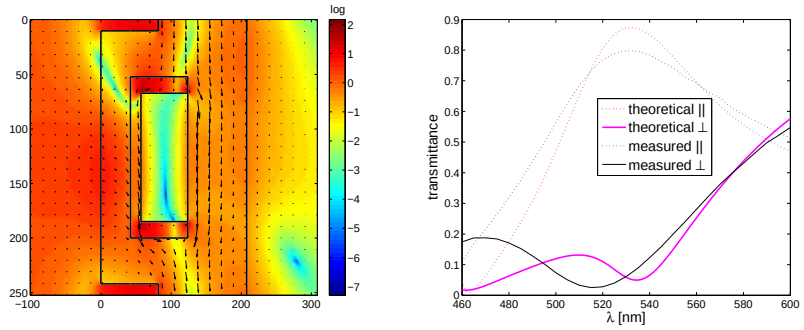

(a) (b)

Figure 6.6: In (a) the electric field intensity and direction of energy flow is given for design A in a 10 deg angle of incidence with slightly altered grating parameters. In (b) experimental (black line) and theoretical (purple line) transmittance for the perpendicular (solid line) and parallel (dashed line) components for design A are given.

6.2 HIGHLY ABSORBING BEAMSPLITTER

The same structure used for the polarizing filters in Fig. 6.2 may also be employed as a polarizing beamsplitter. We proposed a beamsplitter in **Paper IV** that absorbs the perpendicular field component and splits the parallel component into reflected and trans-

mitted fields. The design provides an alternative to traditional polarizing beamsplitters that split the incident beam into two beams of different linear polarizations. The parameters are $d = 419.3$ nm, $D_1 = D_2 = h_2 = 94$ nm, $h_1 = 188.7$ nm, $h_3 = 50.4$ nm, and $l = 194.8$ nm. The design was made for a HeNe-laser that emits the wavelength of 632.8 nm. The metal was gold. The reflectance, transmittance and absorbance are given in Fig. 6.7

Again, the absorbance is significantly higher than for bulk gold. We concluded that not only guided-mode resonance but localized surface plasmon resonance as well contributes to the enhancement of absorption.

The periodic hot spot pattern in Fig. 6.8 indicates the coupling of light in guided-mode resonance. Furthermore, the field is localized to the corners of the gold wires, where the energy flow forms vortexes. In addition, the field penetrates into the metal from the sidewalls of the wire. Such field distribution in metal wires is related to the excitation of localized surface plasmons [104]. The excitation of the plasmons would be consistent with the numerical

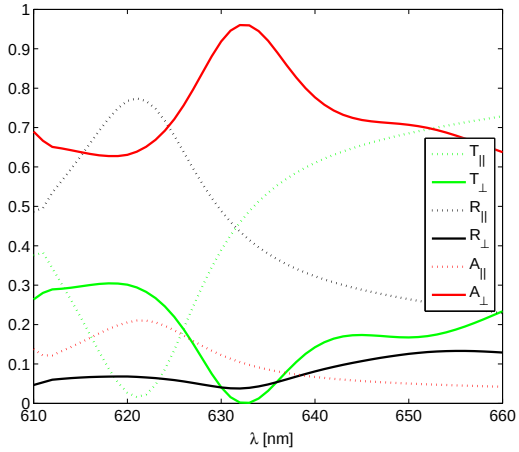

Figure 6.7: Reflectance (black), transmittance (green), and absorbance (red) for perpendicular (solid line) and parallel components (dashed line). Light is incident at the normal angle.

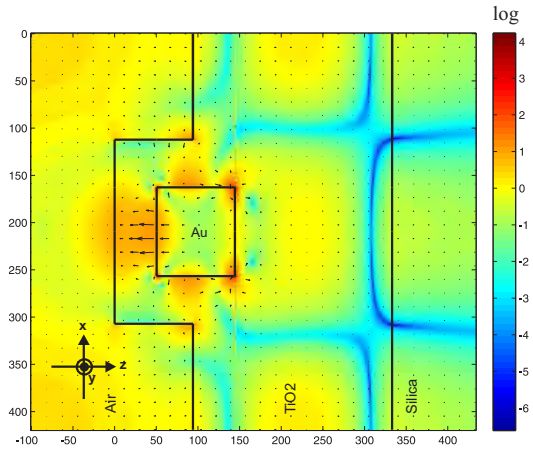

Figure 6.8: Electric field intensity and Poynting vector distribution of the absorbed x-component in a gold grating. The incident light is polarized perpendicular to the grating lines. The scale is logarithmic.

convergence shown in Fig. 6.9, which was found to be exceptionally poor. As stated in Chapter 3, there are some problems with the convergence of the Fourier modal method that could occur in plasma resonances due to the contribution of evanescent fields.

The localized surface plasma resonance condition for an infinitely long cylinder given by Eq. (2.25) shifts to longer wavelengths when fields of the ensemble of cylinders are coupled or when the particle size is increased [29, 105–107]. The resonance condition in Eq. (2.25) is fulfilled at 560 nm for a gold cylinder in titanium oxide. When taking the redshift into account, the particle plasma resonance could be excited at the wavelength of 632.8 nm, which supports our conclusions.

6.3 CHIRAL POLARIZATION ROTATOR

A material that causes an incident linearly polarized electric field to rotate is said to be optically active. In nature optical activity is found in materials that have chiral molecules or an asymmetric molecular arrangement. Optical activity is caused by circular

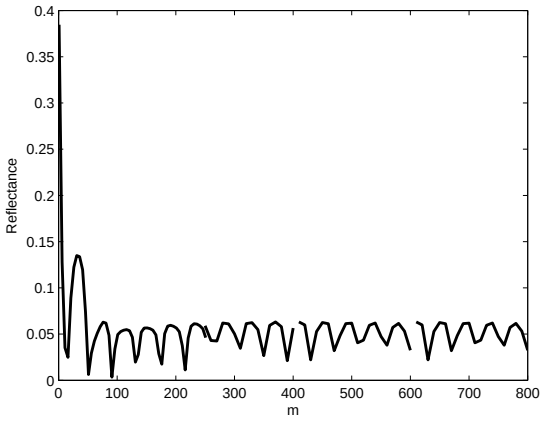

Figure 6.9: Convergence for the perpendicular component in reflectance. The number of the diffraction orders used in calculations is 2m+1.

birefringence, which means that the left- and right-handed circular polarizations have different refractive indexes. Since linear polarization may be expressed as the sum of left- and right-handed polarizations, the different phase changes that the two circular polarizations experience in an optically active material is manifested as a rotation of linearly polarized light. The greater the difference between the phase changes, the larger the polarization rotation. Furthermore, linear polarization becomes elliptical polarization when the absorbance of the material is different for the two circular polarizations. This phenomenon is called circular dichroism. Examples of naturally optically active materials are crystalline quartz and cinnabar, HgS, which have an optical rotatory power of 21.7 deg/mm and 32.5 deg/mm, respectively. [13]

Optical activity may also be produced artificially by nanostructured surfaces where chiral structural features correspond to the molecules of the optically active natural materials. This effect has been achieved by dielectric [108, 109] and metallic structures [110–114] where the polarization rotation is enhanced by resonant anomalies. In metals, the main enhancing resonance mechanism is surface plasmon resonance. The enhancement is based on the different re-

sponses of the two circular polarizations to the resonance anomaly. The drawback of the enhancement is that the resonances dissipate the electromagnetic energy, causing losses to the transmittance. On the other hand, surface plasmons have also been related to extraordinarily high transmission in perforated [115] and corrugated [116] metal films. Therefore, it is reasonable to consider the simultaneous realization of both enhanced optical activity and enhanced transmission in metallic chiral structures.

In **Paper V** we designed and fabricated a chiral golden hole structure with an optical rotatory power of 5×10^4 deg/mm and transmittance of 53.5 % at the wavelength of 1168 nm. The most intuitive chiral structure is perhaps a helix that resembles the chiral molecules of an optically active material. However, since a non-planar helix structure is difficult to fabricate with electron beam lithography, we chose another intuitive chiral structure, gammadion, which is presented in Fig. 6.10. The gammadion structure is also easy to model with the Fourier model method because only rectangular shapes are present.

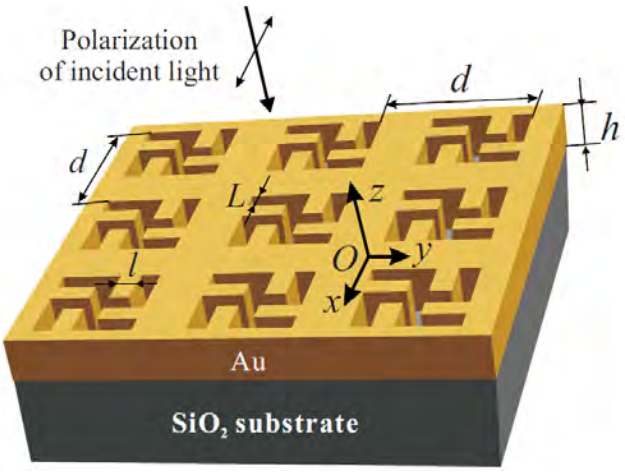

Figure 6.10: Gammadion grating structure. The grating period d=800 nm, depth h=80 nm, thickness of gammadion arm L=108 nm, and l=127 nm.

The structure was fabricated with electron beam lithography and the lift-off technique and was characterized experimentally by measuring the ellipsometric parameters ψ and δ and transmittance with a variable angle spectroscopic ellipsometer. The theoretical and measured polarization rotation, ellipticity, and transmittance are represented in Fig. 6.11. The polarization rotation θ was calculated with Eq. (4.6) and ellipticity from θ using Kramers–Kronig relations. Eq. (4.7) was not used due to its high sensitivity to values of δ that contain some noise.

The origin of the dips and peaks in Fig. 6.11, indicated by the letters A–J, were analyzed by investigating the dispersion relations for the Rayleigh anomaly and surface plasmons. For the Rayleigh anomaly the dispersion relation is given by Eq. (3.42). The dispersion relation for a surface plasmon on a periodic surface, also called surface plasmon Bloch modes, is obtained by matching Eq. (2.12) with Eq. (3.42). The contribution made by localized surface plasmons existing in the gammadion cavities was distinguished from

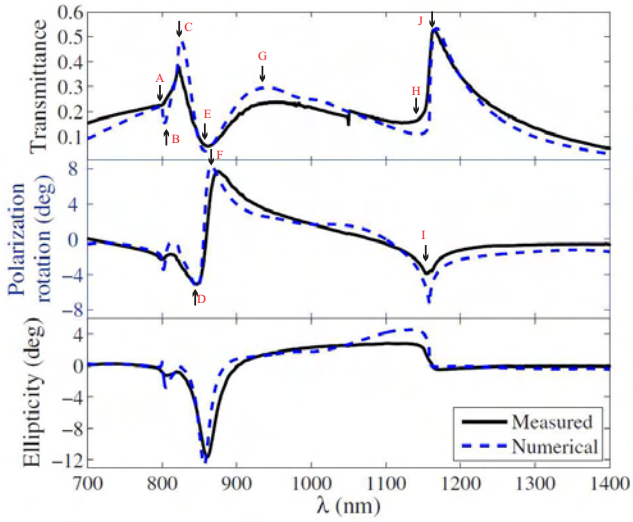

Figure 6.11: Theoretical (dashed blue) and experimental (solid black) transmittance, polarization rotation, and ellipticity.

that of the surface plasmons propagating on the metal by analyzing the field distributions of left- and right-handed circular polarizations.

We concluded that almost all anomalies arise from surface plasmons propagating along the metal, which is evidently the most important phenomenon for enhancing the polarization effect. Another important contributor is the Rayleigh anomaly, with a slightly moderate impact due to the spectrally narrow resonance. Localized surface plasmons, for one, provide a field coupling channel from the gold–air to gold–substrate interface. The anomalies corresponding to the spectral positions A–J are more precisely represented in **Paper V**.

6.4 SUMMARY

Localized surface plasmons are known to relate to energy absorption in metallic structures. We have shown that by embedding metal into the wave guide the absorption may be further increased by guided-mode resonance. It is crucial that the absorption is as high as possible from applications such as polarizing filters and and polarizing beamsplitters point of view. We have demonstrated that as high as 100 % absorption and a contrast of 6600 may be achieved solely by guided-mode resonance, which is remarkable considering the metal thickness in the structure is only 140 nm.

We have discovered that localized surface plasmons also contributed to the simultaneous enhancement of optical activity and transmittance in chiral gold gratings. The most important physical mechanism is the excitation of surface plasmon polaritons when the second place is occupied by the Rayleigh anomaly. The combination of the resonances and the Rayleigh anomaly has permitted us to optimize the structure so that the giant optical rotatory power of 5×10^4 deg/mm together with a transmittance of 53 % have been achieved.

7 Conclusions

This thesis has provided a survey of some optical phenomenon in metallic nano- and microstructures. We have studied metallic thin films, oxide films on metal, and metallic subwavelength gratings that shape the polarization through several physical effects.

First, we showed that the refractive index of metallic thin films depends on the thickness and fabrication method. We concluded that the main factors contributing to the refractive index were grain size, impurities, surface deformation, oxidation, and free path limitations. Overall, it became evident that instead of using literature values, it is most advisable to measure the refractive indexes for home-made thin film and use those values in designing optical elements. Especially for metals that react easily with oxygen, such as aluminum, the oxide inside and on the film has a significant effect on the refractive indexes. It is probable that metallic nano- and microstructures are even more prone to surface deformations and oxidation due to several air–metal interfaces, and the refractive indexes are drifted further away from the literature values representing thin films or bulk materials.

While the oxide layer formation on top of thin films is often undesirable in optical elements, it is the most important phenomenon in the laser coloring of metal surfaces. We discovered that when stainless steel surfaces were heated with a laser, a chemical reaction between air and chromium was triggered, which resulted in the growth of chromium oxide films on the stainless steel. The colors were formed by thin film interference so that different oxide thicknesses corresponded to different colors. We suggested that the laser-marking technique could be easily applied to RGB color pixeling if the beam intensity profile was modified to a flat-top shape. However, the semi-gaussian intensity profile allowed us to determine the relationships between energy density, color, and chromium oxide film thickness, which hopefully will improve con-

trol over the laser-marking technique.

The last chapter of this thesis concerning results was devoted to investigating the optical phenomena that led to the filtering or rotation of polarization in metallic gratings. We represented four linear gratings with exceptionally high absorption due to the characteristic material properties at the bulk plasmon wavelength, the guided-mode resonance, and/or the particle plasma resonance. The combined resonances of the wave guide and plasmons are interesting phenomena by themselves, but the results also seemed promising for applications. We managed to design a polarizing filter that absorbed nearly 100 % of the parallel component while the perpendicular component was nearly 100 % transmitted with a contrast of 6600. In addition, a polarizing beamsplitter absorbing the perpendicular component and splitting the parallel component into reflected and transmitted beams was introduced. It is noteworthy that the energy was dissipated into metallic structures only 40 nm thick and 140 nm high. Furthermore, we should recognize the limitations that absorption sets on the power of the laser. The use of the designed filters for high-energy lasers is advisable only if we want to evaporate the filter into air.

Instead of seeking the highest absorption, we tried to minimize the absorbtion and other losses in the transmission spectra of chiral polarization rotator. The goal was to optimize a structure with giant optical activity together with enhanced transmission, and analyze the physical effects behind the rotation and transmission spectral peaks. We concluded that the surface plasmons propagating on the metal surface made the most significant contribution to the peaks and dips in the spectra. The Rayleigh anomaly and localized surface plasmons also had an impact.

Overall, metallic nano- and microstructures possess great potential for several significant applications. One interesting possibility for metallic nanostructures lies in metamaterials that are artificial materials with optical properties different from anything in nature or capable of producing optical effects much stronger than natural materials. In the future, instead of today's fabrication techniques for

photonic structures, chemical methods, such as self-organization of molecules, might be used as the first-choice fabrication method to produce truly nano-sized structures leading to the creation of next-generation materials.

Bibliography

[1] I. Newton, *Opticks: or a Treatise of the Reflexion, Refractions, Inflexions and Colours* (Royal Society, London, 1704).

[2] T. Young, "Experimental demonstration of the general law of the interference of light," *Philos. T. Roy. Soc.* **94,** 1–16 (1804).

[3] G. Breit, "Quantum theory of dispersion," *Rev. Mod. Phys.* **4,** 504–576 (1932).

[4] H. A. Lorentz, *The Theory of Electrons and Its Applications to the Phenomena of Light and Radiant Heat* (B. G. Teubner, Leipzig, 1916).

[5] J. Homola, S. S. Yee, and G. Gauglitz, "Surface plasmon resonance sensors: review," *Sensor. Actuat. B* **54,** 3–15 (1999).

[6] J. Homola, "Surface plasmon resonance (SPR) biosensors and their applications to food safety and security," in *Frontiers in Planar Lightwave Circuit Technology,*, S. Janz, J. Ctyroky, and S. Tanev, eds. (Springer Netherlands, 2006), pp. 101-118.

[7] M. Quinten, A. Leitner, J. R. Krenn, and F. R. Aussenegg, "Electromagnetic energy transport via linear chains of silver nanoparticles," *Opt. Lett.* **23,** 1331–1333 (1998).

[8] S. A. Maier, M. L. Brongersma, P. G. Kik, S. Meltzer, A. A. G. Requicha, B. E. Koel, and H. A. Atwater, "Plasmonics –a route to nanoscale optical devices," *Adv. Mater.* **13,** 1501–1505 (2001).

[9] S. J. Oldenburg, C. C. Genick, K. A. Clark, and D. A. Schultz, "Base pair mismatch recognition using plasmon resonant particle labels," *Anal. Biochem.* **309,** 109–116 (2002).

[10] J. M. Köhler, A. Csáki, J. Reichert, R. Möller, W. Straube, and W. Fritzsche, "Selective labeling of oligonucleotide monolayers by metallic nanobeads for fast optical readout of DNA-chips," *Sensor. Actuat. B* **76,** 166–172 (2001).

[11] S. Schultz, D. R. Smith, J. J. Mock, and D. A. Schultz, "Single-target molecule detection with nonbleaching multicolor optical immunolabels," *Proc. Natl. Acad. Sci. USA* **97,** 996–1001 (2000).

[12] G. Bohren and D. Huffman, *Absorbtion and Scattering of Light by Small Particles* (John Wiley & Sons, Inc., New York, 1998).

[13] E. Hecht, *Optics* (Addison–Wesley, San Fransisco, 2002).

[14] H. A. Kramers, "La deffusion de la lumiere par les atomes," *Atti del Congresso Internazionale dei Fisici* **2,** 545–557 (1927).

[15] R. de L. Kronig, "On the theory of dispersion of X-rays," *J. Opt. Soc. Am.* **12,** 547–557 (1926).

[16] L. Landau and E. Lifshitz, *Electrodynamics of Continuous Media* (Pergamon Press, Oxford, 1975).

[17] M. Dressela and G. Grüner, *Electrodynamic of Solids: Optical Properties of Electrons in Matter* (Cambridge University Press, Cambridge, 2003).

[18] M. Fox, *Optical Properties of Solids* (Oxford University Press, Oxford, 2001).

[19] F. Wooten, *Optical Properties of Solids* (Academic Press, New York, 1972).

[20] P. Drude, *The Theory of Optics* (Dover Publications, New York, 1959).

[21] D. R. Lide, ed., *Handbook of Chemistry and Physics* (CRC Press LLC, Boca Raton, 2005).

[22] A. Hohenau, A. Leitner, and F. R. Aussenegg, "Near-field and far-field properties of nanoparticle arrays," in *Surface Plasmon Nanophotonics*, M. L. Brongersma and P. G. Kik, eds. (Springer, 2007).

[23] N. Ashcroft and N. Mermin, *Solid State Physics* (Holt-Saunders, New York, 1976).

[24] I. Lindau and P. O. Nilsson, "Experimental verification of optically excited longitudinal plasmons," *Phys. Scripta* **3,** 87–92 (1971).

[25] S. A. Maier, *Plasmonic Fundamentals and Applications* (Springer science + Business Media LLC, New York, 2007).

[26] R. B. M. Schasfoort and A. J. Tudos, *Handbook of Surface Plasmon Resonance* (The Royal Society of Chemistry, Cambridge, 2008).

[27] E. Kretschmann and H. Reather, "Radiative decay of nonradiative surface plasmons excited by light," *Z. Naturforsch., Tail A* **23,** 2135–2136 (1968).

[28] G. Mie, "Beiträge zur optik trüber medien, speziell kolloidaler metallösungen," *Ann. Phys.* **25,** 377–455 (1908).

[29] K. L. Kelly, E. Coronado, L. L. Zhao, and G. C. Schatz, "The optical properties of metal nanoparticles: the influence of size, shape, and idelectric environment," *J. Phys. Chem. B* **107,** 668–677 (2003).

[30] L. Novotny and B. Hecht, *Principles of Nano-Optics* (Cambridge University Press, Cambridge, 2006).

[31] M. Born and E. Wolf, *Principles of Optics* (Pergamon Press, Oxford, 1986).

[32] J. Maxwell, *A Treatise on Electricity and Magnetism*, Vol. 1, 3rd ed. (Dover, New York, 1954).

[33] J. Maxwell, *A Treatise on Electricity and Magnetism*, Vol. 2, 3rd ed. (Dover, New York, 1954).

[34] J. Marion and M. Heald, *Classical Electromagnetic Radiation*, 2nd ed. (Academic Press, New York, 1980).

[35] J. Goodman, *Introduction to Fourier Optics* (The McGraw-Hill Companies, Inc., New York, 1996).

[36] A. Devaney and G. Sherman, "Plane-wave representations for scalar wave fields," *SIAM rev.* **15,** 765–787 (1973).

[37] R. Petit, ed., *Electromagnetic Theory of Gratings* (Springer-Verlag, Berlin, 1980).

[38] O. M. L. Rayleigh, "On the dynamic theory of gratings," *Proc. Royal Soc.* **79,** 399–416 (1907).

[39] D. Maystre, "A new general integral theory for dielectric coated gratings," *J. Opt. Soc. Am.* **68,** 490–495 (1978).

[40] D. M. Sullivan, *Electromagnetic Simulation Using FDTD Method* (IEEE Press series, New York, 2000).

[41] G. C. J. Chandezon, M.T. Dupuis and D. Maystre, "Multi-coated gratings: A differential formalism applicable in the entire optical region," *J. Opt. Soc. Am.* **72,** 839–846 (1982).

[42] L. Li, "New formulation of the Fourier modal method for crossed surface-relief gratings," *J. Opt. Soc. Am. A* **14,** 2758–2767 (1997).

[43] L. Li, "Use of Fourier series in the analysis of discontinuous periodic structures," *J. Opt. Soc. Am. A* **13,** 1870–1876 (1996).

[44] M. Moharam, D. Pommet, E. Grann, and T. Gaylord, "Stable implementation of the rigorous coupled-wave analysis for surface-relief gratings: enhanced transmittance matrix approach," *J. Opt. Soc. Am. A* **12,** 1077–1086 (1995).

[45] J. Turunen, "Diffraction theory of microrelief gratings," in *Micro-Optics: Elements, Systems, and Applications*, H. P. Herzig, ed. (Taylor & Francis, 1997).

[46] L. Li, "Formulation and comparison of two recursive matrix algorithms for modeling layered diffraction gratings," *J. Opt. Soc. Am. A* **13,** 1024–1035 (1996).

[47] L. Li, "Note on the S-matrix propagation algorithm," *J. Opt. Soc. Am. A* **20,** 655–660 (2003).

[48] S. S. Wang and R. Magnusson, "Theory and applications of guided-mode resonance filters," *Appl. Opt.* **32,** 2606–2613 (1993).

[49] M. Kuittinen, J. Turunen, and P. Vahimaa, "Subwavelength-structured elements," in *Diffractive Optics for Industrial and Commerical Applications*, J. Turunen and F. Wyrowski, eds. (Wiley-VCH, 1997).

[50] P. Lalanne and D. Lemercier-Lalanne, "On the effective medium theory of subwavelength periodic structures," *J. Mod. Opt.* **43,** 2063–2085 (1996).

[51] R. Bräuer and O. Bryngdahl, "Design of antireflection gratings with approximate and rigorous methods," *Appl. Opt.* **33,** 7875–7882 (1994).

[52] C. Evans, *Precision Engineering: An Evolutionary View* (Cranfield University Press, Cranfield, 1989).

[53] S. Choi, M. Yan, L. Wanga, and I. Adesida, "Ultra-dense hydrogen silsesquioxane (HSQ) structures on thin silicon nitride membranes," *Microelectron. Eng.* **86,** 521–523 (2009).

[54] A. E. Grigorescu, M. C. van der Krogt, C. W. Hagen, and P. Kruit, "10 nm lines and spaces written in HSQ, using electron beam lithography," *Microelectron. Eng.* **84,** 822–824 (2007).

[55] J. Zheng, P. E. Constantinou, C. Micheel, A. P. Alivisatos, R. A. Kiehl, and N. C. Seeman, "Two-Dimensional Nanoparticle Arrays Show the Organizational Power of Robust DNA Motifs," *Nano Lett.* **6,** 1502–1504 (2006).

[56] T. Aaltonen, *Atomic Layer Deposition of Noble Metal Thin Films*, PhD thesis (University of Helsinki, Helsinki, 2005).

[57] D. M. Mattox, *Handbook of Physical Vapor Deposition (PVD) Processing* (Noyes Publications, Westwood, 1998).

[58] R. P. Netterfeld, "Review of thin film deposition techniques," *Optical Interference Coatings*, Proc. OSA, MA2–3 (2001).

[59] N. Kaiser, "Review of fundamentals of thin film growth," *Optical Interference Coatings*, Proc. OSA, MA1–3 (2001).

[60] M. Leskelä and M. Ritala, "Atomic layer deposition (ALD): from precursors to thin film structures," *Thin Solid Films* **409,** 138–146 (2002).

[61] T. Alasaarela, T. Saastamoinen, J. Hiltunen, A. Säynätjoki, A. Tervonen, P. Stenberg, M. Kuittinen, and S. Honkanen, "Atomic layer deposited titanium dioxide and its application in resonant waveguide grating," *Appl. Opt.* **49,** 4321–4325 (2010).

[62] M. Ritala and M. Leskelä, "Atomic layer deposition," in *Handbook of Thin Film Materials*, H. S. Nalwa, ed. (Academic Press, 2002), pp. 103–159.

[63] M. Ohring, *Materials Science of Thin Films: Deposition & Structure* (Academic Press, San Diego, 2002).

[64] R. H. Doremus, "Optical properties of thin metallic films in island form," *J. Appl. Phys.* **37,** 2775–2781 (1966).

[65] C. V. Thompson, "Structure evolution during processing of polycrystalline films," *Annu Rev. Mater. Sci.* **30,** 150–190 (2000).

[66] C. R. M. Grovenor, H. T. G. Hentzell, and D. A. Smith, "The development of grain structure during growth of metallic films," *Acta Metall.* **32,** 773–781 (1984).

[67] L. B. Freund and S. Suresh, *Thin Film Materials: Stress, Defect Formation and Surface Evolution* (Cambridge University Press, Cambridge, 2003).

[68] F. B. Bramwell, R. E. Zadjura, L. Stemp, S. R. Fahrenholtz, and J. M. Flowers, "Polymer photophysics: A negative photoresist," *J. Chem. Educ.* **56,** 541–542 (1797).

[69] J. Laukkanen, *Fabrication of metallic micro- and nanostructures for optical solutions*, PhD thesis (University of Eastern Finland, Joensuu, 2010).

[70] B. Päivänranta, *Nanostructured surfaces for photonic and biophotonic applications*, PhD thesis (University of Joensuu, Joensuu, 2009).

[71] K. R. Lawless, "The oxidation of metals," *Rep. Prog. Phys.* **37,** 231–316 (1974).

[72] *Guide to Using WVASE32* (J.A Woollam Co., Lincoln, 2003).

[73] W. Press, B. Flannery, S. Teukolsky, and W. Vetterling, *Numerical Recipes in C, The Art of Scientific Computing* (Cambridge University Press, Cambridge, 1988).

[74] E. Collet, *Polarized Light: Fundamentals and Applications* (Marker Dekker, Cambridge, 1993).

[75] E. Palik, ed., *Handbook of Optical Constants of Solids I* (Academic Press, San Diego, 1985).

[76] G. Hass and J. E. Waylonis, "Optical constants and reflectance and transmittance of evaporated aluminium in the visible and ultraviolet," *J. Opt. Soc. Am.* **51,** 719–722 (1961).

[77] L. W. Bos and D. W. Lynch, "Optical properties of antiferromagnetic chromium and dilute Cr-Mn and Cr-Re alloys," *Phys. Rev. B* **2,** 4567–4577 (1970).

[78] R. F. Fane and W. E. J. Neal, "Optical constants of aluminum films related to the vacuum environment," *J. Opt. Soc. Am.* **60,** 790–793 (1970).

[79] H.-J. Hagemann, W. Gudat, and C. Kunz, "Optical constants from the far infrared to the X-ray region: Mg, Al, Cu, Ag, Au, Bi, C, and Al_2O_3," *J. Opt. Soc. Am.* **65,** 742–744 (1975).

[80] H. Ehrenreich and H. R. Philipp, "Optical properties of Ag and Cu," *Phys. Rev.* **128,** 1622–1629 (1962).

[81] L. G. Schulz and F. R. Tangherlini, "Optical constants of silver, gold, copper and aluminum," *J. Opt. Soc. Am.* **44,** 362–368 (1954).

[82] E. Shiles, T. Sasaki, M. Inokuti, and D. Y. Smith, "Self-consistency and sum-rule tests in the Kramers-Kronig analysis of optical data: applications to aluminum," *Phys. Rev. B* **22,** 1612–1628 (1980).

[83] J. H. Weaver, C. G. Olson, and D. W. Lynch, "Optical investigation of the electronic structure of bulk Rh and Ir," *Phys. Rev. B* **15,** 4115–4118 (1977).

[84] D. E. Aspnes, "Optical properties of thin films," *Thin Solid Films* **89,** 249–262 (1982).

[85] O. Hunderi, "Influence of grain boundaries and lattice defects on the optical properties of some metals," *Phys. Rev. B* **7,** 3419–3429 (1973).

[86] L. Ward, "The effective optical constants of thin metal films in island form," *Brith. J. Appl. Phys. (J. Phys. D)* **2,** 123–125 (1969).

[87] W. Zhang, S. H. Brongersma, O. Richard, B. Brijs, R. Palmans, L. Froyen, and K. Maex, "Influence of the electron mean free

path on the resistivity of thin metal films," *Microelectron. Eng.* **76,** 146–152 (2004).

[88] A. Y. Vorobyev and C. Guoa, "Colorizing metals with femtosecond laser pulses," *Appl. Phys. Lett.* **92,** 041914 (2008).

[89] L. Nánai, R. Vajtai, and T. F. George, "Laser-induced oxidation of metals: state of the art," *Thin Solid Films* **298,** 160–164 (1997).

[90] M. Wautelet, "Laser-assisted reaction of metals with oxygen," *Appl. Phys. A* **50,** 131–139 (1990).

[91] A. M. Carey, W. M. Steen, and D. Watkins, "Laser-surface ornamentation," *Proceedings of International Congress on Application of Lasers & Electro-optics*, Proc. ICALEO, 170–178 (1998).

[92] A. M. Huntz, A. Reckmanna, C. Haut, C. Sévérac, M. Herbst, F. Resende, and A. Sabioni, "Oxidation of AISI 304 and AISI 439 stainless steels," *Mat. Sci. Eng. A* **447,** 266–276 (2007).

[93] S. Beauvais-Réveillon, A. M. Huntz, G. Moulin, and J. J. Bléchet, "Comparison of classical oxidation and laser oxidation of a chromium PVD coating on a pure-iron substrate," *Oxid. Met.* **43,** 279–300 (1995).

[94] S. Shibagaki, A. Koga, Y. Shirakawa, H. Onishi, H. Yokokawa, and J. Tanaka, "Chemical reaction path for thin film oxidation of stainless steel," *Thin Solid Films* **303,** 101–106 (1997).

[95] H. Y. Zheng, G. C. Lim, X. Wang, and J. Tan, "Process study for laser-induced surface coloration," *J. Laser Appl.* **14,** 215–220 (2002).

[96] A. Vesel, M. Mozetič, and A. Zalar, "Oxidation of AISI 304L stainless steel surface with atomic oxygen," *Appl. Surf. Sci.* **200,** 94–103 (2002).

[97] D. Pines, "Collective energy losses in solids," *Rev. Mod. Phys.* **28,** 184–199 (1956).

[98] G. R. Bird and M. P. Jr., "The Wire Grid as a Near-Infrared Polarizer," *J. Opt. Soc. Am.* **50,** 886–891 (1960).

[99] J. B. Yound, H. A. Graham, and E. W. Peterson, "Wire grid infrared polarizer," *Appl. Opt.* **4,** 1023–1026 (1965).

[100] C. Pentico, E. Gardner, D. Hansen, and R. Perkins, "New, high performance, durable polarizers for projection displays," *SID Int. Symp. Digest Tech. Papers*, Proc. SID, 1287–1289 (2001).

[101] L. Marton, J. A. Simpson, H. A. Fowler, and N. Swanson, "Plural scattering of 20-keV electrons in aluminum," *Phys. Rev.* **126,** 182–192 (1962).

[102] P. O. Nilsson, I. Lindau, and S. B. M. Hagström, "Optical plasma-resonance abrosption in thin films of silver and some silver alloys," *Phys. Rev. B* **1,** 498–505 (1970).

[103] B. P. Feuerbacher, R. P. Godwin, and M. Skibowski, "Plasma resonance in the photoelectric yield of thin aluminum films," *Z. Physik* **224,** 172–178 (1969).

[104] J. P. Kottmann, O. J. F. Martin, D. R. Smith, and S. Schultz, "Plasmon resonances of silver nanowires with a nonregular cross section," *Phys. Rev. B* **64,** 235402 (2001).

[105] L. A. Sweatlock, S. A. Maier, H. A. Atwater, J. J. Penninkhof, and A. Polman, "Highly confined electromagnetic fields in arrays of strongly coupled Ag nanoparticles," *Phys. Rev. B* **71,** 235408 (2005).

[106] J. P. Kottmann and O. J. F. Martin, "Plasmon resonant coupling in metallic nanowires," *Opt. Express* **8,** 655–663 (2001).

[107] G. Schider, J. R. Krenn, W. Gotschy, B. Lamprecht, H. Ditlbacher, A. Leitner, and F. R. Aussenegg, "Optical properties of Ag and Au nanowire gratings," *J. Appl. Phys.* **90,** 3825–3830 (2001).

[108] X. Meng, B. Bai, P. Karvinen, K. Konishi, J. Turunen, Y. Svirko, and M. Kuwata-Gonokami, "Experimental realization of all-dielectric planar chiral metamaterials with large optical activity in direct transmission," *Thin Solid Films* **516,** 8745–8748 (2008).

[109] B. Bai, K. Konishi, X. Meng, P. Karvinen, A. Lehmuskero, M. Kuwata-Gonokami, Y. Svirko, and J. Turunen, "Mechanism of the large polarization rotation effect in the all-dielectric artificially chiral nanogratings," *Opt. Express* **17,** 688–696 (2009).

[110] A. Papakostas, A. Potts, D. M. Bagnall, S. L. Prosvirnin, H. J. Coles, and N. I. Zheludev, "Optical manifestations of planar chirality," *Phys. Rev. Lett.* **90,** 107404 (2003).

[111] M. Decker, M. W. Klein, M. Wegener, and S. Linden, "Circular dichroism of planar chiral magnetic metamaterials," *Opt. Lett.* **32,** 856–858 (2007).

[112] V. A. Fedotov, A. S. Schwanecke, N. I. Zheludev, V. V. Khardikov, and S. L. Prosvirnin, "Asymmetric transmission of light and enantiomerically sensitive plasmon resonance in planar chiral nanostructures," *Nano Lett.* **7,** 1996–1999 (2007).

[113] M. Kuwata-Gonokami, N. Saito, Y. Ino, M. Kauranen, K. Jefimovs, T. Vallius, J. Turunen, and Y. Svirko, "Giant optical activity in quasi-two-dimensional planar nanostructures," *Phys. Rev. Lett.* **95,** 227401 (2005).

[114] K. Konishi, T. Sugimoto, B. Bai, Y. Svirko, and M. Kuwata-Gonokami, "Effect of surface plasmon resonance on the optical activity of chiral metal nanogratings," *Opt. Express* **15,** 9575–9583 (2007).

[115] T. W. Ebbesen, H. J. Lezec, H. F. Ghaemi, T. Thio, and P. A. Wolff, "Extraordinary optical transmission through sub-wavelength hole arrays," *Nature* **391,** 667–669 (1998).

[116] S. Wedge, I. R. Hooper, I. Sage, and W. L. Barnes, "Light emission through a corrugated metal film: The role of cross-coupled surfaceplasmon polaritons," *Phys. Rev. B* **69,** 245418 (2004).

Paper I

A. Lehmuskero, M. Kuittinen, and P. Vahimaa
"Refractive index and extinction coefficient dependence of thin Al and Ir films on deposition technique and thickness"
Optics Express,
15, pp. 10744–10752, 2007.

I A. Lehmuskero, M. Kuittinen, and P. Vahimaa, “Refractive index and extinction coefficient dependence of thin Al and Ir films on deposition technique and thickness,” *Opt. Express* 15, 10744–10752 (2007).

Refractive index and extinction coefficient dependence of thin Al and Ir films on deposition technique and thickness

Anni Lehmuskero, Markku Kuittinen, and Pasi Vahimaa

University of Joensuu, Department of Physics and Mathematics, P.O. Box 111, FI-80101 Joensuu, Finland

anni.lehmuskero@joensuu.fi

Abstract: We show that the optical properties of thin metallic films depend on the thickness of the film as well as on the deposition technique. Several thicknesses of electron-beam-gun-evaporated aluminium films were measured and the refractive index and the extinction coefficient defined using ellipsometry. In addition, the refractive indexes and the extinction coefficients of atomic-layer-deposited iridium were compared with those of evaporated iridium samples.

OCIS codes: (310.6860) Thin films, optical properties; (310.1860) Deposition and fabrication.

References and links

1. M. Kuwata-Gonokami, N. Saito, Y. Ino, M. Kauranen, K. Jefimovs, T. Vallius, J. Turunen, and Y. Svirko, "Giant optical activity in quasi-two-dimensional planar nanostructures," Phys. Rev. Lett. **95,** 227401 (2005).
2. K. Jefimovs, T. Vallius, V. Kettunen, M. Kuittinen, J. Turunen, P. Vahimaa, M. Kaipiainen, and S. Nenonen, "Inductive grid filters for rejection of infrared radiation," J. Mod. Opt. **51,** (2004) 1651–1661.
3. R. S. Bennink, Young-Kwon Yoon, R. W. Boyd, and J. E. Sipe, "Accessing the optical nonlinearity of metals with metaldielectric photonic bandgap structures," Opt. Lett. **24,** 1416–1418 (1999).
4. B. K. Canfield, S. Kujala, K. Jefimovs, Y. Svirko, J. Turunen, and M. Kauranen, "A macroscopic formalism to describe the second-order nonlinear optical response of nanostructures," J. Opt. A: Pure Appl. Opt. **24,** 1416–1418 (1999).
5. E. Palik, ed., *Handbook of Optical Constants of Solids I* (Academic Press, San Diego, 1985).
6. *Handbook of Chemistry and Physics* (CRC Press, Boca Raton, 1984).
7. J. A. Woollam Co., Inc., http://www.jawoollam.com/index.html
8. LEO 1550 Scanning electron microscope is manufactured by Nano Technology Systems Division of Carl Zeiss SMT, formerly known as LEO Elektronenmikroskopie GmbH, http://www.zeiss.com/
9. J. A. Woollam Co., Inc., http://www.jawoollam.com/wvase32.html
10. W. H. Press, S. A. Teukolsky , W. T. Vetterling, and B. P. Flannery, *Numerical Recipes in C, 2nd ed.* (Cambridge Univ. Press, Cambridge, 1992).
11. J.H. Weaver, C. G. Olson, and D. W. Lynch, "Optical investigation of the electronic structure of bulk Rh and Ir," Phys. Rev. B. **15,** 4115–4118 (1977).
12. C. V. Thompson, "Structure evolution during processing of polycrystalline films," Annu. Rev. Mater. Sci. **30,** 159–190 (2000).
13. E. Lee, N. Truong, B. Prater, and J. Kardokus, "Copper alloys and alternative barriers for sub-45 nm nodes," Semiconductor International, (7/1/2006).
14. K. L. Chopra, *Thin Film Phenomena* (Robert E. Krieger Publishing Company, New York, 1979).
15. G. Hass, W. R. Hunter, and R. Tousey, "Reflectance of evaporated aluminium in the vacuum ultraviolet," J. Opt. Soc. Am. **46,** 1009–1012 (1956).

#81330 - $15.00 USD Received 21 Mar 2007; revised 18 Jun 2007; accepted 28 Jun 2007; published 10 Aug 2007

1. Introduction

Recently, there has been an increasing interest in utilization of metallic nano- and microstructures. These kinds of structures exhibit unique properties and can be used in a wide range of applications including devices such as chiral polarization rotators [1] and metallic mesh structures that are used as infrared filters [2]. Also resonance film stacks, where alternating layers of metal and dielectric material cause enhanced transmission [3] are well known. In the field of nonlinear optics, for example, L-shaped nanostructures offer novel means to show a second-order nonlinear optical response [4].

In order to design such devices and calculate the optical responses, the optical properties of the metallic structure should be known. In the literature [5, 6], accurate tabulated data exist for metals that are processed under extremely carefully prepared conditions to have compact structures and smooth surfaces. However, as is shown in this paper, the optical properties of these metals differ substantially from those of more commonly processed ones.

Generally, metallic nanostructures are fabricated into metallic thin films using lithographical processes. These thin films can be deposited by electroplating, sputtering, atomic layer deposition (ALD), and evaporation. Electroplating is an electrochemical process whereas sputtering and evaporation are physical processes. ALD is based on surface reactions and this is why the film growth during the process is self-limiting.

Thin films can be analyzed as a compound composed of air and metallic clusters, which means that the optical properties can be considered as effective. Since the volume of air and other inhomogeneities differs between different fabrication processes, it is inevitable that the optical properties are also unequal. For example, ALD makes it possible to produce compact structures, whereas evaporated films have more porous and non-uniform structure.

In this paper we compare the refractive indexes and extinction coefficients of evaporated aluminium and iridium films and atomic-layer-deposited iridium films. We demonstrate that the optical properties depend on the film deposition technique. We also show that the properties depend on film thickness. In the following section, we present the fabrication and analysis methods for the metal films. The experimental results for the refractive indexes and extinction coefficients are given in Section 3 and the conclusions are drawn in Section 4.

2. Fabrication and analysis methods

The aluminum and iridium films were evaporated by an electron beam gun. The target for aluminium was 99,999 % pure and for iridium 99,9 %. The evaporation rate for aluminium was 1.8–2.2 Å/s and for iridium 0.6–1.0 Å/s. The pressure at the beginning of the deposition processes was approximately 3×10^{-6} torr but in the case of iridium it rose to 5×10^{-5} torr during the evaporation. The substrate temperatures was held between 300 and 345 K. The substrates were mounted in a spherical holder and rotated to obtain uniform film thickness. The vapor deposition was controlled by using a shutter mounted above the targets. The shutter was opened when the targets were uniformly heated and the evaporation reached a constant speed, and it was closed when the desired film thickness was obtained.

The substrates for the evaporated aluminium and iridium films were fused silica plates of one inch diameter and 3 mm and 0.5 mm thick, respectively. The substrates were first cleaned in an ultrasonic cleaning bath filled with isopropanol. The surface roughness of the fused silica substrates was 11 ± 0.5 Å, which was measured with the variable angle spectroscopic ellipsometer (VASE) [7] and modelled by Bruggeman's effective medium theory. For the atomic-layer-deposited iridium, we used 1-mm-thick borosilicate substrates with a 5-nm-thick aluminium oxide adhesion layer. Borosilicate was chosen since it can withstand the heat required in the ALD process. The borosilicate substrates were cleaned in an ultrasonic cleaner filled with ethanol and water.

#81330 - $15.00 USD Received 21 Mar 2007; revised 18 Jun 2007; accepted 28 Jun 2007; published 10 Aug 2007

Cross section and surface images were taken using a LEO 1550 field emission scanning electron microscope (SEM) [8]. Optical measurements were made with a VASE that used a rotating analyzer design and thus made possible measurements over a broad wavelength range from 300 nm to 2000 nm at 10-nm intervals. The refractive indexes and extinction coefficients of aluminium and iridium were calculated using the Wvase32 [9] ellipsometric analysis program. This fitting software finds a minimum difference between the experimental data and calculated values using the Levenberg–Marquardt algorithm [10]. In the modelling, we assumed that each sample consisted of a homogenous metal film on a substrate. In the case of aluminium, we also included a 3-nm-thick alumina surface layer in the model.

With the VASE, we measured the ellipsometric parameters Ψ and Δ at two different angles, 65 and 75 degrees. In the case of non-opaque films we also measured the transmittance at normal incidence. The thicknesses of the non-opaque films were determined during the fitting procedure using initial values obtained from the thickness monitor in the evaporation chamber and also measured with a profilometer. In the case of opaque films, we did not have the same thickness sensitivity in the fitting process. Hence, the thicknesses reported for the opaque films were determined by the monitor in the evaporation chamber, the profilometer, and also by the SEM values, since the SEM resolution was better for the thicker films.

3. Results

The refractive indexes of different layer thicknesses for ALD and electron-beam-gun-evaporated iridium are compared to values presented in the literature [6] in Fig. 1(a). The literature values were for large polycrystalline samples that were cut from a crystal rod of iridium. The samples were mechanically polished to obtain specular surfaces, boiled in aqua regia, and heated in a vacuum of 10^{-7} torr to produce clean, strain-free surfaces for the optical measurements [11].

For both fabrication methods, the refractive indexes increase as the thickness decreases. However, for the ALD films, the change with thickness is not as large as for the evaporated ones, as one would expect since the ALD process produces tightly packed films with uniform structure. The refractive indexes have higher values than the literature values excluding the 144-nm-thick ALD film at visible wavelengths.

The extinction coefficients of the same samples are shown in Fig. 1(b). Also, in this case, the measured extinction coefficients of the ALD films are larger than the literature values for the entire wavelength range. On the contrary, the measured values for the evaporated films are smaller than those in the literature. However, they increase as the thickness decreases. The ALD films behave in the same way. Again, the thickness does not have as much effect on the extinction coefficients of the ALD films compared to the evaporated ones.

The behavior of the ALD films is caused by the nature of the ALD process. The tightly packed structure of the ALD films results in high refractive indexes and extinction coefficients. The thickness dependence, in turn, is a consequence of irregularities in the atomic structure that increase with the number of deposited layers. The more layers there are, the more defects exist, which lowers the refractive indexes and extinction coefficients. For evaporated iridium, the thickness dependence is mainly caused by poor adhesion and different thermal expansion coefficients of the fused silica substrate and iridium film. As the film thickness increases, the sizes and numbers of cracks in the film surface becomes so large that it lowers the refractive index and extinction coefficient of the film. In Fig. 2 the cracks in the surface of the 115-nm-thick evaporated iridium film are shown.

The refractive indexes for several thicknesses of the electron-beam-gun-evaporated aluminium films are shown and compared to the literature values [6] in Fig. 3(a). The literature values are for ultrahigh-vacuum-evaporated aluminium (more information was not available).

#81330 - $15.00 USD Received 21 Mar 2007; revised 18 Jun 2007; accepted 28 Jun 2007; published 10 Aug 2007

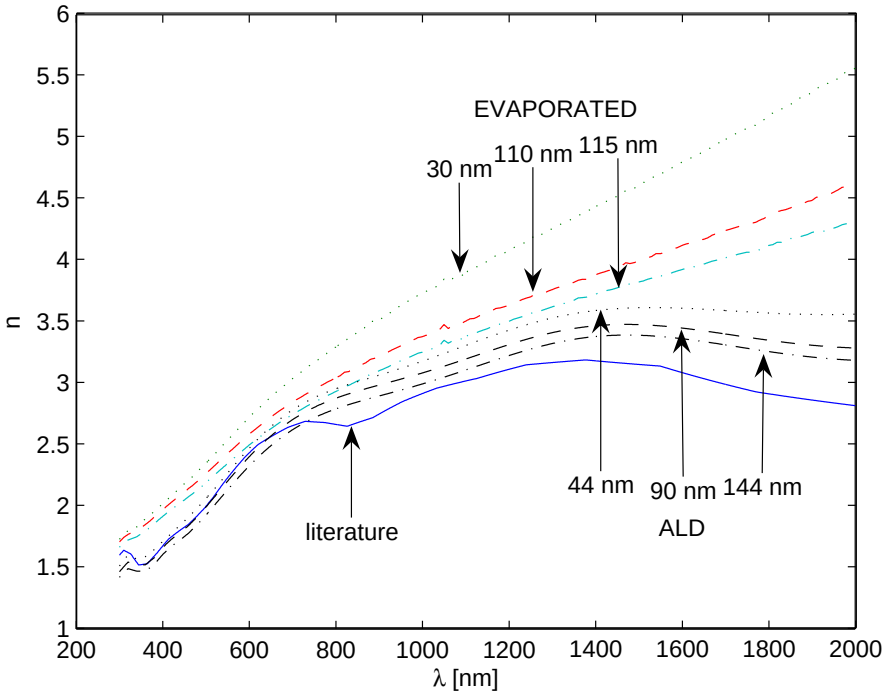

(a)

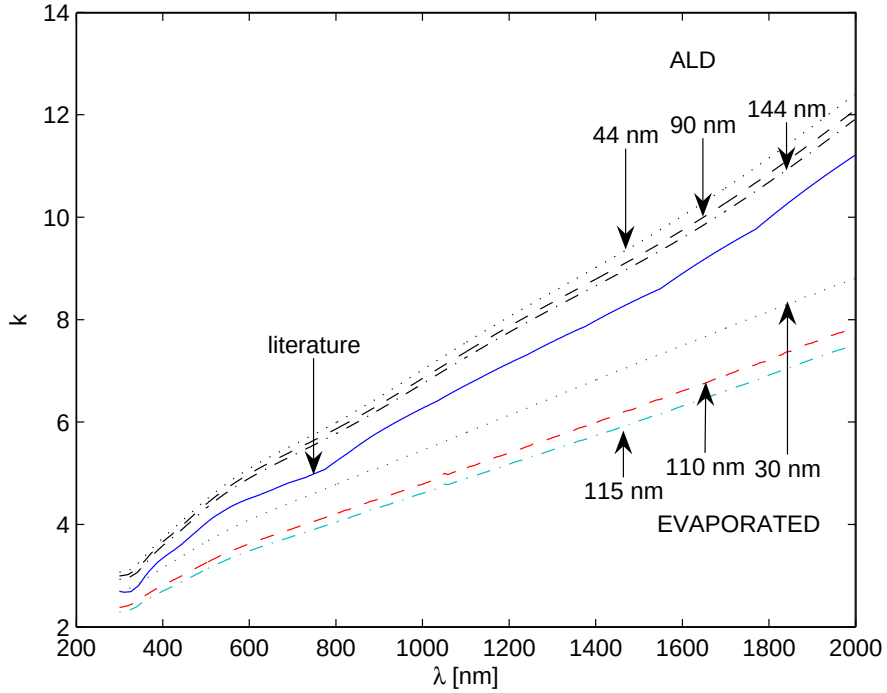

(b)

Fig. 1. Refractive indexes (a) and extinction coefficients (b) of 44 nm, 90 nm, and 144 nm thick atomic-layer-deposited iridium films compared to 30 nm, 110 nm, and 115 nm thick evaporated iridium films and the literature values [6] as a function of wavelength.

#81330 - $15.00 USD Received 21 Mar 2007; revised 18 Jun 2007; accepted 28 Jun 2007; published 10 Aug 2007

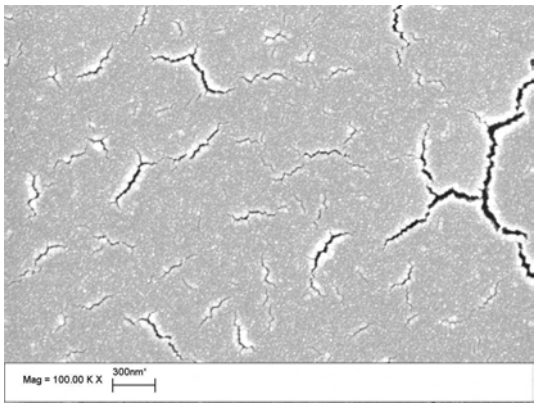

Fig. 2. Surface structure of the 115 nm thick evaporated iridium film. The cracks are due to a poor adhesion and different thermal expansion coefficients between the substrate and iridium.

As a whole, the values for the thicker films are closer to the ones in the literature. Nevertheless, in some cases the results are not consistent. For example, near a wavelength of 800 nm, the values for the 37-nm-thick layer are closer to the literature values than those for the 70-nm-thick layer. Corresponding results for the extinction coefficients can be found in Fig. 3(b).

The low extinction coefficient values of evaporated aluminium can be explained by considering the grain evolution of a thin film in the evaporation process. The large kinetic energy of electron-beam-gun-evaporated atoms enables them to migrate on the substrate surface to form different sizes of crystallites. Thus, the grain structure evolves during film growth, which often results in structure in which the grain size tends to be the same as and scale with the film thickness [12]. In this way the grain size of thicker films tends to be larger than that of thinner films. As long as the electronic mean free path length in the material is a small fraction of the distance between grain boundaries, the presence of these boundaries cannot significantly influence the conductivity. However, as the width or diameter of a grain approaches the mean free path length, a considerable fraction of the conduction electrons strike and scatter at the grain boundaries, reducing the conductivity and extinction coefficient [13]. This explains the decrease of the extinction coefficient as the film becomes thinner, particularly in the infrared region where optical absorption is dominated by the conduction electrons [14].

In Fig. 4(a) a top view of a 270-nm-thick electron-beam-gun-evaporated aluminium layer is shown. Comparing the grain size to that of a 100-nm-thick aluminium layer in Fig. 4(b), a significant difference can be seen. The average grain size of the 270-nm-thick layer seems to be almost 100 nm in diameter, nearly twice as large as for the thinner layer. A similar difference in the grain sizes can be seen in Figs. 5(a) and (b) where the cross-sectional views of 270 nm and 100 nm thick electron-beam-gun-evaporated aluminium layers on fused silica substrates are shown. In the cross-sectional figures, the grooves in the substrates were formed during the cutting of the sample plates and the nanometer-size particles on the substrates are sputtered gold that was used to increase the conductivity in SEM imaging.

The refractive index and extinction coefficient of evaporated aluminium also strongly depend on the proportion of alumina inside the thin film structure. A reasonable assumption is that the volume of alumina is higher for porous material, that is for thinner films, which results in more effective-like optical properties that are difficult to predict. The amount of alumina can be reduced with lower vacuum pressure and higher evaporation rate [15]. However, if we increase the evaporation rate, the surface roughness increases if we are not able to improve the vacuum.

#81330 - $15.00 USD Received 21 Mar 2007; revised 18 Jun 2007; accepted 28 Jun 2007; published 10 Aug 2007

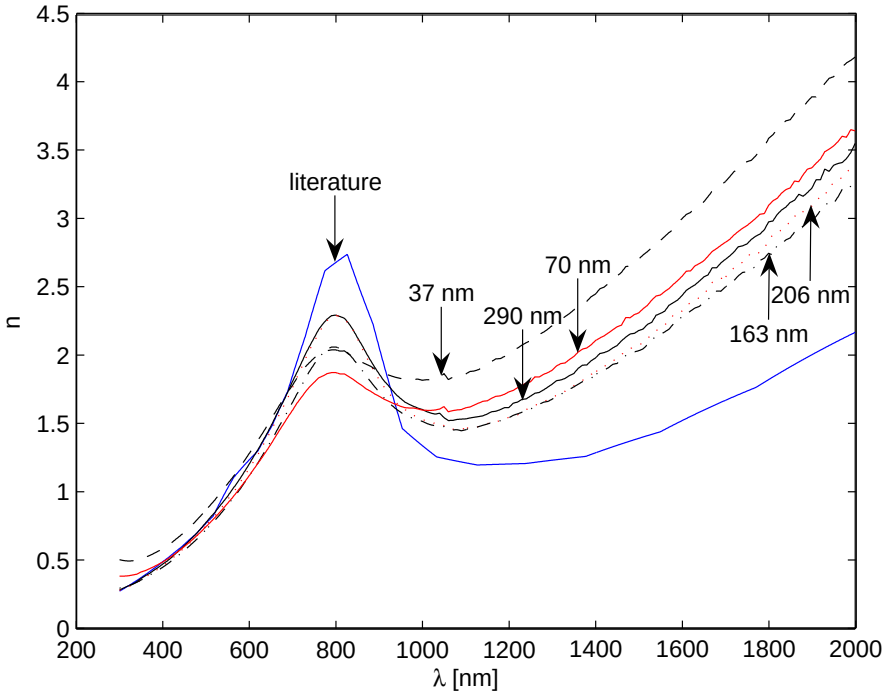

(a)

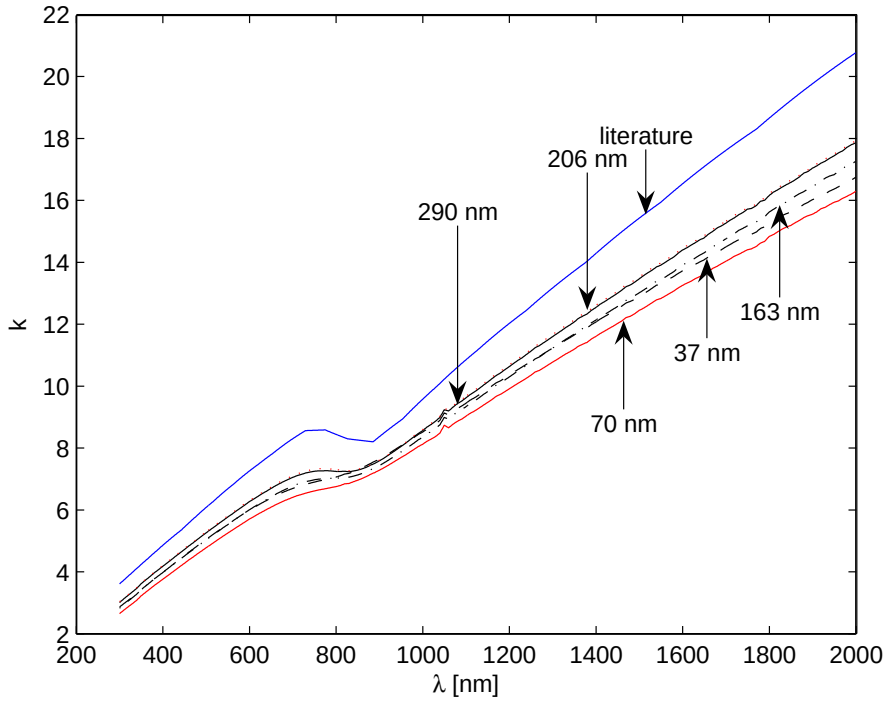

(b)

Fig. 3. Refractive indexes (a) and extinction coefficients (b) of 37 nm, 70 nm, 163 nm, 206 nm, and 290 nm thick evaporated aluminium films compared to aluminium values given in the literature [6] as a function of wavelength.

#81330 - $15.00 USD Received 21 Mar 2007; revised 18 Jun 2007; accepted 28 Jun 2007; published 10 Aug 2007

This in turn leads to less reliable ellipsometric measurements.

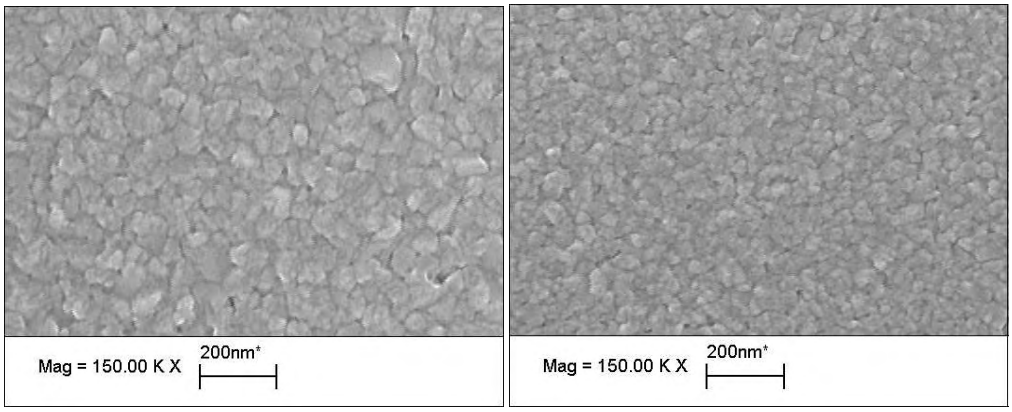

(a) (b)

Fig. 4. Top view of 270 nm (a) and 100 nm (b) thick electron beam gun evaporated aluminium layer.

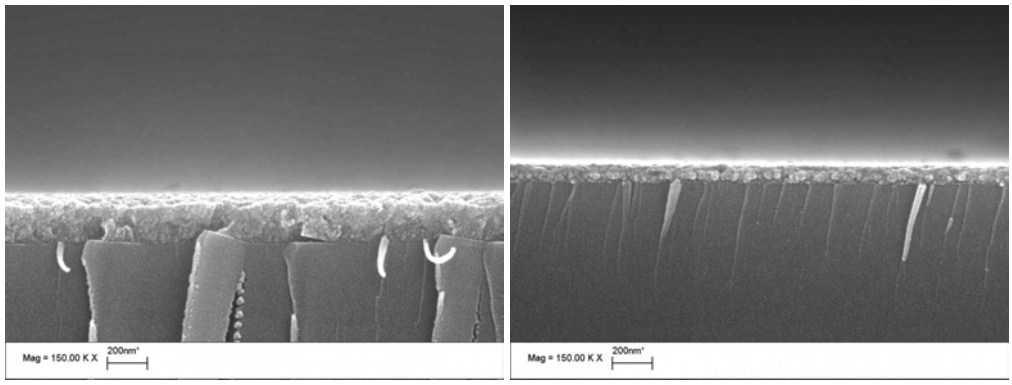

(a) (b)

Fig. 5. Cross-sectional view of 270 nm (a) and 100 nm (b) thick electron beam gun evaporated aluminium layer on fused silica substrate.

Typical relative errors for measured Ψ and Δ values are between 0.02–0.5 %. For transmittance, the numerical uncertainty is defined by the Wvase32 software as approximately 0.5 %. In Fig. 6(a) the 90 % confidence limits of the refractive indexes for the 30-nm-thick iridium and 163-nm-thick aluminum films are shown. Furthermore, the 90 % confidence limits for the extinction coefficients of the same samples are shown in Fig. 6(b). These figures represent the typical uncertainties for all of our measured films. It can be seen that the confidence limits are very close to the reported values. However, in the case of aluminum, the change in the thickness of the aluminum oxide surface layer in the modelling process produces much greater uncertainties than the 90 % confidence limits. We can approximate the change in n and k by estimating that the difference that we obtain by changing the thickness of the aluminium oxide layer in the modelling by 1 nm is roughly $1.25 \times 10^{-4} \times \lambda$[nm] for n and $3.5 \times 10^{-4} \times \lambda$[nm] for k. Nevertheless, if we assume that the thickness of the oxide layer is constant for all of our

#81330 - $15.00 USD Received 21 Mar 2007; revised 18 Jun 2007; accepted 28 Jun 2007; published 10 Aug 2007

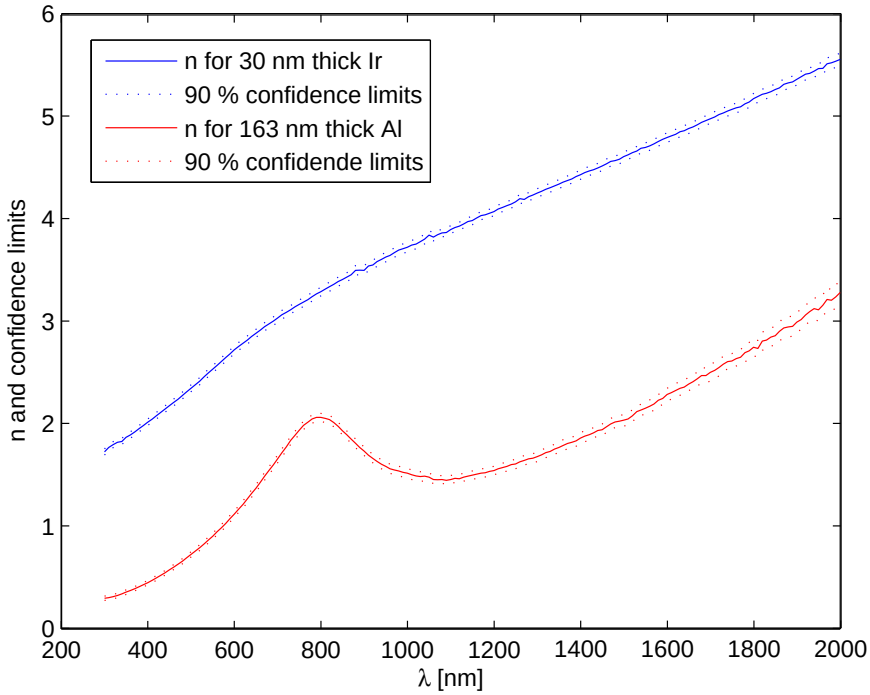

(a)

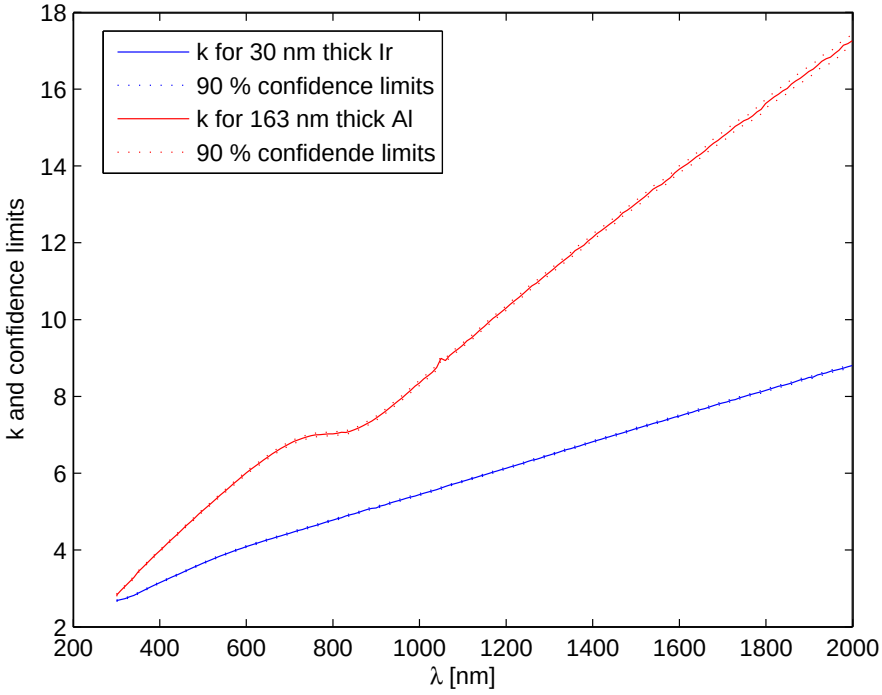

(b)

Fig. 6. 90 % confidence limits of refractive indexes (a) and extinction coefficients (b) for 30-nm-thick electron-beam-gun-evaporated iridium and for 163-nm-thick electron-beam-gun-evaporated aluminum films.

#81330 - $15.00 USD Received 21 Mar 2007; revised 18 Jun 2007; accepted 28 Jun 2007; published 10 Aug 2007

aluminium films, since the measurements were made on freshly prepared samples of the same age, the thickness dependence remains similar, even though the values for the refractive indexes and extinction coefficients change.

4. Conclusions

In this paper we have shown how the refractive indexes and the extinction coefficients of aluminium and iridium films depend on the thicknesses of the films. We have also shown how those properties depend on the deposition technique as well. It is probable that the same dependencies also apply to other metallic thin films.

These results indicate that in order to predict the optical behavior of thin metallic films, it is not necessarily advisable to use values published in the literature since they could have been measured on different thickness films prepared using different techniques from the studied materials. For example, if we calculate the transmittance of a 30-nm-thick evaporated iridium layer at a wavelength of 633 nm using the literature values and the values measured in this paper, the results differ by approximately 20 %. In the case of metallic nano- and microstructures, the optical values of the metal doubtless differ even from the values of a thin film with the same thickness.

Acknowledgment

This work was supported by the Finnish Graduate School of Modern Optics and Photonics. The funding received from the EU Network of Excellence on Micro-Optics (NEMO) is also appreciated. Ellipsometric fitting procedures were carried out in collaboration with Dr. Thomas Wagner from L.O.T. –Oriel Gmbh & Co. We would also like to thank Tero Pilvi for the preparation of the atomic-layer-deposited iridium samples, Vesa Karppinen for evaporating the aluminium and iridium samples, and Noora Heikkilä and Petri Pelli for their assistance in the measurements. Finally, we would like to acknowledge the reviewer for offering valuable comments and suggestions.

#81330 - $15.00 USD Received 21 Mar 2007; revised 18 Jun 2007; accepted 28 Jun 2007; published 10 Aug 2007

Paper **II**

A. Lehmuskero, V. Kontturi,
J. Hiltunen, and M. Kuittinen
"Modeling of laser colored
stainless steel surfaces by color
pixels"
Applied Physics B,
98, pp. 497–500, 2009.

Paper **III**

A. Lehmuskero, B. Bai, P. Vahimaa,
and M. Kuittinen
"Wire-grid polarizers in the
volume plasmon region"
Optics Express,
17, pp. 5481–5489, 2009.

III A. Lehmuskero, B. Bai, P. Vahimaa, and M. Kuittinen, “Wiregrid polarizers in the volume plasmon region,” *Opt. Express* 17, 5481–5489 (2009).

Wire-grid polarizers in the volume plasmon region

Anni Lehmuskero, Benfeng Bai, Pasi Vahimaa, and Markku Kuittinen

University of Joensuu, Department of Physics and Mathematics,
P.O. Box 111, FI-80101 Joensuu, Finland
anni.lehmuskero@joensuu.fi

Abstract: The properties of silver and aluminium wire-grid polarizers are examined in the volume plasmon frequency region where the transmittances of field with polarizations parallel and perpendicular to the grid lines are reversed with respect to their behavior outside the plasma region. Analysis of the behavior is conducted with effective approximate refractive index formulae and by simulations with rigorous Fourier modal method. The parallel polarization behaves as in a homogenous thin metal film while the perpendicular field is absorbed in the plasma region and transmitted otherwise. We further explain the performance by viewing the distribution of the field intensities inside the grating.

OCIS codes: (050.6624) Subwavelength structures; (050.2065) Effective medium theory; (160.3900) Metals; (230.5440) Polarization-selective devices; (250.5403) Plasmonics.

References and links

1. G. R. Bird, M. Parrish, "The wire grid as a near-infrared polarizer," J. Opt. Soc. Am. **50**, 886-891, (1960).
2. J.B. Young, H. A. Graham, E. W. Peterson, "Wire grid infrared polarizer," Appl. Opt. **4**, 1023–1026, (1965).
3. C. Pentico, E. Gardner, D. Hansen, R. Perkins, "New, high performance, durable polarizers for projection displays," SID Int. Symp. Digest Tech. Papers **32**, 1287–1289, (2001).
4. L. Chen, J. J. Wang, F. Walters, X. Deng, M. Buonanno, S. Tai, X. Liu, "Large flexible nanowire grid visible polarizer made by nanoimprint lithography," Appl. Phys. Lett. **90**, 063111, (2007).
5. D. Pines, "Collective energy losses in solids," Rev. Mod. Phys. **28**, 184–199, (1956).
6. R. H. Ritchie, E. T. Arakawa, J. J. Kowan, R. N. Hamm, "Surface plasmon resonance effect in grating diffraction," Phys. Rev. Let. **21**, 1530–1533, (1968).
7. F. J. García-Vidal, J. Sánchez-Dehesa, A. Dechelette, E. Bustarret, T. López-Ríos, T. Fournier, B. Pannetier, "Localized surface plasmons in lamellar metallic gratings," J. Lightwave Technol. **17**, 2191–2195, (1999).
8. W. L. Barnes, A. Dereux, T. W. Ebbesen, "Surface plasmon subwavelength optics," Nature **424**, 824–830, (2003).
9. C. Ropers, C. C. Neacsu, T. Elsaesser, M. Albrecht, M. B. Raschke, C. Lienau, "Grating-coupling of surface plasmons onto metallic tips: a nanoconfined light source," Nano Letters **7**, 2784–2788, (2007).
10. J. Homola, "Present and future of surface plasmon resonance biosensors," Anal. Bioanal. Chem. **377**, 528–539, (2003).
11. S. E. Maier, *Plasmonics: Fundamentals and Applications* (Springer Science+Business Media LLC, New York, 2007).
12. edited by M. L. Brongersma, P. G. Kik *Surface Plasmon Nanophotonics* (Springer, Dordrecht, 2007).
13. R. W. Wood, "On a remarkable case of uneven distribution of light in a diffraction grating spectrum," Phil. Mag. **4**, 396–402, (1902).
14. M. Honkanen, V. Kettunen, M. Kuittinen, J. Lautanen, J. Turunen, B. Schnabel, and F. Wyrowski, "Inverse metal-stripe polarizers," Appl. Phys. B **68**,81–85, (1999).
15. U. Fano, "The theory of anomalous diffraction gratings and of quasi-stationary waves on metallic surfaces," J. Opt. Soc. Am. **31**, 213–222, (1941).
16. G. Schider, J. R. Krenn, W. Gotschy, B. Lamprecht, H. Ditlbacher, A. Leitner, and F. R. Aussenegg, "Optical properties of Ag and Au nanowire gratings," J. Appl. Phys. **90**, 3825–3830, (2001).

#105573 - $15.00 USD Received 2 Jan 2009; revised 27 Feb 2009; accepted 28 Feb 2009; published 23 Mar 2009

17. A. Christ, S. G. Tikhodeev, N. A. Gippius, J. Kuhl, and H. Giessen, "Plasmon polaritons in a metallic photonic crystal slab," Phys. Status Solidi C **0**, 1393–1396, (2003).
18. E. A. Taft, H. R. Phillip, "Optical constants of silver," Phys. Rev. **121**, 1100–1103, (1961).
19. F. Wooten, *Optical Properties of Solids* (Academic press, New York, 1972).
20. ed-in-chief D. R. Lide, *Handbook of Chemistry and Physics, 85th edit.* (CRC Press, Boca Raton, 2005).
21. M. Kuittinen, J. Turunen, P. Vahimaa, "Subwavelength-structured elements" in *Diffractive Optics for Industrial and Commercial Applications*, J. Turunen, F. Wyrowski, eds. (Cambridge university press, New York, 1998).
22. J. Turunen, "Diffraction theory of microrelief gratings" in *Micro-Optics, Elements, Systems, and Applications*, H. P. Herzig, ed. (Taylor & Francis, London, 1997).
23. P. Lalanne, G. M. Morris, "Highly improved convergence of the coupled-wave method for TM polarization," J. Opt. Soc. Am. A **13**, 779–784, (1996).

1. Introduction

Wire-grid gratings are known to be able to transmit light that has an electric field perpendicular to the metallic wires and to reflect light with an electric field parallel to the wires. Thus they are mainly utilized as polarizers or polarizing beam splitters in applications such as projection displays. Wire-grid polarizers have been available for infrared region since 1960's [1, 2], however, it was not until last few years that they were fabricated also for visible light [3, 4] and started to be commercialized.

The term plasmon was introduced in 1956 [5], although plasmons were known from the beginning of the 20th century. Plasmons are collective electron oscillations that can be categorized into two main groups; volume plasmons and surface plasmons. Surface plasmons, that is the confined electron oscillations at metal/insulator surfaces, in connection with gratings have been a subject in various papers, see for example Refs. [6–8]. Both theoretical and experimental research has been made and many applications, such as nanoconfined light sources [9] and biological sensors [10] have been proposed based on them [11, 12].

In this paper, however, we investigate wire-grid gratings in the vicinity of the volume plasmon frequency, the fundamental frequency of a free oscillation of the electron sea in the metal. For ideal metals, the volume plasma frequency can be defined from the Drude model by setting the complex permittivity to zero. Therefore, the spectral position of the resonance is characteristic to the bulk material properties and always independent on the surface parameters, in contrast to the surface plasmons.

In the following, we introduce a switching wire-grid grating that works as a traditional polarizer at off-resonance wavelengths but as an inversed polarizer at the volume plasma wavelength. A similar inverse behavior has also been reported earlier for the Wood's anomaly [13] when the grating period is slightly smaller than the wavelength of light [14]. The first theoretical analysis of the plasmon-type Wood's anomaly in metallic gratings was given by Fano [15]. There are also some works about nanowires where increase of the extinction for perpendicular polarization has been obtained by particle plasmons, the localized surface plasmons [16, 17].

In the next section we specify the conditions for volume plasma resonance and provide effective medium theory to describe the grating. In Section 3 we introduce wire-grid polarizers with the inverse behavior at the plasma wavelength and analyze the behavior with the field intensities and the effective medium theory. Finally we end our work with the conclusions.

2. Theory

There are two conditions for the volume plasmon resonance of real metals. Firstly, the real part of the permittivity has to be zero

$$\varepsilon_1 = 0 \tag{1}$$

and secondly, the imaginary part has to be much smaller than unity [18, 19]

$$\varepsilon_2 \ll 1. \tag{2}$$

#105573 - $15.00 USD Received 2 Jan 2009; revised 27 Feb 2009; accepted 28 Feb 2009; published 23 Mar 2009

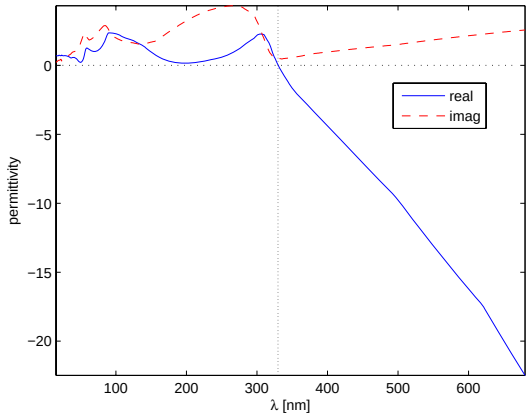

Fig. 1. Real part (solid line) and imaginary part (dashed line) of the complex permittivity for silver. The values are calculated from the refractive indexes given in [20].

Normally this would not happen at all or it would happen only in the extreme ultraviolet region for metals such as lithium and aluminium, whereas for silver the conditions are satisfied in near UV at 330 nm as we can see in Fig. 1. This longer wavelength is more convenient because the period has to be much smaller than the operating wavelength for wire-grid polarizers, which sets certain boundaries for the possible fabrication process.

Let us now define the perpendicular field/polarization to indicate light with electric field perpendicular to the grating lines, and the parallel field/polarization to indicate light with electric field parallel to the lines. The behavior of subwavelength grating is a consequence of material properties as well as structure parameters. The grating can be considered as a birefringent homogenous thin film with different approximate effective refractive indexes for the perpendicular and parallel polarizations. The relationship between complex permittivity ε and complex refractive index n for non-magnetic medium is given by

$$n = \sqrt{\varepsilon}. \tag{3}$$

We can derive the approximate effective refractive indexes from the theory of periodic waveguides by retaining only the zeroth order terms in the eigenvalue equations for the perpendicular and parallel fields [21]. This procedure gives the following equations:

$$n_{\perp}^{\mathrm{eff}} = [f n_1^{-2} + (1-f) n_2^{-2}]^{-1/2}, \tag{4}$$

for the perpendicular polarization and

$$n_{\parallel}^{\mathrm{eff}} = [f n_1^{2} + (1-f) n_2^{2}]^{1/2}, \tag{5}$$

for the parallel polarization. Refractive indexes of the modulated grating area are denoted by n_1 and n_2, and f stands for the fill factor of medium with n_1. In this paper we are considering gratings for which n_1 is metal and n_2 is air. The grating geometry is given in Fig. 2.

Equations (4) and (5) hold sufficiently well in the quasi-static limit $d/\lambda \to 0$. Here d is the period of the grating and λ is the wavelength of light. In other situation the effective refractive indexes have to be calculated rigorously. For that purpose we have used Fourier modal method (FMM) for which the effective refractive index is obtained by dividing the zeroth order

#105573 - $15.00 USD Received 2 Jan 2009; revised 27 Feb 2009; accepted 28 Feb 2009; published 23 Mar 2009

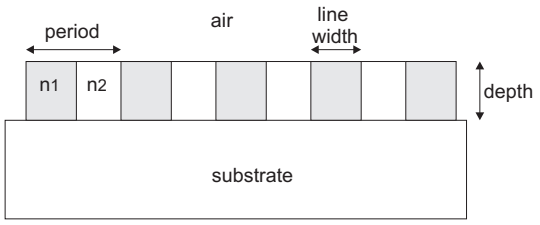

Fig. 2. Grating geometry.

propagation constant, γ_0, by the wave number in vacuum, k,

$$\hat{n}_{eff} = \gamma_0/k, \tag{6}$$

where $k = 2\pi/\lambda$.

3. Results and analysis

Transmittance and absorbance at the plasma region for silver grating are illustrated in Figs. 3(a) and (b), respectively. The results have been calculated using FMM that is based on Refs. [22, 23], for a grating with the period 30 nm, the depth 100 nm, and the line width 5 nm. The substrate material is silica and the angle of incidence is normal to the grating surface. Solid line indicates the electric field parallel to the grating lines and the dashed line represents the perpendicular field.

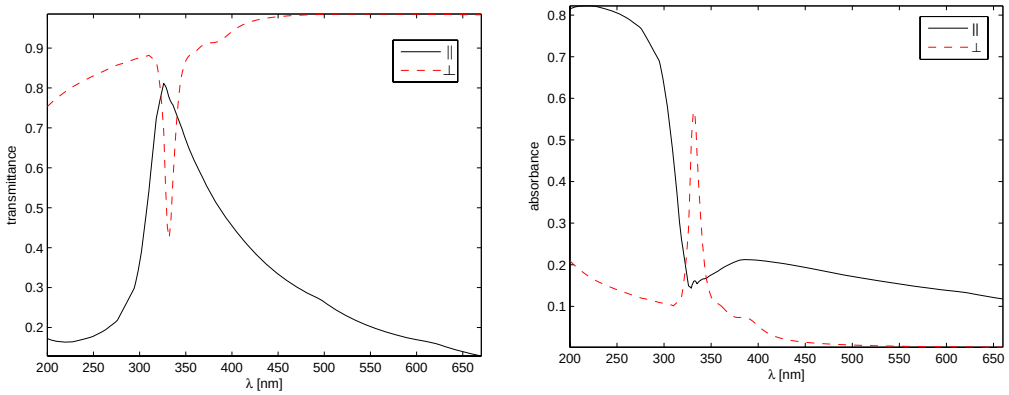

(a) (b)

Fig. 3. Transmittance (a) and absorbance (b) of parallel (||) and perpendicular (⊥) polarizations for a silver wire-grid grating on silica substrate with period 30 nm, depth 100 nm, and line width 5 nm.

The transmittance spectra are typical for a wire-grid polarizer below and above the plasmon region. The perpendicular field is transmitted and the parallel field is absorbed below and mostly reflected above the plasma wavelength. But as we reach the plasmon region the situation changes rapidly to the opposite. The grating becomes an inverse polarizer letting mainly the parallel field pass through the grating.

If we want to understand the underlying physics of this unusual behavior, we should examine the field intensities inside the grating. The intensities of the perpendicular and parallel fields at the wavelength 630 nm and at the plasma wavelength 330 nm are illustrated in Figs. 4(a)–(d).

#105573 - $15.00 USD Received 2 Jan 2009; revised 27 Feb 2009; accepted 28 Feb 2009; published 23 Mar 2009

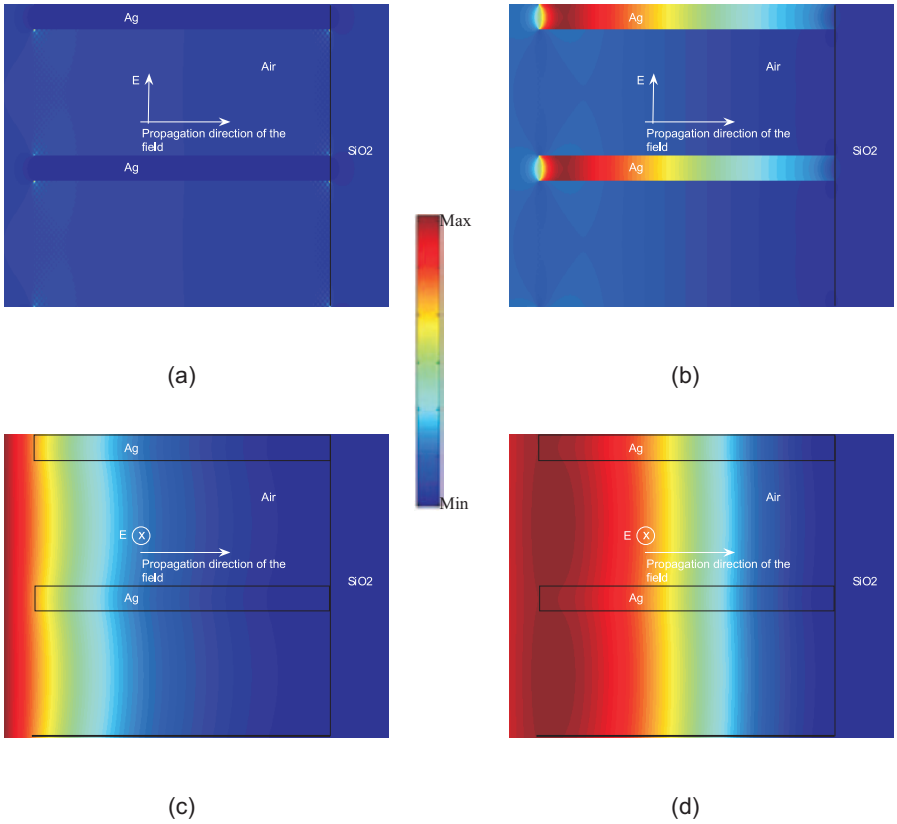

Fig. 4. Intensities in the cross-sectional view of the grating. (a) and (b) show the perpendicular field for the wavelengths 630 nm and 330 nm, respectively. (c) and (d) are for the parallel field for the same wavelengths 630 nm and 330 nm, respectively.

Let us first consider the parallel field. From Fig. 3(b) we notice that most part of the field is absorbed below the plasma wavelength. This is because the field penetrates into the metal. And why part of the field does not slip trough the air grooves to the other side of the grating, is that the parallel field has to be continuous in the lateral direction according to the boundary conditions. Moreover, because of the subwavelength structure, the parallel field is almost constant in lateral direction as seen in Fig 4(c). Thus, the field in the air grooves behaves the same as in the metal wires, it attenuates along the propagation.

At the plasma region, the metal is more like dielectric with a small extinction coefficient. Therefore, the parallel field penetrates again into the metal. However, now the absorption of silver is small and the area of the metal wires is small compared to the air gaps between them. Thus, the small absorption of silver does not effect on the field and the field is transmitted, as seen in Fig. 4(d). In other words, in this case the transmission is solely defined by the proportion of the transparent area, air.

Above the plasma region silver is a good conductor. Therefore the parallel field cannot penetrate into the metal and is reflected, as seen in Fig. 4(c). Overall, it can be concluded that the parallel field acts the same as it would in the case of thin silver film.

The situation at the plasma wavelength can be also approached from the viewpoint of the effective refractive index and to consider the grating as an effectively homogenous thin film.

#105573 - $15.00 USD Received 2 Jan 2009; revised 27 Feb 2009; accepted 28 Feb 2009; published 23 Mar 2009

For ideal metals at the plasma wavelength it holds that $\Re\{n\} = \Im\{n\} \sim 0$. Thus, we can expand Eq. (5) in Taylor series and take only the first term into account, which gives us an approximation for the effective refractive index

$$n_{\parallel}^{\text{eff}} \approx \sqrt{1-f}. \tag{7}$$

It can be seen from Eq. (7) that the grating indeed acts as dielectric with refractive index defined by the fill factor at the plasma wavelength. The corresponding values for silver at this wavelength are $\Re\{n\} = \Im\{n\} \approx 0.48$. Therefore we would have to take more terms from the Taylor expansion which would lead to an appearance of a small imaginary part for the effective refractive index. This is consistent with the fact that in the case of silver, a small part of the field is absorbed.

The behavior of the perpendicular field can be explained by the boundary conditions according to which the normal component of the electric displacement density D has to be continuous across a boundary. Thus, in the modulated grating region it applies that

$$D_{\text{air}} = D_{\text{Ag}} \Leftrightarrow \varepsilon_{\text{air}} E_{\text{air}} = \varepsilon_{\text{Ag}} E_{\text{Ag}}, \tag{8}$$

where E is the electric field. For off-resonance wavelengths it holds that $|\varepsilon_{\text{Ag}}| \gg |\varepsilon_{\text{air}}|$. Then the intensity of the field in air must be much higher than in the metal

$$|E_{\text{Ag}}|^2 \ll |E_{\text{air}}|^2. \tag{9}$$

This means that the field is squeezed mostly in air and since air does not posses any extinction the field is transmitted, as shown in Fig. 3 and Fig. 4(a).

At the plasma wavelength we have the opposite situation: $|\varepsilon_{\text{Ag}}| \ll |\varepsilon_{\text{air}}|$. From this it follows that

$$|E_{\text{Ag}}|^2 \gg |E_{\text{air}}|^2. \tag{10}$$

Thus, the field is highly confined in the metal and gets damped, due to the absorption of silver, when the depth of the wires is more than the skin depth. However, there still remains a small part of the perpendicular field that travels in the air grooves, as seen in Fig. 4(b). That part is transmitted and therefore the transmittance is not completely zero.

Again, we can expand the effective refractive index of the perpendicular field given by Eq. (4) in Taylor series. Assuming the ideal case at the plasma wavelength $\Re\{n\} = \Im\{n\} \sim 0$, the first term approximation gives us

$$n_{\perp}^{\text{eff}} \approx \frac{\hat{n}_1}{\sqrt{f}}. \tag{11}$$

Thus, the behavior of the grating is determined by the nature of silver, which is absorptive in the plasma region. Also now this approach is in good correlation with the results given above.

Many metals, such as gold, have too high imaginary part of the permittivity when $\varepsilon_1 = 0$. This would mean a considerable absorption for the both polarizations and no similar inverse behavior would occur.

The effective refractive indexes calculated with Eqs. (4) and (5) are presented in Fig. 5. The imaginary part is responsible for the extinction of the electric field and the real part the reduction of the speed of light. It is seen that the imaginary part stays low for the perpendicular field, but in the plasmon region it becomes significant and exceeds the corresponding value of the parallel field. In contrast, the extinction of the parallel field is high everywhere else but in the plasma region. These results correlate well with the transmittance values. A change occurs also in the real part of the refractive indexes, especially for the perpendicular field that has a dip at the plasma resonance. In conclusion, at off-resonance the effective medium behaves like

#105573 - $15.00 USD Received 2 Jan 2009; revised 27 Feb 2009; accepted 28 Feb 2009; published 23 Mar 2009

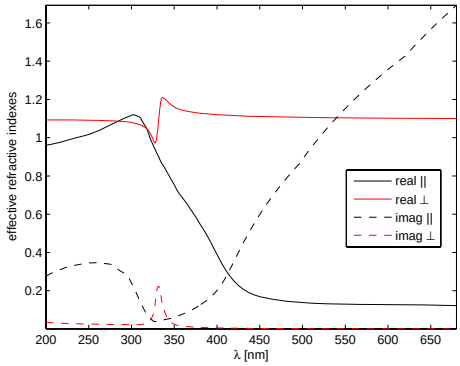

Fig. 5. Effective refractive indexes as a function of wavelength for a silver grating with the same grating parameters as in Fig. 3. Black lines indicate the parallel field and red lines the perpendicular. Solid lines represents the real parts and dashed lines the imaginary parts.

dielectric and at the resonance like absorptive metal for the perpendicular polarization. For the parallel field the medium is almost like dielectric at the plasma wavelength, absorptive metal below it, and good conductor above it.

Unfortunately, inverse silver polarizer even with plasma resonance near the visible spectrum is not likely to be fabricated with the period of 30 nm and the line width 5 nm. More reasonable feature size could be 50 nm that can be achieved with electron beam lithography. Therefore, we calculated transmittances for silver grating with more practical parameters. The results are shown in Fig. 6(a). The period of the grating is 100 nm, line width 50 nm and height 100 nm. The approximate formulae Eqs. (4) and (5) are no longer valid because the period is close to the wavelength. We have therefore used Eq. (6) to determine the effective refractive indexes in Fig. 6(b).

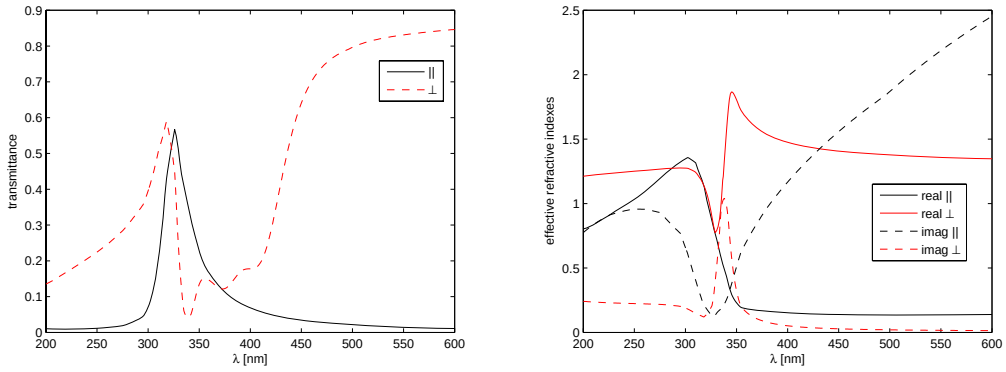

(a) (b)

Fig. 6. Transmittances (a) and effective refractive indexes (b) for a silver grating with period 100 nm, fill factor 0.5 and height 100 nm.

The interaction of light with the grating is now more complicated than in the previous case because of the structure dimensions so large that it can not be analyzed as in the quasi-static limit. It is seen that the parallel field behaves characteristically the same as before but the

#105573 - $15.00 USD Received 2 Jan 2009; revised 27 Feb 2009; accepted 28 Feb 2009; published 23 Mar 2009

perpendicular field has now higher extinction coefficient and lower transmittance below the resonance wavelength. Furthermore, the transmittance peak and the extinction minimum for the parallel field have remained their position but for the perpendicular field the transmission minimum is now shifted to 339 nm.

The performance of the silver wire-grid grating could be further optimized so that the transmittance contrast of the two polarizations at the plasma wavelength goes over hundred. In such a case, the transmittance would be near zero for the parallel field at off-resonance and for the perpendicular field at the resonance. Then the contrast would also be high at off-resonance. The drawback is that below the resonance the transmittance of the perpendicular field would drop down to near 10 %. Herein, it must be reminded that the bulk resonance induced inverse behavior is a consequence of the material property and therefore its position cannot be changed by structure optimization. This is of course a limiting factor, but on the other hand, because of the structure independence, the performance of the grating is not so sensitive to manufactural defects.

As mentioned earlier in Section 2, aluminium has a plasma wavelength in extreme UV, more precisely at 82 nm. Again, the quasi-static approximation does not apply and the performance of the grating as a polarizer falls short of perfection. Regardless, the performance can be enhanced by replacing the substrate layer with air and thus preventing the propagation of other orders than zeroth in the substrate. This is seen from the grating equation that defines the maximum wavelength that generates higher diffraction orders as $\lambda_{\max} = n_s d$, where n_s is the refractive index of the substrate and d the grating period.

Transmittances and effective refractive indexes around the plasma wavelength for a self-supporting aluminium wire-grid polarizer are given in Fig. 7(a) and (b), respectively. For this

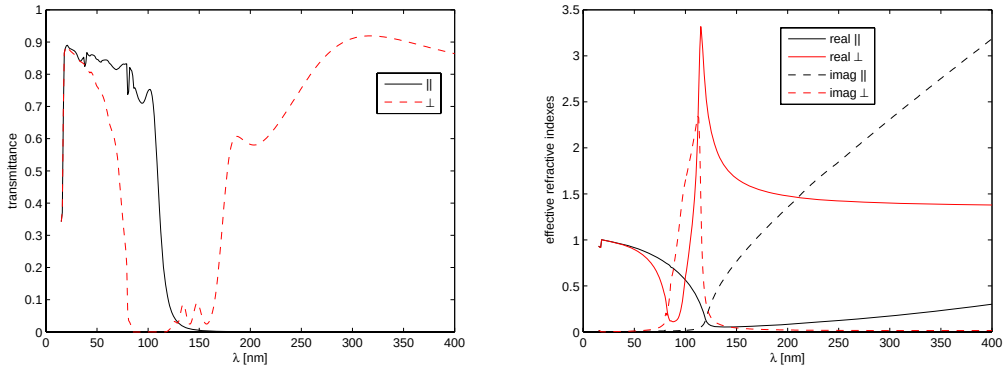

(a) (b)

Fig. 7. Transmittances (a) and effective refractive indexes (b) for a self-supporting aluminium grating with period 40 nm, fill factor 0.5 and height 100 nm.

grating the period is 40 nm, line width 20 nm, and height 100 nm. The grating does not act as a polarizer in the domain where the wavelength is smaller than the grating period because many higher orders are propagating. But as we get closer to the plasma wavelength, we obtain the switched transmittances and switched imaginary parts of effective refractive indexes given by Eq. (6). In the wavelength range of 80–105 nm the transmission for the perpendicular field drops to zero while the transmission of the parallel field is around 80 %. This is exactly the opposite to the behavior at wavelengths above 250 nm. Therefore, the aluminium wire-grid can be regarded as a 2D photonic crystal with inversed band gap structures. Above the wavelength 200 nm the performance is characteristic of a wire-grid polarizer with a contrast of 10 000 and

#105573 - $15.00 USD Received 2 Jan 2009; revised 27 Feb 2009; accepted 28 Feb 2009; published 23 Mar 2009

higher.

4. Conclusions

We have introduced a switching wire-grid polarizer for which the transmittances of the polarization parallel and perpendicular to the grating lines are reversed at the volume plasma wavelength. The polarizer transmits the perpendicular field in the off-resonance region and absorbs it near the resonance, while the parallel field acts as in a thin metal film. The inverse behavior has been investigated and explained with the analysis of the boundary conditions, field intensity distribution, and the effective refractive indexes, that correlated well with each other.

It was shown that the change from normal polarizer into inverse one was most evident when the grating period was much smaller than the plasma resonance wavelength. Although this would set challenges for the present-day fabrication methods due to the tiny dimensions, it does not prevent its potential application as a functional device when new nanofabrication techniques become available.

Acknowledgment

This work was supported by the Finnish Graduate School of Modern Optics and Photonics. The EU Network of Excellence on Micro-Optics (NEMO) and the Research and Development Project on Nanophotonics funded by the Ministry of Education are acknowledged as well. We would also like to thank Prof. Martti Kauranen for the fruitful discussions.

#105573 - $15.00 USD Received 2 Jan 2009; revised 27 Feb 2009; accepted 28 Feb 2009; published 23 Mar 2009

Paper **IV**

A. Lehmuskero, I. Vartiainen,
T. Saastamoinen, T. Alasaarela, and
M. Kuittinen

"Absorbing polarization selective resonant gratings"

accepted in Optics Express

IV A. Lehmuskero, I. Vartiainen, T. Saastamoinen, T. Alasaarela, and M. Kuittinen, “Absorbing polarization selective resonant gratings,” *Opt. Express* (accepted) (2010).

Absorbing polarization selective resonant gratings

Anni Lehmuskero,[1,*] **Ismo Vartiainen,**[1] **Toni Saastamoinen,**[1] **Tapani Alasaarela,**[2] **and Markku Kuittinen**[1]

[1]*University of Eastern Finland, Department of Physics and Mathematics, P.O. Box 111, FI-80101 Joensuu, Finland,*
[2]*Aalto University, Micronova, P.O. Box 13500, FI-00076 Aalto, Finland*
**anni.lehmuskero@uef.fi*

Abstract: We introduce resonant absorbers that consist of linear metal wires embedded inside of a titanium dioxide grating. We show that in these structures the guided-mode resonance may lead to the almost total absorption of one polarization component and greatly enhance the absorption in localized surface plasma resonance. In addition, we show that the structures have potential to function as filters or polarizing beamsplitters. Absorption of 99.67 % has been obtained together with the contrast of 6600 at the wavelength of 532 nm. This corresponds the extinction of 8.8597. The results have been verified experimentally by fabricating an absorbing filter with electron beam lithography and atomic layer deposition technique. The absorption is remarkably high considering the thickness of the structures which is only 219–333 nm.

OCIS codes: (050.2770) Gratings; (260.5740) Resonance; (230.5440) Polarization-selective devices.

References and links

1. A. Hohenau, A. Leitner, and F. R. Aussenegg, "Near-field and far-field properties of nanoparticle arrays," in *Surface Plasmon Nanophotonics* (Springer, Dordrecht, 2007).
2. S. E. Maier, *Plasmonics: Fundamentals and Applications* (Springer Science+Business Media LLC, New York, 2007).
3. G. Schider, J. R. Krenn, W. Gotschy, B. Lamprecht, H. Ditlbacher, A. Leitner, and F. R. Aussenegg, "Optical properties of Ag and Au nanowire gratings," J. Appl. Phys. **90**, 3825–3830 (2001).
4. D. M. Schaadt, B. Feng, and E. T. Yu, "Enhanced semiconductor optical absorption via surface plasmon excitation in metal nanoparticles," Appl. Phys. Lett. **86**, 063106 (2005).
5. S. S. Wang and R. Magnusson, "Theory and applications of guided-mode resonance filters," Appl. Opt. **32**, 2606–2613 (1993).
6. S. S. Wang and R. Magnusson, "Multilayer waveguide-grating filters," Appl. Opt. **34**, 2414–2420 (1995).
7. R. Magnusson and M. Shokooh-Saremi, "Physical basis for wideband resonant reflectors," Opt. Express **16**, 3456–3462 (2008).
8. X. Fu, K. Yi, J. Shao, and Z. Fan, "Nonpolarizing guided-mode resonance filter," Opt. Lett. **34**, 124–125 (2009).
9. A. Christ, S. G. Tikhodeev, N. A. Gippius, J. Kuhl, and H. Giessen, "Waveguide-Plasmon Polaritons: Strong Coupling of Photonic and Electronic Resonances in a Metallic Photonic Crystal Slab," Phys. Rev. Lett. **91**, 83901 (2003).
10. S. Linden, J. Kuhl, and H. Giessen, "Controlling the Interaction between Light and Gold Nanoparticles: Selective Suppression of Extinction," Phys. Rev. Lett. **86**, 4688–4691 (2001).
11. L. Novotny and B. Hecht, *Principles of Nano-Optics*, (Cambridge university press, Cambridge, 2006).
12. K. L. Kelly, E. Coronado, L. L. Zhao, and G. C. Schatz, "The Optical Properties of Metal Nanoparticles: The Influence of Size, Shape, and Dielectric Environment," J. Phys. Chem. B **107**, 668–677 (2003).

#136219 - $15.00 USD Received 7 Oct 2010; revised 10 Nov 2010; accepted 12 Nov 2010; published 10 Dec 2010

13. L. A. Sweatlock, S. A. Maier, H. A. Atwater, J. J. Penninkhof, and A. Polman, "Highly confined electromagnetic fields in arrays of strongly coupled Ag nanoparticles," Phys. Rev. B **71**, 235408 (2005).
14. H. Li, Q. Liu, S. Xie, X. Zhoua, H. Xia, and R. Zhouc, "Particle plasmons resonant characteristics in arrays of strongly coupled gold nanoparticles," Solid State Commun. **149**, 239–242 (2009).
15. J. P. Kottmann and O. J. F. Martin, "Plasmon resonant coupling in metallic nanowires," Opt. Express **8**, 655–663 (2001).
16. J. Turunen, "Diffraction theory of microrelief gratings," in *Micro-Optics, Elements, Systems, and Applications*, H. P. Herzig, ed. (Taylor & Francis, London, 1997).
17. J. J. Wang, L. Chen, X. Liu, Paul Sciortino, F. Liu, F. Walters, and X. Deng, "30-nm-wide aluminum nanowire grid for ultrahigh contrast and transmittance polarizers made by UV-nanoimprint lithography," Appl. Phys. Lett. **89**, 141105 (2006).
18. T. Alasaarela, T. Saastamoinen, J. Hiltunen, A. Säynätjoki, A. Tervonen, P. Stenberg, M. Kuittinen, and S. Honkanen, "Atomic layer deposited titanium dioxide and its application in resonant waveguide grating," Appl. Opt. **49**, 4321–4325 (2010).
19. J. P. Kottmann and O. J. F. Martin, "Plasmon resonances of silver nanowires with a nonregular cross section," Phys. Rev. B **64**, 235402 (2001).
20. A. Lehmuskero, M. Kuittinen, and P. Vahimaa, "Refractive index and extinction coefficient dependence of thin Al and Ir films on deposition technique and thickness," Opt. Express **15**, 10744–10752 (2007).

1. Introduction

Localized surface plasmons (LSP), also called as particle plasmons, are coherent oscillations of electrons. They are excited in metallic subwavelength nanostructures and are non-propagating, in contrast to the surface plasmon polaritons. [1, 2] At the LSP resonance wavelength a part of an incident light is scattered and absorbed by the metallic nanostructure [3, 4]. The polarization selectivity of LSP depends on the geometry and the orientation of the particle. From the applications, such as polarizing filters point of view, the full absorption would be an ideal situation. Since localized surface plasmon resonance is not capable of producing total absorption into our knowledge, an additional physical mechanism has to be introduced.

Guided-mode resonance is a phenomenon that occurs in waveguide gratings when light couples into waveguide modes that propagate parallel to the grating surface [5]. These modes are also called leaky modes since the light that couples to them is coupled out as well. The guided-mode resonance is known to lead to full reflection [6–8] but as will be demonstrated in this work, it may also lead to almost full absorption and greatly enhance the absorption of LSP resonance.

High extinction (= absorption + scattering) originating from the combined guided-mode and the LSP resonance is not a totally new idea [9]. Also, suppressed extinction based on the double resonance has been reported earlier [10]. However, these studies have concentrated only on the extinction so that the absorption is non-optimized. In this paper we present grating structures that are suitable for high absorption and we discuss the possibility of exploiting the gratings in applications such as polarizing beam splitters and polarizing filters. We also demonstrate that only guided-mode resonance is able to produce almost total absorption and in contrast to the double resonance, the absorption is possible to be optimized for the polarization component that is either parallel or perpendicular to the grating lines.

2. Structure parameters and materials

There are several types of structures that could absorb one polarization component by resonant phenomenon. The first requirement for the structure is that it has metal as an absorptive material. Secondly, the structure has to be subwavelength in order to support only the zeroth propagating diffraction order. In addition, to support guided-wave modes, a dielectric waveguide in connection with metallic structure is required. The simplest structures fulfilling these requirements are one-dimensional wire grid gratings and two-dimensional pilar gratings. In this work we consider linear 1D grating, illustrated in Fig. 1, because it is the easiest structure to

#136219 - $15.00 USD Received 7 Oct 2010; revised 10 Nov 2010; accepted 12 Nov 2010; published 10 Dec 2010

fabricate. The substrate is fused silica SiO_2 and the dielectric part of the grating is titanium dioxide TiO_2. The metal wires are either gold or aluminum depending on the design.

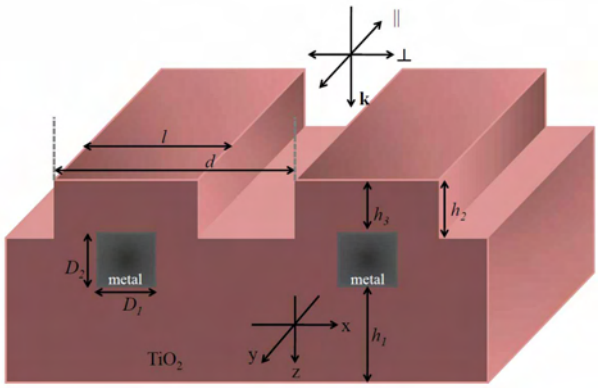

Fig. 1. Absorbing grating geometry. Metal inside TiO_2 is either gold or aluminum. The period of the grating is d, the line width is l, the width and the height of the metal wire are D_1, and D_2, respectively, the height of the bottom TiO_2 layer is h_1, the height of the TiO_2 line is h_2, and the distance between metal wire from the top of the grating is h_3. The parallel ($\|$) polarization indicates light with the electric field in the direction of the y-axis. The perpendicular ($\perp$) polarization indicates light with the electric field in the direction of the x-axis.

The objective in the design was to obtain LSP resonance at the same wavelength with guided-mode resonance because it is assumable that combined resonances would lead to highest absorption. The resonance condition for LSP was approximated from [11]

$$\frac{\Re\{\varepsilon_{\text{metal}}\}}{\varepsilon_{\text{dielectric}}} = -1, \tag{1}$$

which represents the LSP resonance condition for infinitely long cylinder. The parameter $\Re\{\varepsilon_{\text{metal}}\}$ indicates the real part of the permittivity of the cylinder and $\varepsilon_{\text{dielectric}}$ the permittivity of the surrounding medium. The spectral position of the resonance, however, shifts towards the longer wavelengths with increasing particle size [12]. This red-shift occurs also if there are several cylinders close to each other which enables the coupling between the localized modes [13–15].

Three structures for two different wavelengths were optimized. The first structure was optimized for HeNe laser operating at the wavelength of 632.8 nm. The other two structures were designed for the wavelength of 532 nm that corresponds to the wavelength of diode-pumped solid state (DPSS) laser and frequency-doubled Nd:YAG laser.

In the case of the structure that was designed for 632.8 nm, we chose gold as a material for the metal wires because the condition in Eq. (1) is fulfilled at 560 nm which is expected to redshift due to the coupling of the modes. For the other two structures designed for the wavelength 532 nm, we obtained highest absorption for aluminum as a metal.

The optimization was performed by searching the grating parameters that resulted in highest absorbtion for the parallel or the perpendicular component. The parameters obtained in the optimization of the gold grating are $d = 419.3$ nm, $D_1 = D_2 = 94$ nm, $h_1 = 188.7$ nm, $h_2 = 94$ nm, $h_3 = 50.4$ nm, and $l = 194.8$ nm. The two designs containing aluminum are denoted by A and B. The optimized grating parameters for the design A are $d = 244$ nm, $D_1 = 125$ nm, $D_2 = 86$ nm, $h_1 = 84$ nm, $h_2 = D_2 = 86$ nm, $h_3 = 49$ nm, and $l = 223$ nm. The corresponding

#136219 - $15.00 USD Received 7 Oct 2010; revised 10 Nov 2010; accepted 12 Nov 2010; published 10 Dec 2010

parameters for the design B are $d = 312$ nm, $D_1 = 40$ nm, $D_2 = 140$ nm, $h_1 = 34$ nm, $h_2 = 64$ nm, $h_3 = 36$ nm, and $l = 102$ nm. Because a native oxide is formed on aluminum surface when exposed to air, a 15 nm-thick oxide layer on the top of and on the sidewalls of aluminum wire was taken into account in the optimization. The calculations were carried out with Fourier-modal method for 1D grating [16]. The fabrication of the design A is described next before going into Section 4 in which the spectral behavior of the designs are presented.

3. Fabrication of aluminum polarizing filter

The aluminum grating corresponding to the design A was chosen to be fabricated due to its reasonable contrast ratio. The underlaying TiO_2 layer was grown on a 0.09 inches thick fused silica substrate using atomic layer deposition (ALD). Then the substrate was coated with an aluminum layer in high vacuum deposition using electron beam gun. During the same deposition cycle, a thin (about 30 nm) SiO_2 layer was deposited on aluminum. The SiO_2 layer is used as a hard mask for aluminum etching. This has been shown to improve the etched aluminum profile during the aluminum etching [17]. Next, the substrate was coated with an electron beam resist ZEP-7000 and the electron beam exposure was performed with Vistec EBPG 5000+ ES HR. The exposure was followed by the development of the resist layer and reactive ion etching (RIE) of the SiO_2 layer using CHF_3/Ar plasma. The aluminum layer was then etched in BCl_3/Cl based RIE-process using the patterned SiO_2 layer as a hard mask. The remaining resist and the SiO_2 layers were removed in oxygen and CHF_3/Ar plasma, respectively. Finally, the aluminum grating was coated with a TiO_2 layer applying ALD. The scanning electron microscope image from the cross section of the grating is illustrated in Fig. 2.

Fig. 2. Cross section of the absorbing polarization filter corresponding to the design A. The sample was fabricated with electron beam lithography. The metal wires are aluminum and the surrounding material is atomic layer deposited titanium dioxide. The image is taken with scanning electron microscope.

The ALD technique was used in the deposition of the wave guide material because it produces well controlled layer thickness. The precise control of the thickness is important because resonance phenomena are highly dependent on the dimensions of the structure. ALD also produces denser material with higher refractive index than is achieved by, for example, evaporation or sputtering techniques [18]. The higher the refraction index is, the more there exist waveguide modes. Thus, the possibility for light coupling into the waveguide modes increases which allows greater freedom for the design. Moreover, Eq. (1) indicates that for lower refraction in-

#136219 - $15.00 USD Received 7 Oct 2010; revised 10 Nov 2010; accepted 12 Nov 2010; published 10 Dec 2010

dexes the excitation wavelength of localized surface plasmons would shift towards the shorter wavelengths, and thus out of the operation range of the lasers.

4. Spectral behavior near resonances

The absorbance, reflectance, and transmittance spectra for the gold grating are shown in Fig. 3. It can be seen that the absorbance reaches 95 % at the wavelength of 632.8 nm for the perpendicularly polarized light. The parallel polarization is mostly reflected (approximately 42 %) and transmitted (approximately 48 %). The absorption is indeed much higher than reported earlier for localized surface plasmons. Since the absorption of bulk gold near the wavelength of 632.8 nm is 4 %, it is remarkable that only 330 nm thick structure is able to produce such high absorption.

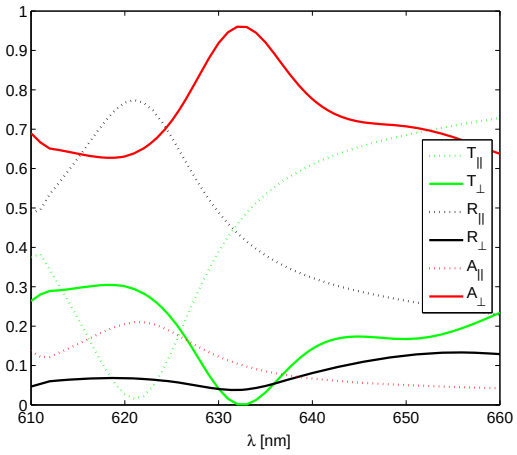

Fig. 3. Absorbance (A), reflectance (R) and transmittance (T) for TiO2 grating with gold wires inside. The absorption peak is located at the wavelength of 632.8 nm. The solid lines indicate the electric field polarized perpendicular to the grating lines and the dashed lines indicate the parallel polarization.

Although it is probable that the absorption mechanism is based on combined guided-mode resonance and LSP resonance, we may analyze the phenomenon in more detail from electric field intensity distributions. The electric field intensity distributions and Poynting vectors inside the gold grating are shown in Figs. 4(a) and 4(b) for the absorbed and split polarizations, respectively. The direction of the Poynting vector represents the direction of the energy flow and the length of the vector represents the strength of the electric field.

When waveguide modes interfere with each other, a periodic pattern of high intensity regions, so-called hotspots, are expected to occur in the x-direction. The hotspots are an indication of a standing wave that is generated when waveguide modes propagate both in the $+x$- and $-x$-directions along the waveguide. The hot spots can indeed be seen in Fig. 4(a) in the TiO_2 layer between gold and the fused silica substrate indicating that the guided-mode resonance really takes place in the structure.

On the other hand, the intensity of the electric field reaches the highest values at the corners and on the sidewalls of the gold wires where the intensity is several times higher than in the surrounding medium. This kind of electric field distribution is related to the excitation of localized surface plasmons [19]. As a reference, the field distribution of the non-absorbed component in

#136219 - $15.00 USD Received 7 Oct 2010; revised 10 Nov 2010; accepted 12 Nov 2010; published 10 Dec 2010

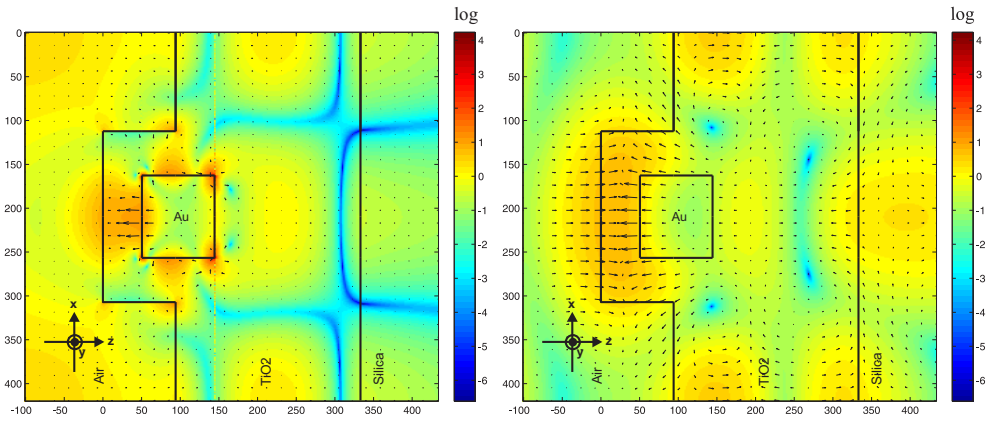

Fig. 4. Intensity distribution and Poynting vectors of the electric field inside the absorbing gold grating. (a) represents the absorbed *x*-component and (b) the partly reflected and partly transmitted *y*-component. The scale is logarithmic.

Fig. 4(b) shows none of the resonant features. The Poynting vectors in Fig. 4(b) show that a part of the light is transmitted and the other part reflected.

Because the light in the gold grating couples into the waveguide modes of the TiO_2 grating, the interaction of light and metal is greater than for naked metal wires. Furthermore, because the metal is surrounded by the waveguide material, light can penetrate into the metal from all sides which leads to high absorption. The period of the structure is sufficiently small compared to the wavelength of light so that only the zeroth order mode is transmitted and reflected. Therefore, the energy is indeed absorbed and not coupled to other diffraction orders.

The theoretical absorbance, reflectance, and transmittance for the aluminum grating designs A and B are shown in Figs. 5(a) and 5(b). The absorbance for the perpendicular polarization for

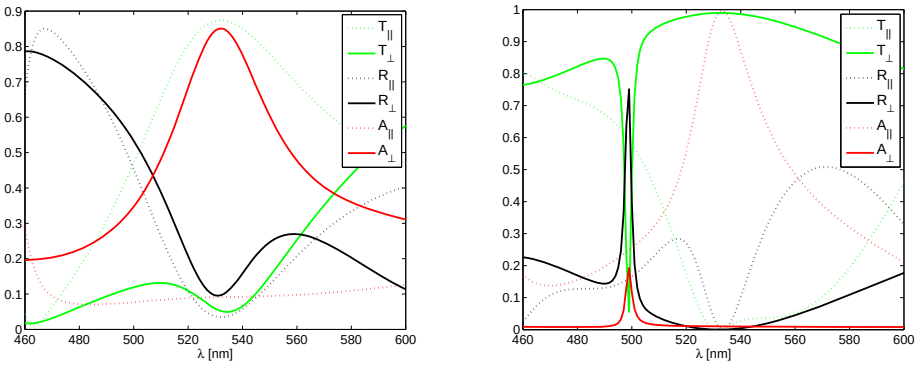

Fig. 5. Reflectance (R), transmittance (T), and absorbance (A) for the perpendicular (solid line) and the parallel component (dashed line) in the case of aluminum gratings. Light is incident at normal angle. (a) represents the design A and the design B. For the design B the contrast $T_\perp/T_\parallel = 6600$ and the absorbance is 99.67 % at the wavelength of 532 nm.

#136219 - $15.00 USD Received 7 Oct 2010; revised 10 Nov 2010; accepted 12 Nov 2010; published 10 Dec 2010

the design A at the wavelength of 532 nm reaches about 85.1 % but now 87.4 % of the parallel polarization is transmitted instead of split into two.

For the design B almost total absorption (99.69 %) is reached together with the contrast of $T_\perp/T_\parallel = 6600$ that corresponds to extinction of $-\ln T_\parallel = 8.8597$. Peculiarly, in this case the parallel electric field component is absorbed instead of the perpendicular component. LSP resonance is excited only by the light with the electric field component normal to the surface. Therefore, the LSP resonance has to be excluded as an absorption mechanism which leads to the conclusion that only guided-mode resonance contributes to the absorption.

Again, we analyzed the field intensity distribution and the Poynting vectors shown in Figs. 6(a) and 6(b) for the absorbed components of the designs A and B, respectively. The peri-

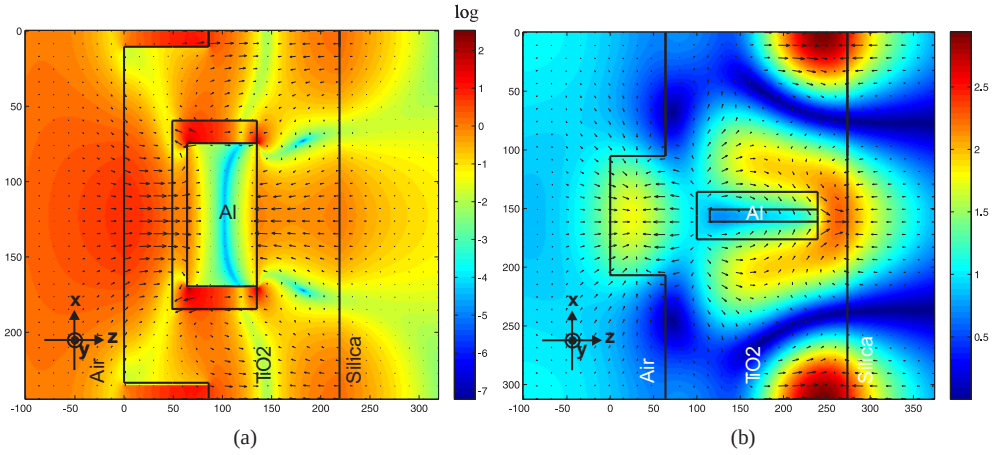

(a) (b)

Fig. 6. Electric field intensities and the Poynting vector distributions for the absorbed components inside one grating period for the designs A (a) and B (b). Light is incident along the z-axis. In (a) the incident light is polarized perpendicularly to the grating lines. In (b) the incident field is polarized parallel to the grating lines. The material on the top of and on the sidewalls of aluminum is aluminum dioxide. The scale is logarithmic.

odic hotspot pattern indicates again the guided-mode resonance in both of the figures. However, the field around the aluminum wires is different from the gold wires. The field is not as strongly localized as in the case of the gold wires. This is of consistent with our conclusion that no LSP resonance is excited in the structure.

The contribution of the guided-mode resonance is most easiest seen if the angle of incidence is oblique because light may propagate either $-x$- or $+x$-direction instead of forming a standing wave, as it does at the normal incidence angle. Figure 7 shows that the energy clearly flows along the waveguide between aluminum and titanium dioxide, when the angle of incidence is 10 deg for the design A. Of course, the grating parameters are slightly altered to obtain the same resonance condition as in the normal incidence case.

The theoretical calculations for the aluminum and gold structures have been conducted by using 771 diffraction orders. However, in the case of the gold grating, even this amount of orders at the resonance wavelength is not enough. The numerical convergence of the absorbance for the perpendicular polarization component in the gold structure at wavelength of 632.8 nm is given in Fig. 8. Even though the convergence is poor, it may be estimated from Fig. 8 that the right value for the absorbance is between 94–98 %.

The slow numerical convergence might be explained by the contribution of evanescent fields caused by LSP resonance. The convergence for the aluminum gratings was good. The different

#136219 - $15.00 USD Received 7 Oct 2010; revised 10 Nov 2010; accepted 12 Nov 2010; published 10 Dec 2010

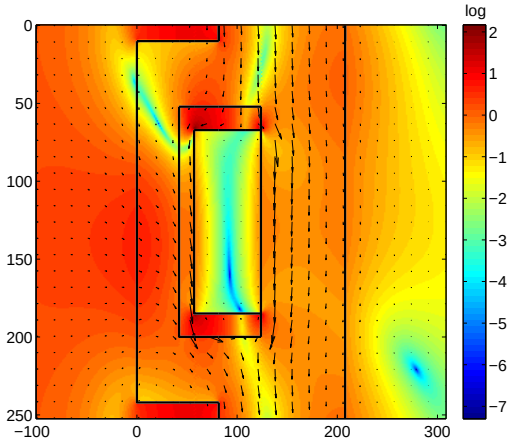

Fig. 7. Electric field intensity and the direction of the energy flow is given for the design A in 10 deg angle of incidence with slightly altered grating parameters. The Poynting vector arrows show clearly that the light is coupled to guided-mode resonance and therefore absorbed.

convergence properties of the structures support the suggestion that for the gold structure the absorption enhancement is contributed by LSPs and for the aluminum gratings only guided-mode resonance is responsible for the absorption. Furthermore, the resonance condition given by Eq. (1) is fulfilled approximately at wavelength of 220 nm for aluminum cylinders. This is several hundreds of nanometers away from the spectral position of the absorption peak.

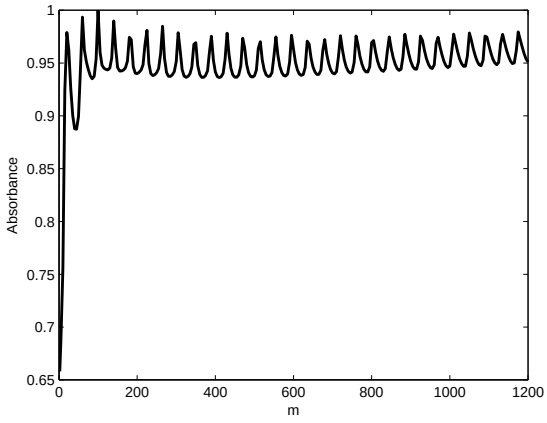

Fig. 8. Convergence of the gold grating for the perpendicular component in absorbance at the resonance wavelength 632.8 nm. The number of the diffraction orders used in the calculations is 2m+1. The poor convergence indicates the excitation of localized surface plasmons.

The resonance phenomenon was verified experimentally by measuring the transmittance of the fabricated aluminum structure for the design A. The measurements were made with variable angle spectroscopic ellipsometer. The theoretical results have been compared to the measured

#136219 - $15.00 USD Received 7 Oct 2010; revised 10 Nov 2010; accepted 12 Nov 2010; published 10 Dec 2010

results in Fig. 9. It may be seen that the theoretical transmittance matches reasonably well with the experimental transmittance. The small differences in the intensity and in the position of the resonance originate probably from porous microstructure of aluminum that might change the refractive index significantly [20]. Also manufactural defects, such as rounding of the rectangular corners, have influence to the performance of the grating.

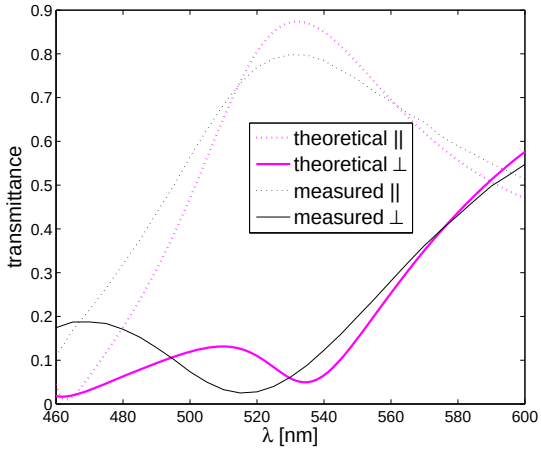

Fig. 9. Experimental (black line) and theoretical (purple line) transmittance for the perpendicular (solid line) and the parallel (dashed line) component for the design A.

Despite the fact that the fabrication did not result in perfect structures, guided-mode resonance solely or combined guided-mode resonance and LSP resonance seem to have potential to be utilized in application purposes. The gold grating behaves as a polarizing beamsplitter by dividing the non-absorbed polarization component into the reflected and transmitted parts. This property could provide an alternative to common beamsplitters that usually divide the beam into two different polarizations.

The aluminum gratings designs A and B work as polarizing filters by transmitting only one polarization component and by absorbing the other component. However, it must be noted that even though the design A could be fabricated, the design B, which has better performance from the applications point of view, is still challenging for fabrication. Anyway, all the absorbing resonant grating designs show potential for applications where low intensity light sources are used. High intensities would lead into the damaging of the absorbing elements.

5. Conclusions

In this work, guided-mode resonance has been demonstrated to lead to almost total absorbtion of either the parallel or the perpendicular field component for linear metal structure embedded in a dielectric waveguide. It was also shown that the guided-mode resonance may significantly enhance the absorbtion of localized surface plasmons.

Three types of absorbing resonance gratings operating at the wavelengths of 632.8 nm or 532 nm were designed. The gold grating resulted in high absorption of the perpendicular polarization component and in division of the parallel component into reflected and transmitted parts. The two aluminum gratings absorbed the parallel or the perpendicular component and transmitted the non-absorbed component.

The behavior of the gold grating was explained by the combination of guided-mode resonance and localized surface plasmons. In case of the aluminum gratings it was concluded that

#136219 - $15.00 USD Received 7 Oct 2010; revised 10 Nov 2010; accepted 12 Nov 2010; published 10 Dec 2010

the only effect leading to the absorption was guided-mode resonance. The reasoning was based on analyzing the field intensity distributions, the direction of the energy flow, and the numerical convergence.

Almost total absorption in structures that have metallic film of thickness of only about 100 nm is theoretically interesting phenomenon by itself. In addition, the structures also showed potential to be used as filters and beamsplitters for low-intensity application purposes. Especially the gratings where the absorption mechanism was based solely on guided-mode resonance show flexibility of use due to the possibility to choose whether the parallel or the perpendicular polarization is filtered out.

Acknowledgment

This work was supported by the Finnish Graduate School of Modern Optics and Photonics. Prof. Jari Turunen is acknowledged for his insight into the subject.

#136219 - $15.00 USD Received 7 Oct 2010; revised 10 Nov 2010; accepted 12 Nov 2010; published 10 Dec 2010

Paper **V**

B. Bai, J. Laukkanen,
A. Lehmuskero, and J. Turunen
”Simultaneously enhanced
transmission and artificial optical
activity in gold film perforated
with chiral hole array”
Physical Review B,
81, pp. 115424, 2010.

V B. Bai, J. Laukkanen, A. Lehmuskero, and J. Turunen, “Simultaneously enhanced transmission and artificial optical activity in gold film perforated with chiral hole array,” *Phys. Rev. B*, 81, 115424 (2010).

Simultaneously enhanced transmission and artificial optical activity in gold film perforated with chiral hole array

Benfeng Bai,[1,2,3,*] Janne Laukkanen,[1] Anni Lehmuskero,[1] and Jari Turunen[1]
[1]*Department of Physics and Mathematics, University of Eastern Finland (Joensuu Campus), P.O. Box 111, FI-80101 Joensuu, Finland*
[2]*State Key Laboratory of Precision Measurement Technology and Instruments, Department of Precision Instruments, Tsinghua University, Beijing 100084, China*
[3]*Tsinghua-Foxconn Nanotechnology Research Center, Tsinghua University, Beijing 100084, China*
(Received 21 October 2009; revised manuscript received 17 February 2010; published 15 March 2010)

We propose a simple two-dimensional metallic periodic chiral structure (PCS) consisting of a dielectric substrate and a thin gold film perforated with gammadion-shaped chiral hole array, in which the transmittance and artificial optical activity can be simultaneously enhanced. The principle and optical performance of the PCS are demonstrated through the experimental realization of a PCS sample, from numerical design, fabrication, to optical characterization. Good agreement between theory and experiment has been obtained. The PCS sample shows an enhanced transmittance of 53% at wavelength 1168 nm, accompanied nearby by a polarization rotation peak with the effective specific rotatory power up to 10^5 deg/mm. The enhancement mechanism of the dual effect is thoroughly studied by investigating the optical anomalies (i.e., Rayleigh anomalies, surface plasmon polaritons, and localized surface plasmons) in the PCS and their roles in the light-matter interaction. Several light-anomaly coupling regimes have been revealed. The single-layer metallic PCS is relatively easy to realize in optical frequencies by using mature microfabrication techniques such as electron-beam lithography and lift-off technique. The physical insight into the enhancement mechanism provides guidelines to develop more complicated PCS, such as multilayer PCS with metal and dielectric inclusions, which can produce stronger optical activity and better optical performance.

DOI: 10.1103/PhysRevB.81.115424 PACS number(s): 78.20.Ek, 73.20.Mf, 42.79.Dj, 42.25.Ja

I. INTRODUCTION

The artificially induced optical activity and circular dichroism in two-dimensional (2D) (Refs. 1–7) and three-dimensional (3D) (Refs. 8–13) periodic chiral structures (PCS) have been intensively studied in recent years. Such structures usually are composed of common optical materials (such as metals and dielectrics) without optical activity; however, due to their chiral structural features that resemble the molecular or crystalline chirality in natural chiral media (such as sucrose solution and quartz, respectively), optical activity can also be produced in PCS and may be further enhanced by various electromagnetic resonances. For example, giant polarization rotatory power (several orders larger than that in natural chiral media) (Refs. 1, 8, and 9) and tens-of-degree polarization rotation[6] have been observed in the zero-order transmission in some previously investigated PCS.

The PCS differ from traditional periodic polarizing elements such as wire grid polarizers[14,15] and film stacks[16] in the sense that the polarization conversion in PCS is realized via *circular form birefringence/dichroism* where left-circularly polarized (LCP) and right-circularly polarized (RCP) waves are eigenpolarizations of the structures;[17] in contrast, traditional grating polarizers[14–16] achieve the polarizing effect via *linear form birefringence* where two mutually orthogonal linearly polarized waves are eigenpolarizations. Owing to this new principle, the PCS have two distinct characteristics/advantages over traditional polarizing elements. First, unlike some linear grating polarizers that should work under *oblique* or *conical* illumination mountings,[18,19] the PCS can produce large polarization conversion under *normal* incidence.[17] Second, due to circular birefringence, the polarization conversion output in the PCS does not depend on the initial polarization direction of incident light, i.e., there is no need to align the incident polarization orientation in application. These characteristics are obviously more convenient and favorable from an application point of view. In addition, the PCS have some other peculiar polarizing properties, such as the reciprocity of the polarizing effect and no polarization conversion in reflection.[17] All of these features make PCS promising candidates to be developed as novel-type compact polarizing elements that can be used in, e.g., integrated electro-optic systems.

The light-matter interaction in PCS, from an effective-medium point of view, can be described by the classical constitutive equation of chiral media[20]

$$\mathbf{D} = \epsilon\mathbf{E} + i\xi\mathbf{k} \times \mathbf{E}, \tag{1}$$

where ϵ is the unperturbed (achiral) permittivity tensor of the effective medium, $\mathbf{k}$ is the wave vector, and ξ is known as the gyratory coefficient. Therefore, to achieve large optical activity in PCS, an intuitive idea is to increase the gyratory coefficient ξ as much as possible by properly designing the PCS with high chirality. Extending 2D PCS to 3D or quasi-3D designs[8–13] is one such attempt. However, 3D PCS usually impose many challenges and difficulties to the fabrication process due to the increased structural complexity. This is why most 3D PCS realized so far work in microwave[8,13] and far infrared domain.[12] To reach visible and near-infrared domain, the period of PCS should be small enough compared with the corresponding operation wavelength. Therefore, it is always preferred if large optical ac-

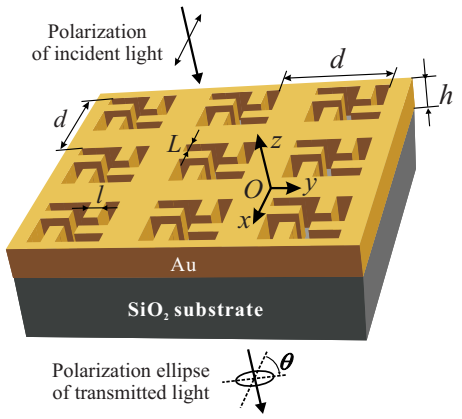

FIG. 1. (Color online) Geometry of the PCS with a gold film perforated with gammadion-shaped hole array on a fused silica substrate.

tivity can be achieved in simple 2D PCS, which can be manufactured relatively easily with mature microfabrication techniques such as electron-beam lithography.

In 2D PCS, although the maximization of chirality factor ξ is limited, the optical activity can nevertheless be enhanced by various optical resonances in *subwavelength* PCS (whose period d is comparable with or smaller than the wavelength λ). It has been revealed that surface-plasmon resonance (SPR) in metallic PCS (Refs. 1–5) as well as the guided-mode resonance and Fabry-Pérot resonance in dielectric PCS (Ref. 7) can contribute to the enhancement of optical activity. However, the large transmission loss in previous PCS is a major defect that dims their application prospect. Metallic PCS suffer from serious absorption at resonance due to the dissipation of energy in surface-plasmon polaritons (SPPs) (Refs. 1, 4, 8, and 13) while dielectric PCS often get suppressed transmission at guided-mode resonance.[6,7] Therefore, it has been a vital issue and main objective in the development of PCS to produce simultaneously large optical activity and high transmittance.

The extraordinary transmission effect in perforated[21] or corrugated[22] metallic films has been well known for several years. Although there is still debate on the physical mechanism of enhancement,[23–26] it is commonly admitted that surface plasmons, including SPP Bloch waves on a periodic metal surface and localized surface plasmons (LSPs) excited in metallic particles or voids, play a crucial role in mediating the light transmission.[26] According to our previous study,[7,17] a key factor of producing large optical activity in PCS is to provide a channel for the incident light to be efficiently coupled to some surface or guided modes in the PCS, so that the LCP and RCP components may experience different coupling strength and phase change. Since both the extraordinary transmission and artificial optical activity may be related to surface plasmons, it is natural to consider synchronous realization of the two effects.

In this work, we propose a metallic PCS composed of a fused silica substrate covered by a gold film perforated with gammadion-shaped chiral hole array, as shown in Fig. 1. As an inductive structure, it is complementary compared with most previous 2D and quasi-3D metallic PCS structures[1–5,8,9,13] that usually take the form of arrays of isolated chiral metal particles. Such particle type, or capacitive, PCS are not necessarily efficient geometries to excite and sustain propagating SPP modes for lack of connected metal surface. Although the LSPs on particles can be excited, they are less efficient than the propagating modes to accumulate phase difference between the LCP and RCP components during their propagation and, on the other hand, increase the dissipation of electromagnetic energy. Therefore, with the hole-type PCS, we expect to achieve the enhanced dual effect via the efficiently excited SPPs.

The paper is organized as follows. In Sec. II, we present the experimental realization of a hole-type PCS with simultaneously enhanced transmission and optical activity, from numerical design and fabrication to optical characterization. Then, in Sec. III, the enhancement mechanism of the dual effect is thoroughly studied by investigating the optical anomalies in the PCS as well as their interaction with the incident light. Several light-anomaly coupling regimes are revealed. In Sec. IV, the measures for optimizing the enhanced dual effect are discussed and the simulation results of an optimized case is demonstrated. Section V summarizes the work.

II. EXPERIMENTAL REALIZATION OF A PCS WITH DUAL EFFECT

A. Numerical design

The optical response of the PCS is rigorously simulated with the Fourier modal method (FMM) for crossed gratings with fourfold rotational (C_4) symmetry,[27] which is based on rigorous electromagnetic theory of gratings and is an optimization of the standard FMM (Ref. 28) by using a group-theoretic approach.[29] The method first Fourier factorizes both the electromagnetic field and the periodic permittivity function of the grating media such that the Maxwell's equations are transformed into the discretized Fourier space; then by solving an eigenvalue problem in the grating layer and matching the boundary conditions at interfaces between different spatial regions, the fields inside and outside the modulated region can be readily solved. The reformulated FMM is specially developed for modeling C_4 symmetric crossed gratings with faster computation speed and better convergence, and is therefore most suitable for the study of our PCS.

A linearly polarized plane wave is assumed to illuminate the PCS at normal incidence with its polarization direction arbitrarily mounted. After the interaction with the PCS, the directly transmitted light (i.e., the zeroth diffraction order of the grating) usually becomes elliptically polarized. The polarization change is described by a polarization rotation angle θ (the angle between the major semiaxis of the polarization ellipse and the incident polarization direction, as shown in Fig. 1) and an ellipticity angle χ (which is defined by $\tan\chi$ as the minor-to-major-axis ratio of the polarization ellipse).[30]

We choose gold as the metal film material for the efficient excitation of SPPs in optical frequencies. The gold refractive index used in simulation was measured by ellipsometry on a 100-nm-thick homemade gold film, as the refractive index of

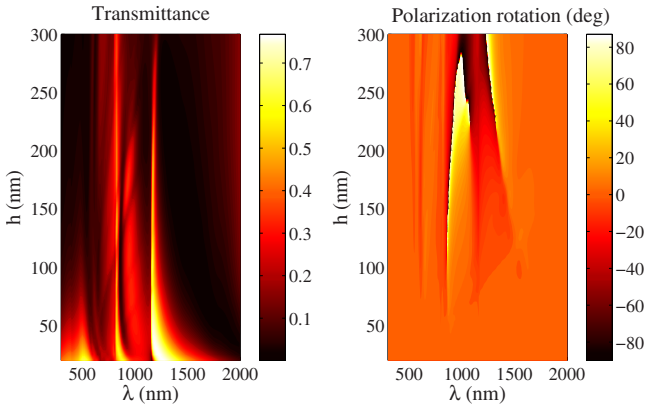

FIG. 2. (Color online) Numerically calculated transmittance and polarization rotation angle θ of the directly transmitted light in the PCS with respect to wavelength λ and film thickness h.

a thin metal film can be considerably different from that of bulk metal.[31] It is crucial for the generation of optical activity in 2D PCS that the cover and substrate materials are different.[17] Taking into account the feasibility of fabrication, we design the PCS with period $d=800$ nm and the gammadion dimensions $L=l=120$ nm. Then the only structural parameter to be optimized is the film thickness h.

Figure 2 shows the simulated transmittance and polarization rotation angle θ of the directly transmitted light with respect to the wavelength λ and film thickness h. It is seen that there are two main branches of polarization rotation maxima (one around wavelength 850 nm and the other around 1150 nm) corresponding to the vicinities of two transmittance maxima that should be attributed to the excitation of SPPs on the upper (air-gold) and lower (gold-silica) interfaces (the physical mechanism will be analyzed in detail in Sec. III). Furthermore, one can see that when the film thickness is beyond a certain limit (say, $h>80$ nm), tens-of-degree polarization rotation accompanied by an enhanced transmission over 50% may be realized in the PCS. This is a practical guideline to the fabrication.

B. Sample fabrication

We have fabricated our first samples by using electron-beam lithography and lift-off technique. First, a 1″ fused silica wafer was spin coated with PMMA resist, which was then patterned with a Vistec EBPG5000+ES HR electron-beam patterning tool. After exposure, the resist was developed in methyl iso-butyl ketone:isopropanol 1:2 solution and rinsed in isopropanol. Then, after an adhesion layer of 3-nm-thick chromium was sputtered on the sample, an 80-nm-thick gold layer was deposited by thermal evaporation. Finally, the remaining resist as well as the metal on top of it was removed in acetone.

Due to the limitation of the lift-off technique, the maximum gold film thickness that we can achieve is around 80 nm. Figure 3 shows the scanning electron microscope (SEM) image of a fabricated PCS sample with left-twisted gammadion pattern, whose parameters are $d=800$ nm, $h=80$ nm, $L=108$ nm, and $l=127$ nm.

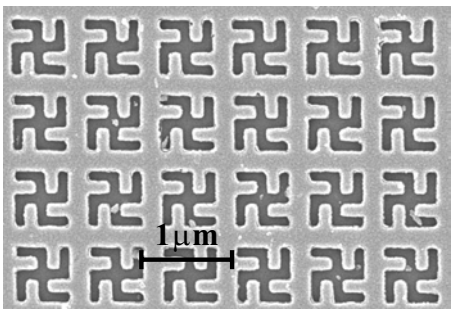

FIG. 3. Top-view SEM image of a fabricated PCS sample.

C. Optical characterization

The optical properties of the PCS sample were characterized by ellipsometry. We employed a variable angle spectroscopic ellipsometer VASE produced by J. A. Woollam Co. to measure the transmittance and polarization state of the transmitted light under normal incidence in the wavelength range 300–1500 nm.

In the polarization measurement, the ellipsometer outputs ψ and δ that are defined by

$$\frac{t_p}{t_s} = \tan\psi \exp(i\delta), \tag{2}$$

where t_p and t_s are the complex transmission coefficients of two mutually orthogonal linearly polarized components. Note that the orientation of the s-p coordinate system can be arbitrary with respect to the Oxy system (with the x and y axes along the two periodic directions) due to the circular birefringence in the PCS, which simplifies the alignment of the sample. The above measurement actually corresponds to the case that a linearly polarized light is incident with its polarization direction parallel to the main diagonal of the s-p coordinate system. Therefore, the polarization rotation angle θ (with the clockwise rotation defined as the positive sense) of the transmitted light can be derived from[30]

$$\tan[2(45^\circ - \theta)] = \tan 2\psi \cos\delta. \tag{3}$$

After the full dispersion spectrum of θ is obtained, the spectrum of the ellipticity angle χ can be easily calculated numerically by Kramers-Kronig transformation.[32,33]

Figure 4 shows the obtained measurement results of the transmittance and polarization spectra of the PCS sample, compared with the theoretical counterparts calculated with the practical structural parameters. We can see very good agreement between them. The small discrepancies are probably due to structure imperfections, surface roughness, and the uncertainty of the measured structural dimensions. Note that the abrupt change around $\lambda=1050$ nm in the measured transmittance curve is caused by the change in detectors in the ellipsometer; it is not a physical effect.

In the spectra there are two main transmission peaks around wavelengths 824 and 1168 nm, which are related to the excitation of SPPs on the air-gold and gold-silica interfaces, respectively (the detailed analysis is given in Sec. III). In the vicinity of each resonance, the polarization conversion effect (including the polarization rotation and elliptization) is

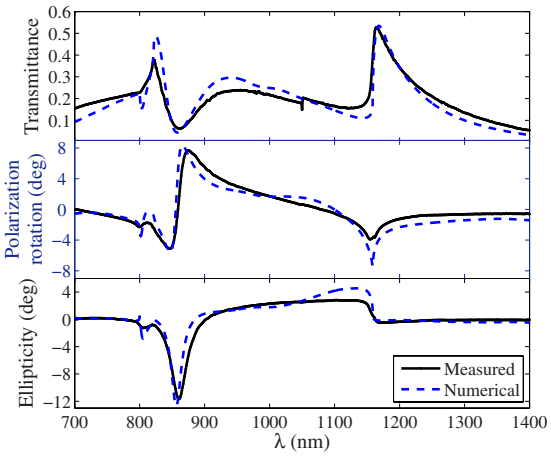

FIG. 4. (Color online) Experimentally measured and numerically calculated transmittance and polarization spectra of the PCS sample under normal incidence.

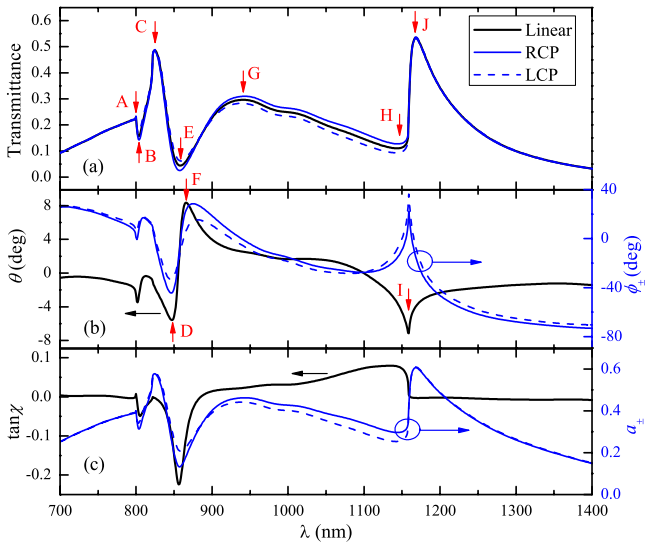

FIG. 5. (Color online) Calculated transmittance and polarization spectra of the PCS sample for the linearly polarized illuminating light as well as its LCP and RCP components. (a) Transmittance. (b) Polarization rotation angle θ and the phases $\phi_{\pm}$ of $t_{\pm}$. (c) Ellipticity tan χ and the amplitudes $a_{\pm}$ of $t_{\pm}$. The vertical arrows with letters indicate several characteristic points on the spectra. The horizontal arrows in (b) and (c) indicate whether left or right scales should be considered.

enhanced likewise. Especially, around 1168 nm, a large polarization rotation (about 8° in theory and 4° in measurement) is observed nearby the transmittance peak of 53%, which is an unambiguous manifestation of the expected simultaneously enhanced dual effect. The corresponding *effective specific rotatory power* (i.e., the polarization rotation angle per unit thickness of the chiral film) reaches 10^5 deg/mm, which is one or two orders larger than that of previously reported particle-type 2D metallic PCS working in the visible and near-infrared spectral range[1,9] and is several orders larger than that of natural chiral media (such as quartz, cinnabar, and liquid crystals, whose specific rotatory power is 20 deg/mm, 600 deg/mm, and 10^3 deg/mm, respectively[34]). However, around wavelengths 847–866 nm the enhanced polarization rotation (whose peak value is about 8° in both theory and experiment) is shifted away from the spectral position of the transmission peak and corresponds to a transmittance minimum. This means that the enhanced polarization effect may be accompanied by either an *enhanced* or *suppressed* transmission. Therefore, the underlying physical mechanism must be thoroughly studied to reveal how to achieve and improve the simultaneously enhanced dual effect.

III. ENHANCEMENT MECHANISM

A. Circular birefringence in the PCS

To investigate the light-matter interaction in the PCS, we should first ascertain the eigenpolarizations of the proposed PCS under normal incidence. This can be done by using, e.g., Jones matrix calculus.[30] For directly transmitted light, the Jones vector describing its polarization state can be represented by the multiplication of a 2×2 Jones matrix (representing the polarizing component) and the Jones vector of the incident light,

$$\begin{pmatrix} E_x^{\text{out}} \\ E_y^{\text{out}} \end{pmatrix} = \begin{pmatrix} T_{11} & T_{12} \\ T_{21} & T_{22} \end{pmatrix} \begin{pmatrix} E_x^{\text{in}} \\ E_y^{\text{in}} \end{pmatrix}. \tag{4}$$

The number of independent elements of the Jones matrix is solely determined by the symmetry of the system (including both the structure and the incident mounting). For the PCS with C_4 symmetry under normal incidence, symmetry considerations show that $T_{11}=T_{22}$ and $T_{12}=-T_{21}$. Therefore, the eigenvalues of the Jones matrix can be solved as $T_{11}\pm iT_{12}$ and the corresponding eigenvectors are $(1,\pm i)$, which represent the RCP and LCP waves. This means that the RCP and LCP waves go through the PCS with only the change in their phases and amplitudes (scaled by the eigenvalues) while the polarization states are maintained. Therefore, circular birefringence indeed takes place in the PCS.

If we define the complex transmission coefficients of the RCP (+) and LCP (−) waves as $t_{\pm}=a_{\pm}\exp(i\phi_{\pm})$, then the polarization rotation angle θ and the ellipticity angle χ can be derived as

$$\theta=\frac{1}{2}(\phi_+-\phi_-), \quad \tan\chi=\frac{a_+-a_-}{a_++a_-}. \tag{5}$$

Henceforth, to study the generation and enhancement of the optical activity, it suffices to explore how the LCP and RCP waves are coupled to and interact with the optical modes in the PCS, during which the field amplitudes are changed and the phase difference is accumulated.

Since the numerical modeling reflects reality rather well, as seen from Fig. 4, we will perform the succedent investigation mainly by numerical simulation. Figure 5 shows the calculated spectra of the PCS sample under the illumination of a linearly polarized light as well as its LCP and RCP components. It is clearly seen from Figs. 5(b) and 5(c) that the circular birefringence relations given by Eq. (5) are well satisfied. In Fig. 5, we mark by vertical arrows and letters A–J several wavelengths of interest, where abnormal

changes (anomalies) are observed in both or either of the transmittance and polarization spectra. We proceed to analyze in detail the physical mechanisms behind these anomalies.

B. Optical anomalies in the metallic PCS

Optical anomalies in diffraction gratings, also known as Wood's anomalies, refer to rapid variations in the intensity spectra of various diffraction orders in certain narrow spectral bands. According to the classification by Hessel and Oliner,[35] there are two types of anomalies: *Rayleigh anomalies* (RAs), which often appear as abrupt turning points in spectra due to the onset or disappearance of particular diffraction orders, and *resonance anomalies*, which are smoother spectral variations and arise due to the excitation of certain surface or guided waves. The SPR in the metallic PCS is a resonance anomaly due to the excitation of SPP waves. Furthermore, according to Loewen and Popov,[36] there are the third-type anomalies, called *nonresonance anomalies*, which refer to the other nonresonant effects such as Littrow mounting zeros and Bragg anomalies. The LSPs in the gammadion holes of the metallic PCS can contribute to such anomalies because the LSPs can be excited in a wide spectral range without resonance (which will be shown later).

The metallic hole-type PCS can maintain all the above-mentioned three types of anomalies. Since the anomalies significantly affect the diffraction pattern, energy transportation, and field distribution in the PCS, we must distinguish these anomalies so as to identify different light coupling channels and regimes. Often anomalies of different types overlap with each other, making them difficult to distinguish, especially from the normal-incidence spectra where there are degeneracies of modes. Therefore, we should calculate the angle-resolved transmission spectra to lift up the mode degeneracy. In the following calculation, the incident direction of light is varied only in the Oxz plane with an incident angle α (the angle between the incident wave vector $\mathbf{k}^{\text{in}}$ and the z axis).

The condition for the occurrence of RA corresponding to the cutoff of the (p,q)th diffraction order is

$$|\mathbf{k}_{\parallel}^{\text{in}} + pK\hat{\mathbf{x}} + qK\hat{\mathbf{y}}| = nk_0, \tag{6}$$

where $\mathbf{k}_{\parallel}^{\text{in}}$ is the projection of the incident wave vector on the Oxy plane, $K=2\pi/d$, $\hat{\mathbf{x}}$ and $\hat{\mathbf{y}}$ are unit vectors in the two periodic directions, $k_0=2\pi/\lambda$ is the wave number in vacuum, and n is the refractive index of the cover or substrate medium. For the case of incidence in the Oxz plane, Eq. (6) is specified as

$$\left(\frac{\sin\alpha}{\lambda} + \frac{p}{d}\right)^2 + \frac{q^2}{d^2} = \frac{n^2}{\lambda^2}. \tag{7}$$

Similarly, by replacing the right-hand side of Eq. (6) with the modulus of the SPP wave vector on a *smooth* metal surface, we can obtain the approximate dispersion relation of the (p,q)th-order SPP Bloch wave excited on the *periodic* metal surface as

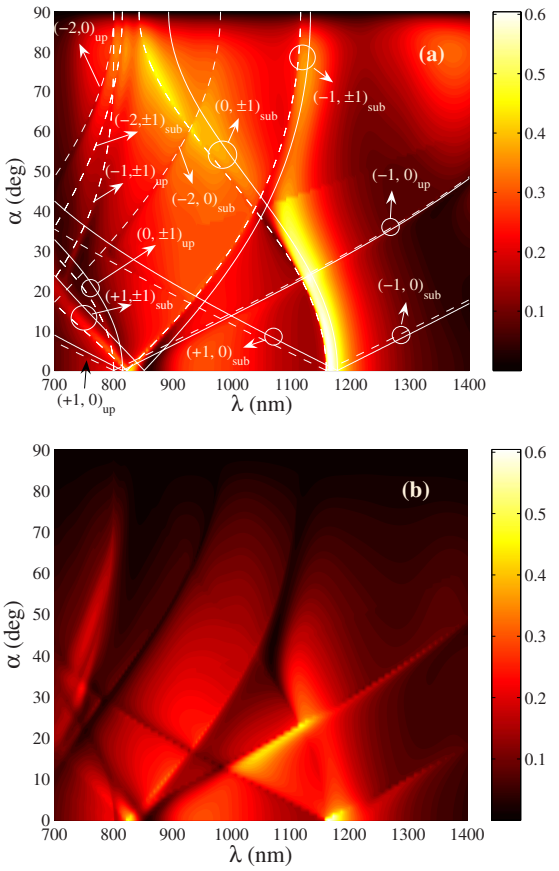

FIG. 6. (Color online) Calculated transmittance of the PCS sample with respect to the change of illumination wavelength λ and incident angle α for the (a) TM and (b) TE incident cases. The dashed and solid lines in (a) are the dispersion curves of RAs and SPP Bloch waves of various orders, calculated with Eqs. (7) and (8), respectively. Only the SPP modes with order indices $|p|,|q| \leq 1$ are demonstrated. The texts "up" and "sub" indicate the modes on the upper (air-gold) and substrate (gold-silica) interfaces, respectively.

$$\left(\frac{\sin\alpha}{\lambda} + \frac{p}{d}\right)^2 + \frac{q^2}{d^2} = \frac{1}{\lambda^2}\frac{\epsilon_m\epsilon_d}{\epsilon_m+\epsilon_d}, \tag{8}$$

where ϵ_m and ϵ_d are the permittivities of the metal and the adjacent dielectric. Note that, while Eq. (7) is accurate and is independent on the metal, Eq. (8) is an approximate relation determined by both the metallic and dielectric properties. Thus Eq. (8) is valid only for slightly modulated metal surfaces and ignores the coupling of SPPs on the upper and lower interfaces of the thin metal film. Nevertheless, we can still use it as a reference to help identify the SPP modes.

Figure 6 shows the calculated transmittance spectra of the PCS sample with respect to the change in illumination wavelength λ and incident angle α. Two polarization cases are investigated: the TM case with the magnetic field vector of the incident wave perpendicular to the incident plane (i.e., the plane containing the incident wave vector and the grating normal) and the TE case with the electric field vector perpendicular to the incident plane. To help distinguish the anomalies, we also plot in Fig. 6(a) the dispersion curves of

RAs (dashed lines) and SPPs (solid lines) of various orders, which are calculated analytically with Eqs. (7) and (8), respectively. We can see clearly the signatures of *all* RAs in both the TM and TE cases, where the numerical and analytical RA traces are exactly superposed with each other. The SPP dispersion curves, though approximate, show qualitatively the spectral positions of the SPRs, which are always redshifted a bit with respect to the corresponding RAs.

The traces of SPP modes are not visible for all orders in the transmittance spectra. This is reasonable because only some low-order SPP Bloch modes can be efficiently excited on a metal grating surface,[26] which sometimes even lead to suppressed transmission.[23,25] In Fig. 6, at non-normal incidence, only one enhanced transmission peak is evident around wavelengths 1100–1170 nm in the TM case, which is related to the excitation of the $(0,\pm 1)_{\mathrm{sub}}$ SPP modes; at normal incidence, however, the SPP modes of same orders (propagating in different directions) degenerate, leading to stronger SPP excitation on both the upper and substrate interfaces around wavelengths 824 nm and 1168 nm, respectively. To exactly identify the SPPs (especially, to distinguish the cavity LSPs in the gammadion holes and the SPPs on the grating surface, both of which may contribute to the enhanced transmission), the far-field transmittance spectra are not sufficient. Thus the characteristic near-field distribution and energy flow must be inspected.

We have calculated the distribution of the electric field components $E_{\parallel} \equiv (E_x^2 + E_y^2)^{1/2}$ and E_z as well as the energy flow on both the upper (air-gold) and substrate (gold-silica) interfaces of the PCS sample at normal incidence. The planes of calculation were selected 20 nm above the respective interfaces in the dielectric side, so that the near-field features of SPPs can be best presented. The energy flow is obtained by calculating the time-averaged Poynting vector $\langle \mathbf{S} \rangle = \frac{1}{2}\mathrm{Re}(\mathbf{E} \times \mathbf{H}^*)$. Except for the RAs, we calculated at each wavelength of the interesting points indicated in Fig. 5(a) for RCP and LCP illuminations so as to intuitively observe the different light-anomaly interactions and to distinguish between the LSPs and SPPs.

As an example, Fig. 7 shows the near-field plots of the PCS under RCP and LCP illuminations at $\lambda = 1168$ nm corresponding to point J in Fig. 5(a). We can see unambiguously the following features. At the air-gold interface, the field is mostly localized in the gammadion holes with the $E_{\parallel}$ component dominant and the energy flowing longitudinally into the holes, showing the characteristics of cavity LSPs. Whereas, at the gold-silica interface, the field is primarily localized on the open continuous metal surface with the E_z component much stronger than the in-plane component $E_{\parallel}$; meanwhile, the $\langle \mathbf{S} \rangle$ vector has a dominant in-plane component, meaning that the energy flows along the metal surface in the xy plane. All of these reveal the presence of SPPs on the substrate interface. The energy flow forms vortices on the metal surface, as a result of the interference of the $\mathrm{SPP}_{\mathrm{sub}}^{(\pm 1,0)}$ and $\mathrm{SPP}_{\mathrm{sub}}^{(0,\pm 1)}$ modes. Therefore, we can conclude that at $\lambda = 1168$ nm there is a hybrid of SPPs and LSPs while the SPPs are dominant. This is consistent with the estimated SPP excitation wavelength $\lambda = 1178$ nm predicted according to Eq. (8) and the dispersion curve in Fig. 6.

Furthermore, by comparing the fields of RCP and LCP cases in Fig. 7, we can see that they have similar field features (field localization, energy flow, etc.), meaning that the dominant anomalies are the same. However, due to the different interactions of the RCP and LCP waves with the chiral structure, the anomalies affect the coupling of RCP and LCP waves differently, manifested in the energy flow and coupling strength. For example, under the RCP and LCP illuminations, the directions of energy flow vortices on the substrate interfaces are opposite and the enhancement factors of the E_z field amplitude are 6.80 and 7.45, respectively. These lead to the accumulated phase difference (circular birefringence) and/or amplitude difference (circular dichroism) of the RCP and LCP waves, as observed in Figs. 5(b) and 5(c).

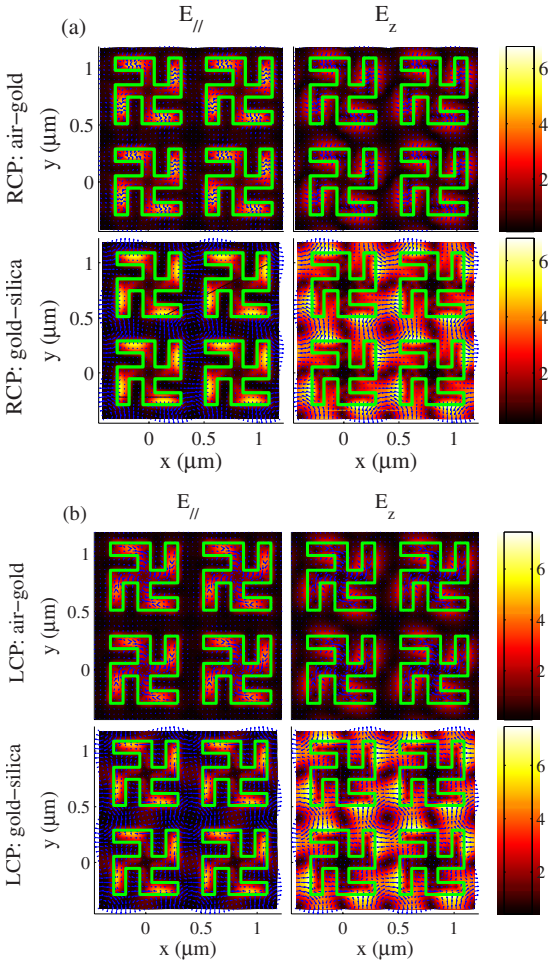

FIG. 7. (Color online) Distribution of the amplitudes of $E_{\parallel}$ and E_z (color plot, in the unit of the incident field amplitude) and the energy flow (arrows with the arrow length proportional to the magnitude of the time-averaged Poynting vector) on the air-gold and gold-silica interfaces under the normal incidence of (a) RCP and (b) LCP waves at $\lambda = 1168$ nm.

Similarly, we can ascertain all the dominant anomalies at points A–J indicated in Fig. 5. Since at each wavelength the basic near-field features of the RCP and LCP cases are similar except for the energy flow direction and field coupling strengths, we show in Figs. 8–11 only the near-field distributions for the RCP incidence case at several typical wavelength points B (802 nm), C (824 nm), E (858 nm), and G (941 nm). At point B (Fig. 8), the SPP excitation on the air-gold surface is evident, corresponding to the $\mathrm{SPP}_{\mathrm{up}}^{(\pm 1,0)}$

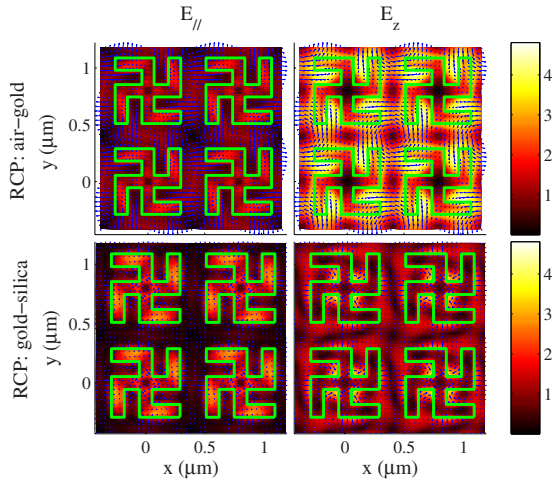

FIG. 8. (Color online) Similar to Fig. 7 but for RCP case at λ =802 nm.

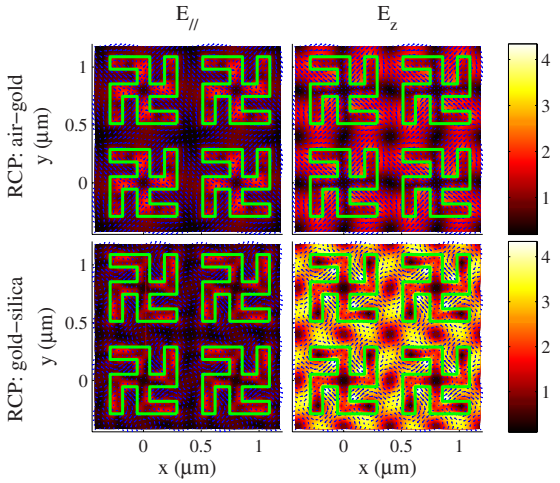

FIG. 10. (Color online) Similar to Fig. 7 but for RCP case at λ=858 nm.

and $SPP_{up}^{(0,\pm1)}$ modes. At point C (Fig. 9), the cavity LSPs in gammadion holes are dominant, although the SPPs on the gold-silica interface are still present and couple with the LSPs. At point E (Fig. 10), the $SPP_{sub}^{(\pm1,\pm1)}$ modes are excited, whose interference pattern and energy flow are intrinsically different from those of the $(\pm1,0)$ and $(0,\pm1)$ order SPPs as shown in Fig. 7. At point G (Fig. 11), we can see that at both the air-gold and gold-silica interfaces the cavity LSPs are dominant, although the impact of SPPs does not totally disappear. In this way, we can characterize the dominant anomalies at all the indicated points, with the results summarized in Table I.

C. Light-anomaly coupling regimes

According to the far-field and near-field features summarized in Table I, we can uncover the light coupling characteristics in the PCS. First, all the RAs, SPPs, and LSPs can serve as efficient coupling channels for the RCP and LCP waves. The light coupling with SPPs and LSPs is intuitive because SPPs and LSPs are localized surface waves or modes on the metal-dielectric interface which can exchange energy with the incident electromagnetic field. The RAs, though not any surface or guided modes, control the opening or closing of the diffraction channels of certain propagating orders, which lead to abrupt redistribution of electromagnetic energy in all other diffraction orders; thereby, the coupling performance of the incident light can still be significantly affected.

Second, the SPPs may lead to enhanced (at point J) as well as suppressed (at points B and E) transmission. However, they always contribute to the polarization effect positively. For example, at point B, the circular birefringence (and thereby the polarization rotation angle θ) is maximized; at point E, the circular dichroism (and thereby the ellipticity χ) is maximized. At point J, although χ is locally minimized, it induces a θ peak nearby due to the fact that θ and χ obey the Kramers-Kronig relations. Also, thanks to the Kramers-Kronig relations, it is seen that the θ peak/zero usually corresponds to a χ zero/peak at strong resonances (see, e.g.,

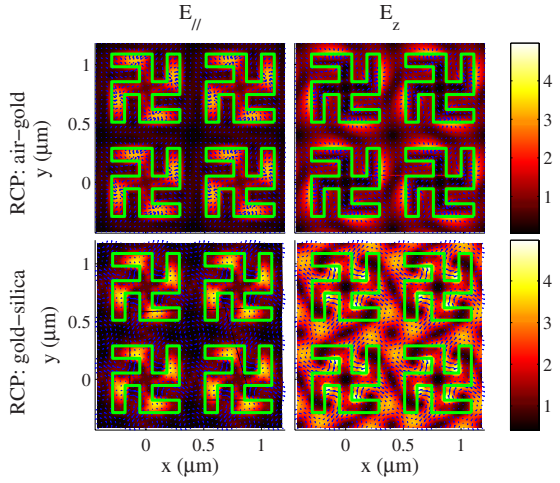

FIG. 9. (Color online) Similar to Fig. 7 but for RCP case at λ =824 nm.

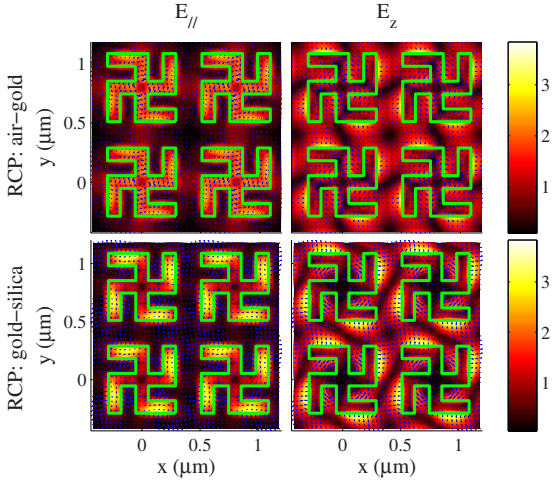

FIG. 11. (Color online) Similar to Fig. 7 but for RCP case at λ=941 nm.

TABLE I. Characteristics of the points indicated in the spectra of Fig. 5.

Point	λ (nm)	T (%)	θ (deg)	χ (deg)	Spectral feature[a]	Dominant anomalies[b]
A	800	23.0	−2.51	0.44	T peak, χ peak	$RA_{up}^{(\pm1,0)}$, $RA_{up}^{(0,\pm1)}$
B	802	16.5	−3.49	−1.39	T dip, θ peak	$SPP_{up}^{(\pm1,0)}$, $SPP_{up}^{(0,\pm1)}$
C	824	46.8	−1.01	0.00	T peak, χ zero	$RA_{sub}^{(\pm1,\pm1)}$, $LSP+SPP_{sub}$
D	847	11.5	−5.59	−5.94	θ peak	$LSP+SPP_{sub}$
E	858	4.5	0.00	−12.27	T dip, θ zero, χ peak	$SPP_{sub}^{(\pm1,\pm1)}$
F	866	6.2	8.35	−5.79	θ peak	$LSP+SPP_{sub}$
G	941	29.6	2.54	1.31	T peak	$LSP+SPP_{sub}$
H	1143	11.0	−3.43	4.48	T dip	$LSP+SPP_{sub}$
I	1159	41.8	−7.83	0.29	θ peak	$RA_{sub}^{(\pm1,0)}$, $RA_{sub}^{(0,\pm1)}$
J	1168	53.5	−3.97	−0.16	T peak, χ zero	$SPP_{sub}^{(\pm1,0)}$, $SPP_{sub}^{(0,\pm1)}$

[a]The peaks of θ and χ refer to the maxima of the absolute values.
[b]Subscript—interface; superscript—order index.

points E and I in Fig. 5). This is a useful property of the PCS for their application as polarization control devices.

Third, in the full spectral range of interest (700–1400 nm), the hybridization or overlapping of RAs, SPPs, and LSPs commonly exists. Especially, at wavelengths between points B and J (where the first-order SPP_{up} and SPP_{sub} modes are excited, respectively), the LSPs are tightly combined with SPPs, which causes stronger circular birefringence/dichroism (see Fig. 5). At point C, the LSPs overlap with $RA_{sub}^{(\pm1,\pm1)}$, where the $(\pm1,\pm1)$ orders in the substrate side are on cutoff (turning from propagating to evanescent or vice versa); the grazing waves also strengthen the SPPs on the lower interface, leading to enhanced transmission. Therefore, we can say that the hybridization of anomalies is advantageous to the light coupling and benefits the enhanced transmission as well as the circular birefringence. This is consistent with the observations by McMahon *et al.*[37] on a thin gold film perforated with a square array of nanoholes.[38]

Finally, the roles and characteristics of the RAs, SPPs, and LSPs are different in modifying the optical response of PCS. SPPs are efficient light coupling channels for the RCP and LCP components to accumulate phase and amplitude differences, due to the relatively long propagation/interaction length of the SPPs. Also, since the SPPs can be excited in the vicinity of the resonance wavelength, the SPR peaks usually exhibit broadband and smooth features (see, e.g., the Fano-type feature at point J). Therefore, the impact of SPPs on the polarization effect is the most significant in all the three types of anomalies. In contrast, the RAs usually cause abrupt changes in spectra with sharp and narrow resonance features; their influence on the polarization effect is moderate unless a RA is hybridized with the SPPs (e.g., at point I). The LSPs are excited in a wide spectral range without any resonance condition. Though not contributing directly to the polarization effect, the LSPs provide an efficient channel for the tunneling of energy through the metallic film and mediate the coupling of anomalies on the upper and substrate interfaces.

Having recognized the characteristics of the anomalies, we can conclude several different coupling regimes in the PCS, through which the RCP and LCP components interact with the anomalies in the chiral structure and receive different modifications: (1) incident light → coupling to RAs and/or SPPs on the first interface → tunneling through LSPs → outcoupling to transmitted light. Examples: points A and B. (2) Incident light → tunneling through LSPs → coupling to RAs and/or SPPs on the second interface → outcoupling to transmitted light. Examples: points C, G, H, I, and J. (3) Incident light → coupling to RAs and/or SPPs on the first interface → tunneling through LSPs → coupling to RAs and/or SPPs on the second interface → outcoupling to transmitted light. Examples: points D, E, and F. (4) Incident light → tunneling through LSPs → outcoupling to transmitted light. Examples: the other nonresonant wavelengths, e.g., $\lambda < 750$ nm or >1200 nm.

Among all the four regimes, only the first three can significantly change the transmission and polarization properties of the PCS because of the occurrence of RAs and/or SPPs. Especially, when there is coupling between the RAs and/or SPPs on the upper and substrate interfaces, i.e., regime (3), the resonance is the strongest.

IV. DISCUSSION AND PERSPECTIVE

From the investigation presented above, we have understood the mechanism of light-matter interaction in the 2D metallic PCS. Then a natural expectation is: how to optimize the PCS so as to realize stronger simultaneously enhanced dual effect? We may find some clues from the light coupling regimes.

First, the SPPs have been revealed as the most important anomalies for enhancing the polarization effect in the 2D metallic PCS. However, in our PCS they only enhance transmission in the *nondiffraction regime* (where there are only the directly transmitted and reflected zeroth orders, such as point J) while suppress it in the *diffraction regime* (where there exist higher diffraction orders, such as points B and E). This fact has also been more or less observed in some previous plasmonic structures with perforated metal films.[24–26,37,38] Although this is just an empirical observation, it shows that the opening of more diffraction channels may

affect the interaction of incident light with the SPPs as well as the reradiation of electromagnetic energy into the zeroth transmitted order. Therefore, we should mainly utilize the excitation of the $SPP_{sub}^{(\pm 1,0)}$ and $SPP_{sub}^{(0,\pm 1)}$ modes to get the simultaneously enhanced dual effect, i.e., the PCS should work in subwavelength regime.

Second, the hybridization of RAs and SPPs can significantly enhance transmission[37,38] as well as the polarization effect (see Fig. 5). Therefore, in the design of the PCS, one may try to realize the first-order RAs and SPPs (i.e., points I and J) as close as possible to each other, preferably overlapped.

Third, the important role of SPPs implies that the continuous metal surface is indeed necessary in the PCS to maintain propagating surface waves with which the RCP and LCP components of the incident wave can couple and interact efficiently. The chiral holes are also necessary to maintain the cavity LSPs that act as tunneling channels for transferring electromagnetic energy between the upper and substrate interfaces. In this sense, the hole-type 2D metallic PCS are indeed advantageous over the particle-type ones.

The above discussion provides some guidelines to the design of 2D metallic PCS. However, we should emphasize that, since in the thin-film PCS the overlapping and coupling of different anomalies are very common, it is rather difficult to figure out the contribution of each single anomaly. Therefore, in the design of other PCS, the interaction between different anomalies should also be analyzed specifically to characterize the device performance. Rigorous numerical modeling of the far-field and near-field responses of the PCS has been shown to be a useful and convenient tool to achieve this goal.

Before the end of the discussion, we want to show how the dual effect of the 2D metallic PCS can be improved by simply increasing the gold film thickness. It has been shown by numerical optimization in Fig. 2 that, if the gold film thickness h is large enough, tens-of-degree polarization rotation may be achieved. In Fig. 12, we calculated the transmittance and polarization spectra of a PCS with $d=800$ nm, $L=l=120$ nm, and $h=200$ nm. Evidently, in this case the enhancement of the polarization effect is much stronger, especially in the spectral range between points B and J (still with the labeling in Fig. 5) where strongly hybridized LSPs and SPPs are dominant. For example, at point E where the $SPP_{sub}^{(\pm 1,\pm 1)}$ modes are excited, a suppressed transmission still occurs and the transmitted light is almost pure LCP due to the strong circular dichroism, meaning that the PCS can function as a LCP polarizer at this wavelength. In the vicinity of points I and J where the first-order SPPs and RAs are present, we observe a transmission peak of 34% accompanied by a peak polarization rotation up to −32° with almost zero ellipticity ($\tan\chi=0.05$), meaning that the PCS can work as a pure linear polarization rotator without elliptization at this wavelength.

With this example, we show the potential of the single-layer hole-type 2D metallic PCS. The experimental realization of such PCS with thicker gold film and high quality, however, needs fabrication methods other than the lift-off technique, which are under our investigation.

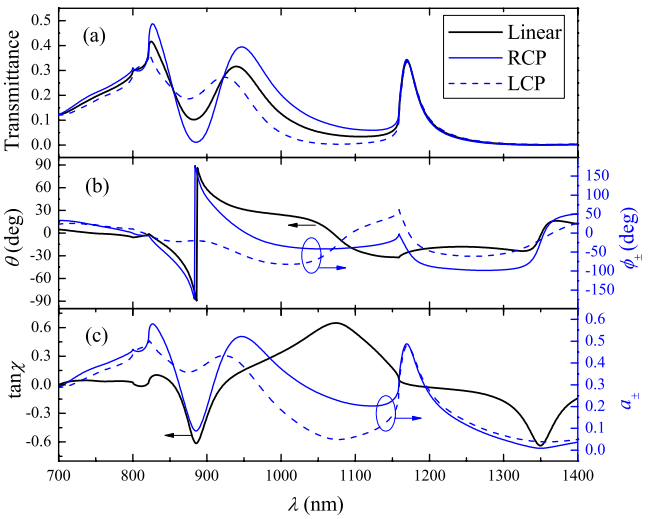

FIG. 12. (Color online) Similar as Fig. 5 but for a hole-type metallic PCS with $d=800$ nm, $L=l=120$ nm, and $h=200$ nm.

V. CONCLUSIONS

In this work, we propose a design of 2D metallic PCS consisting of a fused silica substrate and a thin gold film perforated with gammadion-shaped chiral holes. The hole-type metallic PCS are advantageous over previous particle-type ones in the sense that they can produce simultaneously enhanced transmission and artificial optical activity, thanks to the excitation of SPPs and RAs on the upper and substrate interfaces of the grating and the cavity LSPs in the gammadion holes. These anomalies can couple and interact strongly with the incident light and mediate the different penetration of RCP and LCP components through the chiral film, leading to enhanced circular birefringence and dichroism. The increased transmittance in the hole-type PCS provides a solution to the serious transmission loss in previous metallic PCS. Furthermore, the single-layer 2D metallic PCS are easier to realize in optical frequencies, by using mature microfabrication techniques such as EBL and lift-off, compared with the more complicated 3D and quasi-3D PCS.

The principle and optical performance of the proposed PCS are demonstrated by the experimental realization of a PCS sample, from numerical design, fabrication, to optical characterization. Good agreement between theory and experiment has been obtained. An enhanced transmittance peak of 53% is observed at wavelength 1168 nm accompanied nearby by a polarization rotation peak (about 8° in theory and 4° in experiment) at normal incidence. The effective specific rotatory power reaches 10^5 deg/mm, which is one or two orders of magnitude larger than that of previous particle-type 2D metallic PCS and several orders larger than that of natural chiral media.

The underlying physical mechanism of the enhanced dual effect is thoroughly studied by investigating the optical anomalies (RAs, SPPs, and LSPs) in the PCS and their roles in the light-matter interaction. Several light-anomaly coupling regimes have been revealed. It is seen that the SPPs can significantly change the amplitudes and accumulate phase difference of the RCP and LCP waves, leading to en-

hanced optical activity; the RAs also cause polarization change, which is more remarkable if hybridized with the SPPs; the LSPs, though do not contribute to the optical activity directly, function as efficient channels of transferring and coupling energy between the two sides of the chiral metal film.

The physical insight into the enhanced dual effect provides us useful guidelines for the design and optimization of the 2D metallic PCS. Knowing the enhancement mechanism, we may develop more complicated PCS, such as multilayer PCS with both metal and dielectric inclusions, with which to produce stronger optical activity and better optical performance. The perspective is to develop PCS-based functional polarization elements used in, e.g., integrated electro-optic systems.

ACKNOWLEDGMENTS

We acknowledge the support by the Academy of Finland (Projects No. 128420, No. 209806, and No. 129155), the Finnish Graduate School of Modern Optics and Photonics, the Research and Development Project on Nanophotonics funded by the Ministry of Education of Finland, and the National Basic Research Program of China (Project No. 2007CB935303).

*Corresponding author; baibenfeng@tsinghua.edu.cn

[1] M. Kuwata-Gonokami, N. Saito, Y. Ino, M. Kauranen, K. Jefimovs, T. Vallius, J. Turunen, and Y. Svirko, Phys. Rev. Lett. **95**, 227401 (2005).

[2] K. Konishi, T. Sugimoto, B. Bai, Y. Svirko, and M. Kuwata-Gonokami, Opt. Express **15**, 9575 (2007).

[3] A. Papakostas, A. Potts, D. M. Bagnall, S. L. Prosvirnin, H. J. Coles, and N. I. Zheludev, Phys. Rev. Lett. **90**, 107404 (2003).

[4] M. Decker, M. W. Klein, M. Wegener, and S. Linden, Opt. Lett. **32**, 856 (2007).

[5] V. A. Fedotov, A. S. Schwanecke, N. I. Zheludev, V. V. Khardikov, and S. L. Prosvirnin, Nano Lett. **7**, 1996 (2007).

[6] X. Meng, B. Bai, P. Karvinen, K. Konishi, J. Turunen, Y. Svirko, and M. Kuwata-Gonokami, Thin Solid Films **516**, 8745 (2008).

[7] B. Bai, K. Konishi, X. Meng, P. Karvinen, A. Lehmuskero, M. Kuwata-Gonokami, Y. Svirko, and J. Turunen, Opt. Express **17**, 688 (2009).

[8] A. V. Rogacheva, V. A. Fedotov, A. S. Schwanecke, and N. I. Zheludev, Phys. Rev. Lett. **97**, 177401 (2006).

[9] E. Plum, V. A. Fedotov, A. S. Schwanecke, N. I. Zheludev, and Y. Chen, Appl. Phys. Lett. **90**, 223113 (2007).

[10] J. C. W. Lee and C. T. Chan, Opt. Express **13**, 8083 (2005).

[11] M. Thiel, G. von Freymann, and M. Wegener, Opt. Lett. **32**, 2547 (2007).

[12] J. K. Gansel, M. Thiel, M. Wegener, K. Bade, V. Saile, G. von Freymann, and S. Linden, in *Proceedings of the Conference on Lasers and Electro-Optics/International Quantum Electronics Conference*, OSA Technical Digest (Optical Society of America, Baltimore, MD, 2009).

[13] E. Plum, J. Zhou, J. Dong, V. A. Fedotov, T. Koschny, C. M. Soukoulis, and N. I. Zheludev, Phys. Rev. B **79**, 035407 (2009).

[14] T. Clausnitzer, H.-J. Fuchs, E.-B. Kley, A. Tuennermann, and U. Zeitner, in *Lithographic and Micromachining Techniques for Optical Component Fabrication II*, Proceedings of SPIE Vol. 5183, edited by E.-B. Kley and H. P. Herzig (SPIE, Bellingham, WA, 2003), p. 8.

[15] L. Chen, J. J. Wang, F. Walters, X. Deng, M. Buonanno, S. Tai, and X. Liu, Appl. Phys. Lett. **90**, 063111 (2007).

[16] I. Hodgkinson and Q. H. Wu, Appl. Phys. Lett. **74**, 1794 (1999).

[17] B. Bai, Y. Svirko, J. Turunen, and T. Vallius, Phys. Rev. A **76**, 023811 (2007).

[18] S. J. Elston, G. P. Bryan-Brown, and J. R. Sambles, Phys. Rev. B **44**, 6393 (1991).

[19] A. V. Kats and I. S. Spevak, Phys. Rev. B **65**, 195406 (2002).

[20] A. Yariv and P. Yeh, *Optical Waves in Crystals* (Wiley, New York, 1983).

[21] T. W. Ebbesen, H. J. Lezec, H. F. Ghaemi, T. Thio, and P. A. Wolff, Nature (London) **391**, 667 (1998).

[22] S. Wedge, I. R. Hooper, I. Sage, and W. L. Barnes, Phys. Rev. B **69**, 245418 (2004).

[23] Q. Cao and P. Lalanne, Phys. Rev. Lett. **88**, 057403 (2002).

[24] W. L. Barnes, W. A. Murray, J. Dintinger, E. Devaux, and T. W. Ebbesen, Phys. Rev. Lett. **92**, 107401 (2004).

[25] C. P. Huang, Q. J. Wang, and Y. Y. Zhu, Phys. Rev. B **75**, 245421 (2007).

[26] A. V. Zayats and I. I. Smolyaninov, J. Opt. A, Pure Appl. Opt. **5**, S16 (2003).

[27] B. Bai and L. Li, J. Opt. A, Pure Appl. Opt. **7**, 783 (2005).

[28] L. Li, J. Opt. Soc. Am. A Opt. Image Sci. Vis. **14**, 2758 (1997).

[29] B. Bai and L. Li, J. Opt. Soc. Am. A Opt. Image Sci Vis. **21**, 1886 (2004).

[30] E. Collett, *Polarized Light: Fundamentals and Applications* (Marker Dekker, New York, 1993).

[31] A. Lehmuskero, M. Kuittinen, and P. Vahimaa, Opt. Express **15**, 10744 (2007).

[32] H. Eyring, H. Liu, and D. Caldwell, Chem. Rev. **68**, 525 (1968).

[33] V. Lucarini, J. J. Saarinen, K.-E. Peiponen, and E. M. Vartiainen, *Kramers-Kronig Relations in Optical Materials Research* (Springer, Heidelberg, 2005).

[34] P. G. de Gennes, *The Physics of Liquid Crystals* (Clarendon, Oxford, 1974).

[35] A. Hessel and A. A. Oliner, Appl. Opt. **4**, 1275 (1965).

[36] E. G. Loewen and E. Popov, *Diffraction Gratings and Applications* (Marcel Dekker, New York, 1997).

[37] J. M. McMahon, J. Henzie, T. W. Odom, G. C. Schatz, and S. K. Gray, Opt. Express **15**, 18119 (2007).

[38] H. Gao, J. M. McMahon, M. H. Lee, J. Henzie, S. K. Gray, G. C. Schatz, and T. W. Odom, Opt. Express **17**, 2334 (2009).

Anni Lehmuskero

Metallic thin film structures and polarization shaping gratings

This book provides a survey of some optical phenomenon in metallic nano- and microstructures. It includes the study of the optical properties of thin metallic films, laser-colored stainless steel surfaces, and metallic subwavelength gratings that shape the polarization mainly through plasmonic and grating resonances. The optical phenomena have been examined by theoretical modeling, fabricating structures by electron-beam lithography and laser-marking technique, and using mainly ellipsometry for the characterization.

UNIVERSITY OF
EASTERN FINLAND

Publications of the University of Eastern Finland
Dissertations in Forestry and Natural Sciences

ISBN 978-952-61-0285-6
ISSN 1798-5668